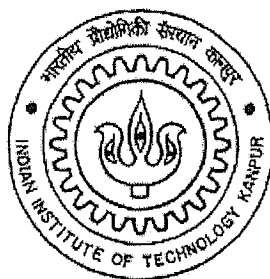


Development of Crystallographic Texture in a Ni-40 Co and Ni-60 Co alloys during Deformation and Recrystallization

A Thesis Submitted
In Partial Fulfilment of the requirements
For the degree of
MASTER OF TECHNOLOGY

by

SHASH RANJAN DEY



DEPARTMENT OF METALLURGICAL ENGINEERING
INDIAN INSTITUTE OF TECHNOLOGY, KANPUR
FEBRUARY 2002

4 FEB 2003 / MMG

पुरुषोत्तम काशीनाथ केनकर पुस्तकालय

भारतीय प्रौद्योगिकी संस्थान कानपुर

अवधि क्र० A 141867



A141867


**Dedicated
to
Maa, Baba,
Dada, Silky,
Alakaya
&
Akhila**

27-2-02
2.

CERTIFICATE

This is to certify that the work **Development of Crystallographic Texture in a Ni-40 Co and Ni-60 Co Alloys During Deformation and Recrystallization** has been carried out by SUHASH RANJAN DEY under my supervision and that it has not been submitted elsewhere for a degree.

Date : 26/02/02



(Dr. R. K. Ray)

Professor,

Department of Metallurgical Engineering

Indian Institute of Technology

Kanpur, 208016

India.

First and foremost I express my indebtedness and gratitude to Professor R.K.Ray for his valuable guidance and inspiring encouragement throughout the tenure of this work. It has been my good fortune to be associated with such an excellent teacher and an impressing personality during my stay at IIT, Kanpur.

I sincerely acknowledge the help and support rendered by Dr. Mungole to allow me to use some of the facilities of the Metallography Lab.

I would like to convey my sincere thanks to Mr. V. Kumar for his valuable and elderly advice and extending all possible and sincere help through the course of this study and I feel very fortunate to have a laboratory assistant and friend like him.

My sincere thanks are due to Dr. Gauthama and Mr. S.C. Barthwal for their active co-operation during the tedious period of TEM study.

Finally I would like to mention those integral part of my IIT life, my friends, who have made every moment of stay here at IITK to rejoice in future. The list is endless, still, the support, cooperation and help rendered by my laboratory partners Pinaki, Arijit, Krishnendu and Deepti are gratefully acknowledged.

I am at a total loss of words in expressing the depth of my emotions for my Baba, Maa, Dada, Silky, Alakaya and Akhila for their constant support throughout.

I am also very much thankful to CSIR(Council of Scientific & Industrial Research) for their Research Fellowship during my M.Tech.

(Suhash Ranjan Dey)

CONTENTS

		PAGE
	LIST OF TABLES	V
	LIST OF FIGURES	VI
	ABSTRACT	IX
CHAPTER	TITLE	
1	INTRODUCTION	1
2	LITERATURE REVIEW	3
2.1	Microstructure of Cold Worked Metals	3
2.2	Stored energy of the cold work	4
2.3	The release of stored energy	5
2.4	Recovery	7
2.4.1	Property changes during recovery	7
2.4.2	The kinetics of recovery	8
2.4.3	Recovery mechanisms	10
2.5	Recrystallization	16
2.5.1	Primary recrystallization	18
2.5.1.a	Grain boundary migration	25
2.5.1.b	Orientation dependence of boundary migration	25
2.6	Continuous grain growth	26
2.7	Preferred Orientation or Texture	29
2.7.1	Introduction	29
2.7.2	Determination of Texture	29
2.7.3	Rolling Texture	34
2.7.4	Annealing Texture	34
2.7.5	Rolling Texture and Annealing Texture of Ni-Co alloys	35
2.7.6	Recrystallization and Cube Texture	43
2.8	Correlation of Literature Study with present investigation	47
		III

CHAPTER	TITLE	PAGE
3	EXPERIMENTAL PROCEDURE	48
3.1	Cold Rolling	48
3.2	Recrystallization Anneal	49
3.3	Optical Microscopy	49
3.4	Electron Microscopy	49
3.5	Determination and Representation of Texture	50
4.	RESULTS	52
5.	DISCUSSIONS	99
6.	CONCLUSION	103
	REFERENCES	104
	APPENDIX	

LIST OF TABLES

No.	TITLE	PAGE
Table 1.	Chemical composition of alloys (wt%).	51
Table 2.	Texture components and their weightage of Ni-40 Co and Ni-60 Co (95% cold rolled and annealed at 800°C for various time Time durations.	86

LIST OF FIGURES

No.	TITLE	PAGE
Figure 1.	Nickel Cobalt Binary Phase Diagram.	2
Figure 2.	Anisothermal anneal curve. Electrolytic copper.	6
Figure 3.	Isothermal anneal curve. High purity copper.	6
Figure 4.	Anisothermal-anneal curve for cold worked nickel.	9
Figure 5.	Change in dislocation density during the recovery of iron at 550°C.	12
Figure 6.	Schematic Laue patterns showing how polygonization breaks up Asterated X-ray reflections into a series of discrete spots.	11
Figure 7(a).	Random arrangement of excess parallel edge dislocations	
Figure 7(b).	Alignment into dislocations walls (polygonisation).	12
Figure 8.	Dislocation structure at a Y-junction.	14
Figure 9.	Schematic representation of sub-grain coalescence by sub-grain rotation.	15
Figure 10.	Plot of E vs. θ .	17
Figure 11.	Nucleation by sub-grain growth in a deformation band.	20
Figure 12.	Schematic representation of the formation of a recrystallized grain by the coalescence of sub-grains.	21
Figure 13.	Schematic representation of strain induced boundary migration (a) Configuration before annealing (b) The boundary between the cold worked grains A and B has migrated from position 1 to position 2.	22
Figure 14.	Model for high grain boundary migration process in recrystallization.	24
Figure 15(a).	A grain of the orientation g is surrounded by grains of the orientations G_i and g_j . The energy of the a-boundaries tends to contract the grain whereas the b-boundaries tend to expand it	
Figure 15(b).	Growth of region 2 by the movement of interface boundary from region 2 to region 1	

Figure 15(c).	Curvature of grain boundaries in n-sided two dimensional grains.	28
Figure 16.	The rolling plane and rolling direction in a metal sheet subjected to rolling.	30
Figure 17.	Schematic illustration of pole figure construction.	32
Figure 18(a).	Specimen frame and crystallite frame	
Figure 18(b).	The three rotations for superimposing crystallite frame on reference frame	
Figure 18(c).	Orientation space.	33
Figure 19.	(111) pole figure of pure Cu (a) and 70:30 brass (b).	36
Figure 20.	Effect of composition on stacking fault energy.	37
Figure 21.	{111} pole figures showing the cold rolling textures developed in pure Ni and Ni-Co alloys.	38
Figure 22.	Position of α , β and τ textures fibres in the Euler space.	39
Figure 23(a).	Plot of $f(g)$ vs ϕ_1 along the line $\phi = 45^\circ$, $\phi_2 = 0$ or 90° , Ni-40% Co	
Figure 23(b).	Plot of $f(g)$ vs ϕ along the line $\phi_1 = 90^\circ$, $\phi_2 = 45^\circ$, Ni-40% Co alloy	
Figure 23(C).	Plot of $f(g)$ vs ϕ_2 , Ni-40% Co alloy	
Figure 23(d).	Plot of ϕ_1 / ϕ vs ϕ_2 , Ni-40% Co alloy.	40
Figure 24.	Plot showing the variation of M_i with % Co in Ni-Co alloys.	42
Figure 25.	Typical cube texture in nickel. {111} poles shown in {100} <001> Texture.	25
Figure 26.	Pure Copper (a) Cu type rolling texture (b) Cube type annealing texture.	45
Figure 27.	Grain boundary migration (a) before migration (b) after migration.	46
Figure 28.	Growing of cube texture region during annealing.	46
Figure 29.	Optical Micrographs of Ni-40 Co alloy.	53
Figure 30.	Optical Micrographs of Ni-60 Co alloy.	54
Figure 31.	Microstructure of Ni-40 Co alloy (95 % Cold Worked).	57
Figure 32.	Microstructure of Ni-40 Co alloy (annealed for 15 minutes at 800°C).	58

Figure 33.	Microstructure of Ni-40 Co alloy (annealed for 30 minutes at 800°C).	59
Figure 34.	Microstructure of Ni-40 Co alloy (annealed for 1 hour at 800°C).	60
Figure 35.	Microstructure of Ni-40 Co alloy (annealed for 3 hours at 800°C).	61
Figure 36.	Microstructure of Ni-40 Co alloy (annealed for 5 hours at 800°C).	62
Figure 37.	Microstructure of Ni-40 Co alloy (annealed for 10 hours at 800°C).	63
Figure 38.	Microstructure of Ni-40 Co alloy (annealed for 20 hours at 800°C).	64
Figure 39.	Microstructure of Ni-40 Co alloy (annealed for 50 hours at 800°C).	65
Figure 40.	Microstructure of Ni-60 Co alloy (95 % Cold Worked).	66
Figure 41.	Microstructure of Ni-60 Co alloy (annealed for 15 minutes at 800°C).	67
Figure 42.	Microstructure of Ni-60 Co alloy (annealed for 30 minutes at 800°C).	68
Figure 43.	Microstructure of Ni-60 Co alloy (annealed for 1 hour at 800°C).	69
Figure 44.	Microstructure of Ni-60 Co alloy (annealed for 3 hours at 800°C).	70
Figure 45.	Microstructure of Ni-60 Co alloy (annealed for 5 hours at 800°C).	71
Figure 46.	Microstructure of Ni-60 Co alloy (annealed for 10 hours at 800°C).	72
Figure 47.	Microstructure of Ni-60 Co alloy (annealed for 20 hours at 800°C).	73
Figure 48.	Microstructure of Ni-60 Co alloy (annealed for 50 hours at 800°C).	74
Figure 49.	ODF of 95% cold rolled Ni-40 Co alloy.	78
Figure 50.	ODF of 15 minutes annealed Ni-40 Co alloy at 800°C.	79
Figure 51.	ODF of 20 hours annealed Ni-40 Co alloy at 800°C.	80
Figure 52.	ODF of 50 hours annealed Ni-40 Co alloy at 800°C.	81
Figure 53.	ODF of 95% cold rolled Ni-60 Co alloy.	82
Figure 54.	ODF of 15 minutes annealed Ni-60 Co alloy at 800°C.	83
Figure 55.	ODF of 20 hours annealed Ni-60 Co alloy at 800°C.	84
Figure 56.	ODF of 50 hours annealed Ni-60 Co alloy at 800°C.	85
Plot1.	Plot showing the variation of M_i [%] with annealing time in Ni-40 Co alloy.	95
Plot 2.	Plot showing the variation of pole density, $f(g)$ with annealing time(hrs) in Ni-40 Co alloy.	96
Plot3.	Plot showing the variation of M_i [%] with annealing time in Ni-60 Co alloy.	97
Plot 4.	Plot showing the variation of pole density, $f(g)$ with annealing time(hrs) in Ni-60 Co alloy.	98

ABSTRACT

The Ni-Co alloys with up 30% Co show pure metal-type rolling texture, while the Ni-60% Co alloy shows alloy-type texture. The rolling texture of the Ni-40 % Co alloy lies in between these two extremes. Although the rolling textures of Ni-Co alloys have been well documented, not much work has been done on the formation of recrystallization textures in them. In view of the industrial importance of this class of alloys it is necessary to carry out detailed study of the deformation and recrystallization textures of Ni-Co alloys. In this study an attempt has been made to understand the development of crystallographic texture in a Ni-40 Co and a Ni-60 Co alloy during deformation and recrystallization. Samples of these two alloys were processed properly to produce texture-less starting materials. These were cold rolled 95%, followed by recrystallization annealing at 800°C. Microstructural characterization was carried out using optical and Transmission Electron Microscopy(TEM), while textures were measured by using the ODF(Orientation Distribution Function) method.

The deformed Ni-60 Co alloy shows an alloy-type texture, whereas the deformation texture of the Ni-40 Co alloy possesses the characteristics of both pure metal-type and alloy-type. Upon recrystallization, the annealing texture of the Ni-40 Co alloy shows predominantly the Rotated Cube component with some Cube as well as some other minor components. On the other hand, the annealing texture of the Ni-60 Co alloy shows two major components, namely the Bs/G $\{110\}<511>$ and the Rotated Goss(RG) $\{110\}<011>$. An attempt has been made to understand the origin and growth of the annealing texture components in both the alloys.

CHAPTER 1

INTRODUCTION

Pure f.c.c. metals and alloys are known to exhibit three different types of rolling textures, namely (i) α -brass or alloy-type in materials of low stacking fault energy; (ii) copper or pure metal-type in materials of medium stacking fault energy; and (iii) aluminium-type texture in very high stacking fault energy materials. A large number of investigations have been carried out to characterize the rolling textures of pure Cu and Al and a number of their alloys. On the basis of these results it is now known that while in the α -brass or alloy-type texture one has practically only the brass (Bs) component $\{110\}\langle 112 \rangle$, and in the copper or pure metal-type the Cu $\{112\}\langle 111 \rangle$, S $\{123\}\langle 634 \rangle$ and brass components are nearly equally strong, it is the S component which predominates in aluminium-type.

Excepting Cu, Ag and Au, extensive data on stacking fault energy (SFE) are available for two other f.c.c. metals, e.g. aluminium and nickel. A reasonable value of the SFE of Al as estimated from its coherent twin energy, is 200 mJ/m^2 , while for Ni a value of 130 mJ/m^2 is probably reasonably accurate. Although extensive research on the deformation and recrystallization textures of Cu and Al base alloys has been carried out over the years, very little work has been done on pure Ni and its alloys. This is surprising because the Ni-base alloys are industrially very important. The addition of Co in Ni decreases the SFE of Ni drastically. Thus, it was thought that a thorough and systematic study of the deformation and recrystallization texture in pure Ni and a number of Ni-Co alloys will be useful in bridging this gap in the existing knowledge.

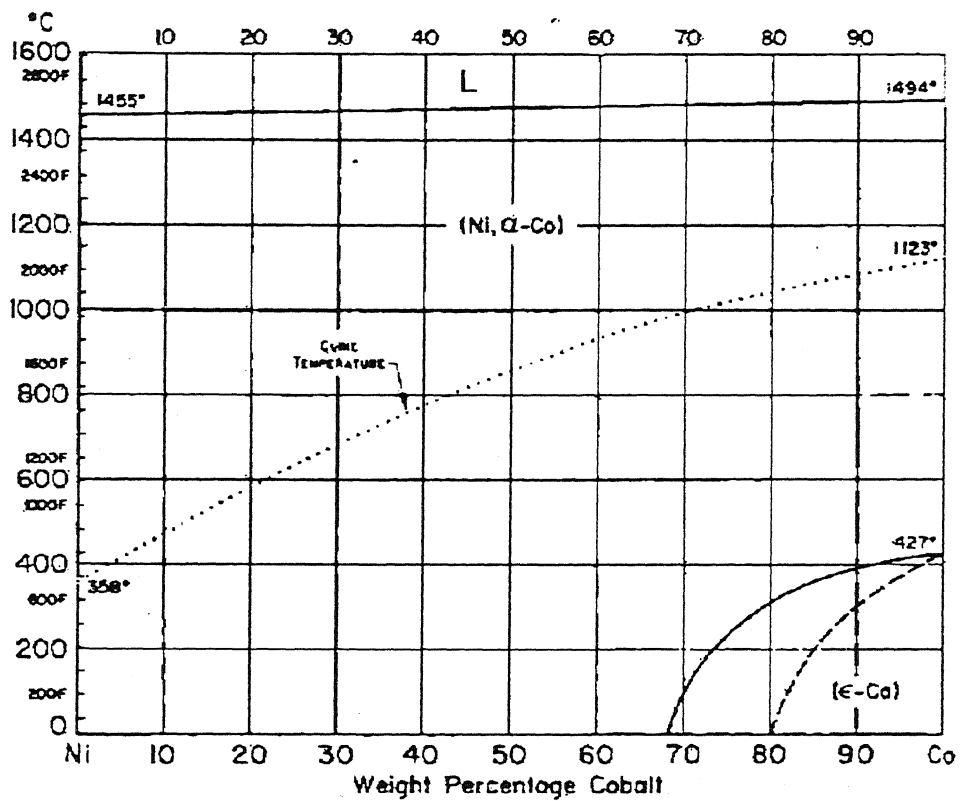


Figure 1. Nickel Cobalt Binary Phase diagram.

CHAPTER 2

LITERATURE REVIEW

A stress applied to a material causes a deformation, or strain. The deformation may either be *elastic*, which disappears upon removal of the load, or *plastic*, which remains in the material even after the stress has been removed. When a metal is deformed plastically at temperatures that are low relative to its melting point, be it in tension, compression or torsion, the stress required to deform it further usually increases. After such deformation the crystal is said to be in the work-hardened, or cold worked, state. The principal entities responsible for the cold worked state are point defects such as vacancies and interstitials as well as linear and planar defects like dislocations and stacking faults etc. Plastic deformation of a material involves a permanent shape change produced by stressing the material beyond its elastic limits, during which any or all of the types of the defects mentioned above may be produced in the solid. As this increases the dislocation density in different planes and directions. These differently oriented dislocations will interfere with one another in their movement and the real strength of the metal will increase.

2.1 Microstructure of Cold Worked Metals

Transmission electron microscopic techniques have been successfully applied for determining the structures of cold worked materials. Electron microscopic observations on polycrystalline cold worked metals shows grains of deformed metals having groups of slightly misoriented regions (cells) with a low density of dislocations surrounded by spatial dislocation networks (cell walls)[1,2]. The size of a cell may be 1-2 μm and the thickness of its wall, a few tenths of a micrometer. The structure is said to be a cell structure. As deformation proceeds, the total dislocation density increases and dislocations are redistributed and form dislocation arrays, which divide a crystal (or grain) into volumes that are relatively, free dislocations, i.e. a cell structure is formed. An important feature in the formation of a cell structure is that the size of cells is only slightly dependent on the original grain size and decreases to a certain limit with increasing deformation. Another feature typical of a cell structure is

that the crystal lattice has quite strong distortions at cell boundaries, which depend on the misorientation angle θ .

The initial stage of plastic deformation is associated with the appearance of macroinhomogeneities in the distribution of deformations over the volume of a crystallite. At this stage, kink bands and secondary slip bands appear, in which deformation occurs in slip planes different from the main portion of the crystallite (rotational slip). Subsequently, kink bands and secondary slip bands become obstacles for dislocation movement.

2.2 Stored energy of the cold work

Most of the energy expended in cold work appears in the form of heat, but a finite fraction is stored in the metal as strain energy associated with various lattice defects created by the deformation. The amount of energy retained depends on the deformation process and a number of other variables, for example, composition of the metal as well as the rate and temperature of deformation. A number of investigators have indicated that the fraction of the energy, which remains in the metal, varies from a low percentage to somewhat over 10 percent. The data, from the work of Gordon[3], show that the stored energy increases with increasing deformation, but at a decreasing rate, so that the fraction of the total energy stored decreases with increasing deformation. The amount of stored energy can be greatly increased by increasing the severity of the deformation, lowering the deformation temperature, and by changing the pure metal to an alloy. Cold working is known to increase greatly the number of dislocations in a metal. A soft annealed metal can have dislocation densities of the order of 10^6 to 10^8 cm^{-2} , and heavily cold worked metals can have approximately 10^{12} . Since each dislocation represents a crystal defect with an associated lattice strain, increasing the dislocation density increases the strain energy of the metal.

While plastic deformation certainly increases the entropy of a metal, the effect is small compared to the increase in internal energy (the retained strain energy). The term $-TS$ in the free-energy equation may, therefore, be neglected and the free-energy increase equated directly to the stored energy. Therefore

$$F = E - TS$$

becomes

$$F = E$$

Where F is the free energy associated with the cold work, E is the internal, or stored strain energy, S is the entropy increase due to the cold work, and T is the absolute temperature.

2.3 The release of stored energy

Valuable information about the nature of the reactions that occur as a cold worked metal returns to its original state may be obtained through a study of the release of its stored energy. Out of several basically different methods of accomplishing this. Two of the more important methods are now be briefly indicated. In the *anisothermal anneal* method, the cold worked metal is heated continuously from a lower to a higher temperature and the energy release is determined as a function of temperature. One form of anisothermal anneal measures the difference in the power required to heat two similar specimens at the same rate. One specimen of the two is cold worked before the heating cycle, while the other serves as a standard and is not deformed. During the heating cycle, the cold worked specimen undergoes reactions that release heat and lower the power required to heat it in comparison with that required to heat the standard specimen. Measurements of the difference in power give direct evidence of the rate at which heat is released in the cold worked specimen. Figure 2 shows a typical anisothermal anneal curve[4] for a commercially pure copper (99.97 percent copper). It is noteworthy that some heat is released at temperatures only slightly above room temperature.

The other method of studying energy release involves *isothermal annealing*. Here the freed energy is measured while the specimen is maintained at a constant temperature. Figure 3 is representative of the type of curves obtained in an isothermal anneal.

Both the anisothermal anneal and the isothermal anneal curves of Figure 2 and Figure 3 and show maxima corresponding to large energy releases. Metallographic specimens prepared from samples annealed by either method show that an interesting phenomenon occurs in the region of maximum energy release. These large energy releases appear simultaneously with the growth of an entirely new set of essentially strain-free crystals which grow at the expense of the original badly deformed crystals.

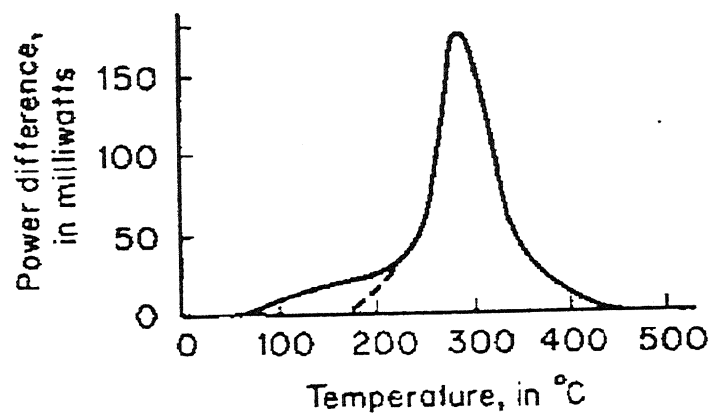


Figure 2. Anisothermal anneal curve. Electrolytic copper[4].

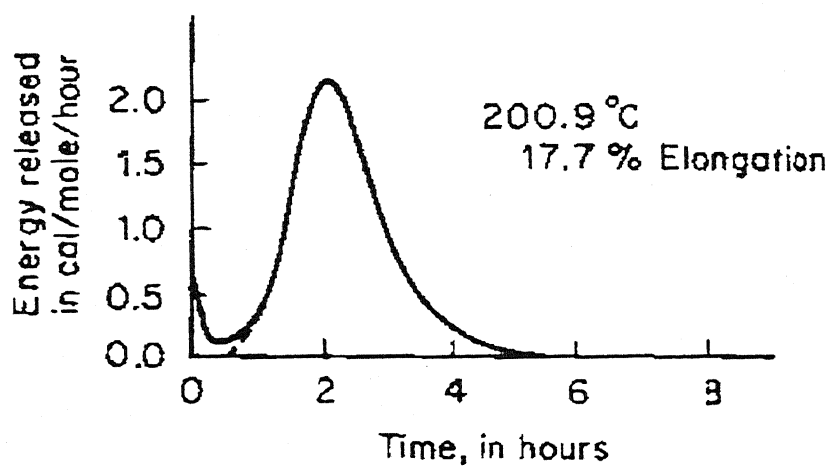


Figure 3. Isothermal anneal curve. High purity copper[3].

The process by which this occurs is called *recrystallization* and may be understood as a realignment of the atoms into crystals with a lower free energy. While the major energy release of the curves of Figure 2 and Figure 3 and correspond to recrystallization, both curves show that energy is released before recrystallization. The area under each solid curve that lies to the left and above the dashed lines represents an energy release not associated with recrystallization. In the anisothermal anneal curve, this freeing of strain energy starts at temperatures well below those at which recrystallization starts. Similarly, in the isothermal anneal curve it begins at the start of the annealing cycle and is nearly completed before recrystallization starts. The part of the annealing cycle that occurs before recrystallization is called *recovery* (termed by Haessner[5]). However, the reactions that occur during the recovery stages are able to continue during the progress of recrystallization; not in those regions which have already recrystallized, but in those that have not yet been converted into new crystals. The third stage of annealing is – *grain growth*. Grain growth occurs when annealing is continued after recrystallization has been completed. In grain growth, certain of the recrystallized grains continue to grow in size, but only at the expense of other crystals which accordingly disappear.

Therefore, the three stages of annealing – recovery, recrystallization, and grain growth.

2.4 Recovery

In general sense, *recovery* should be understood as the process of structural perfection of cold-worked metal by redistribution and annihilation of point defects and redistribution of dislocations by conservative slip without formation of new boundaries[6,7]. Thus, the stage of recovery involves no visible changes in the microstructure of the metal.

2.4.1 Property changes during recovery

In the recovery stage of annealing, the physical and mechanical properties that suffered changes as a result of cold working tend to recover their original values. The various physical and mechanical properties do not recover their values at the same

rate indicates the complicated nature of the recovery process. Normally the restoration of a mechanical property such as hardness or yield strength to its fully annealed value is only about one-fifth completed during recovery[7]. Figure 4 shows another anisothermal anneal curve corresponding to the energy released on heating cold worked polycrystalline nickel. The peak at point *c* defines the region of recrystallization. It can be seen that the resistivity is almost completely recovered before the state of recrystallization. On the other hand, the major change in the hardness occurs simultaneously with recrystallization of the matrix.

2.4.2 The kinetics of recovery

The kinetics of recovery can be characterized by the fact that the process has no incubation period. Its rate is at a maximum at the initial instant ($\tau = 0$) and then decrease exponentially.

Denoting by *X* the restored fraction of a property, we have :

$$X = 1 - \exp \left[-k' \tau \exp \left(\frac{-Q}{RT} \right) \right] \quad (1)$$

where *T* and τ are respectively the absolute temperature and time of heating; *Q* is the activation energy; *R* is the gas constant; and *k'* is a coefficient.

For an isothermal process:

$$X = 1 - \exp (-k' \tau) \quad (2)$$

$$\frac{dX}{d\tau} = \frac{k'}{\tau} \quad (3)$$

i.e. the rate of variation of the property which is restored by recovery is inversely proportion to the time of heating and has a maximum at the beginning of the process.

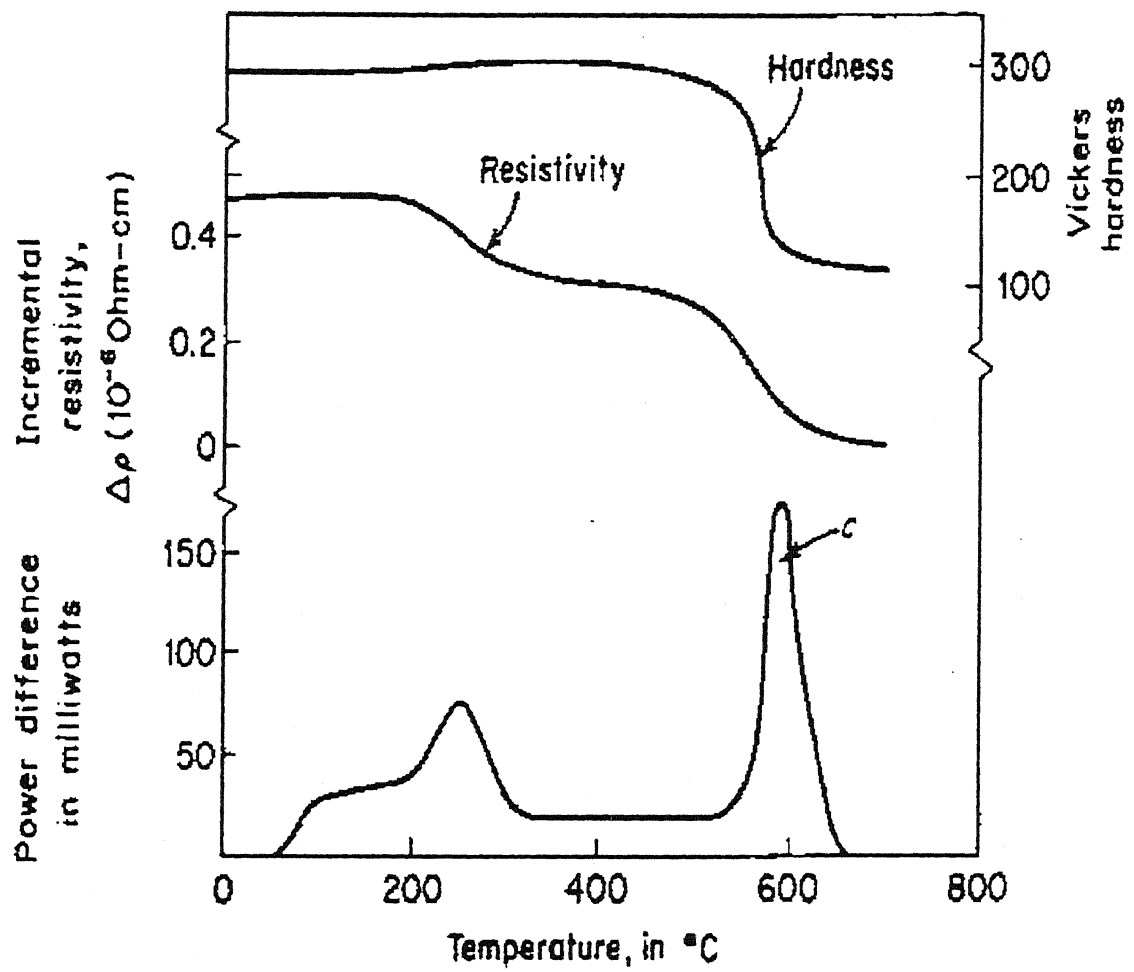


Figure 4. Anisothermal-anneal curve for cold worked nickel[4].

2.4.3 Recovery mechanisms

Electron microscopic evidence shows that, in a cold worked metal has cell structures. The cell wall consists of dislocation tangles, and some additional dislocations are found to exist in the cell interiors. As annealing starts, the tangled dislocations in the cell walls are supposed to rearrange themselves while some of the dislocations from within the cells may be attracted to cell walls. During the whole process of recovery dislocation annihilation probably occurs since the dislocation density in the cell interiors is found to decrease gradually on continued annealing. The cell walls become more clearly defined and eventually form sub-grains of about the same size as the initial cells. The sub-grain size does not change much until quite late in the recovery process when it starts increasing slightly. Thus, it might be said that, in general, three processes – dislocation annihilation, subgrain formation and sub-grain growth[8] – may take place during the recovery of most metals.

(i) *Dislocation annihilation*

From direct experimental evidence, Keh[9] stated that the dislocation density decreases during the initial stages of recovery (Figure 5). But presumably this does not involve the movements of dislocations over long distances. According to Li[10], dislocation annihilation takes place at the cell boundaries.

It has been found that elongated dislocation loops gradually becomes circular and finally vanish[11]. Similarly, Wagner[12] has shown that stacking faults also, can be annealed out during the recovery stage.

(ii) *Polygonisation and sub-grain formation*

Polygonisation is understood as the process of formation and coarsening of sub-grains during heating of cold worked metals and alloys. Sub-grains are formed by redistribution of individual dislocations and/or by ‘flattening’ of spatial dislocation pile-ups due to dislocation slip and climb, with the formation of low-angle dislocation sub-boundaries. Coarsening of sub-grains is realized by their coalescence or by migration of sub-boundaries.

The phenomenon of polygonisation was first observed by S.T.Konobeevsky and I.I.Mirer in rock salt crystals. They found that radially extended spots (asterism

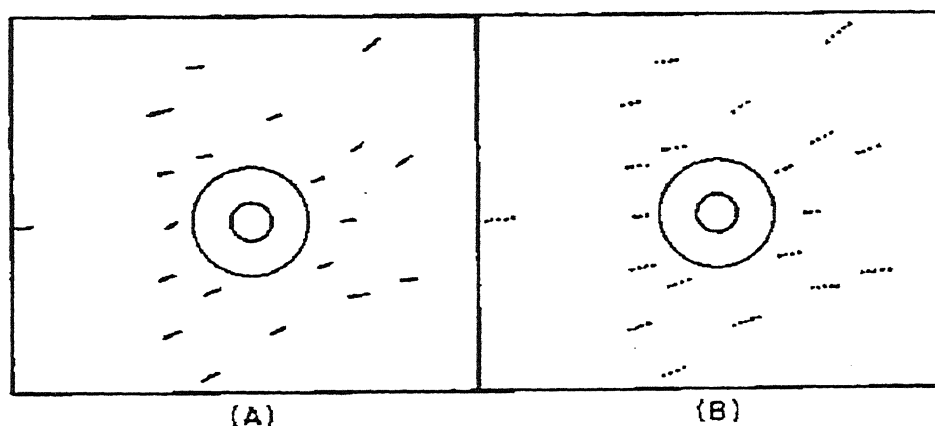


Figure 6. Schematic Laue patterns showing how polygonisation breaks up asterated X-ray reflections into a series of discrete spots.

streaks) in Laue photographs Figure 6 of a salt crystal deformed by bending were separated on annealing into discrete single fine spots. This effect implies that a plastically bent crystal disintegrates on annealing into a number of structurally perfect blocks which are discretely tilted through small angles relative to one another, with misorientation of the crystal remaining unchanged. In that case, each spot is a trace of an interference beam 'reflected' from an individual block.

This has been explained as due to a process – polygonisation – which leads to a rearrangement of dislocations, with a resultant lowering of the lattice strain energy. The mechanism has been shown schematically in Figure 7. The random arrangement of excess parallel edge dislocations produced during deformation can clearly be seen, on heating, to align themselves, into walls to small angle, polygonisation or sub-grain boundaries by a process of annihilation and rearrangement. That the dislocation walls so produced were normal to the main slip planes active during bending was verified by Cahn[13,14] by producing etch pits after the anneal. The process of polygonisation is believed to start with the glide and climb of individual dislocations, thereby forming small segments of boundary perhaps five to ten dislocations high. By further glide and climb these short range boundary segments then combine to give larger

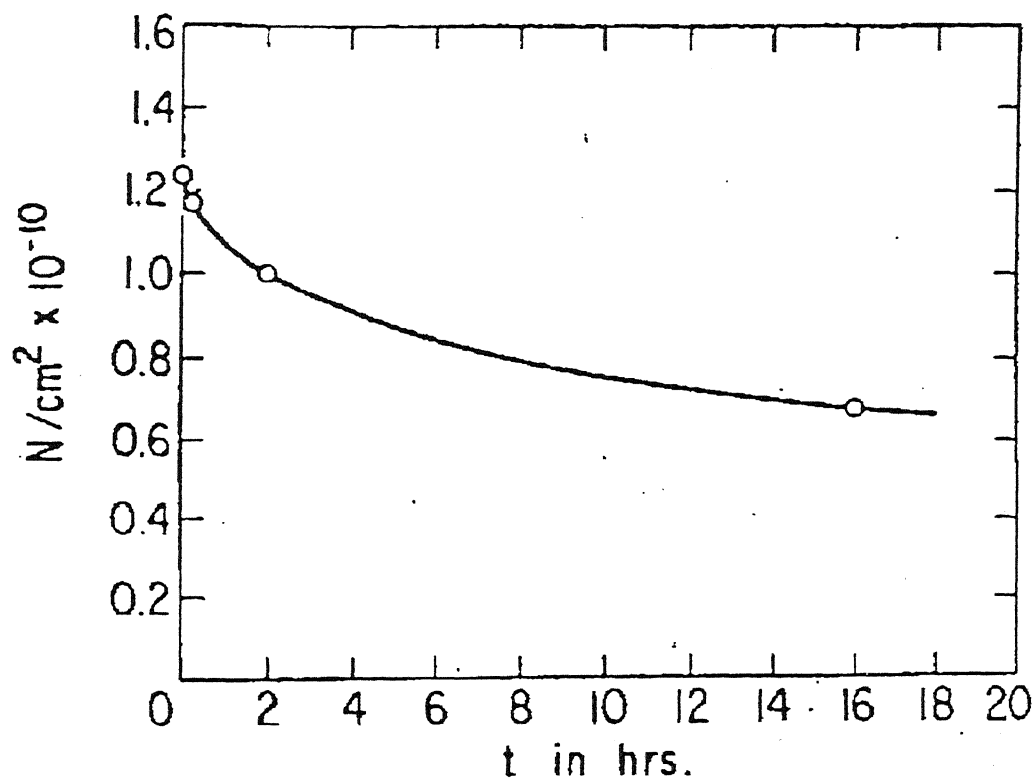


Figure 5. Change in Dislocation Density during the Recovery of Iron at 550°C.

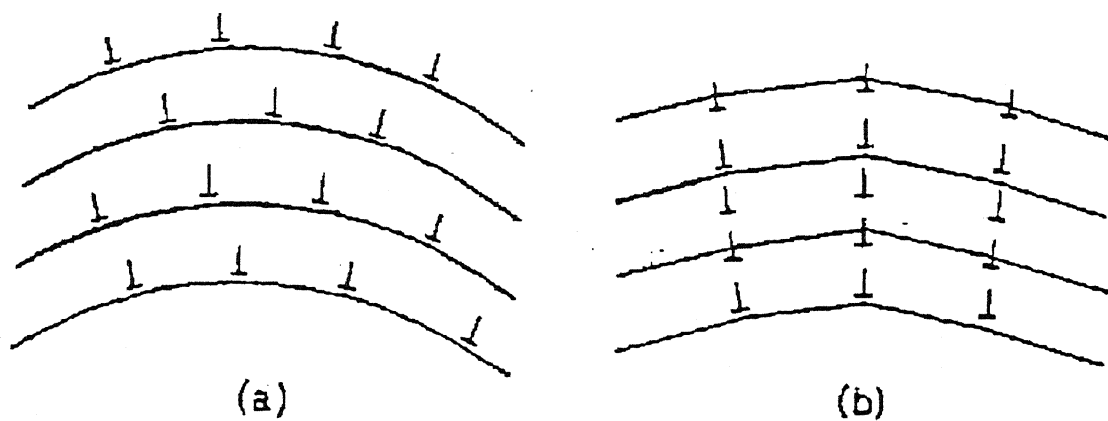


Figure 7(a). Random arrangement of excess parallel edge dislocations.

Figure 7(b). Alignment into dislocation walls (Polygonisation).

boundaries, still of low angle, which may now be termed long range. At higher temperature the spacings between these boundaries are found to increase and this lies led to the suggestion by Dunn and Daniel[15] and later Gilman[16] that two neighbouring boundaries may coalesce. This is thought to take place by the so called Y-junction mechanism[17] which produces a single boundary (Figure 8). Although misorientation across the single boundary will be the sum of both the original boundaries, the total energy of the system is lowered by this mechanism[18].

(iii) *Sub-grain growth*

Two mechanisms – sub-boundary migration and sub-grain coalescence – have been proposed to explain the growth of sub-grains during recovery.

Growth by sub-grain boundary migration is similar in terms to primary grain growth where grains larger than a critical size are supposed to grow at the expense of those which are small than the critical size. The rate of growth of a particular sub-grain is given by Hu and Szirane[19] as

$$\frac{dR}{dt} = M \left(\Delta G - 2 \frac{\sigma}{R} \right) \quad (4)$$

where R is the radius of the growing sub-grain

M is the interface mobility

ΔG is the free energy per unit volume for growth

and σ is the specific surface energy of the interface.

At equilibrium $\frac{dR}{dt} = 0$ so that

$$R = \frac{2\sigma}{\Delta G} \quad (5)$$

It follows that growth will occur if

$$R > \frac{2\sigma}{\Delta G} \quad (6)$$

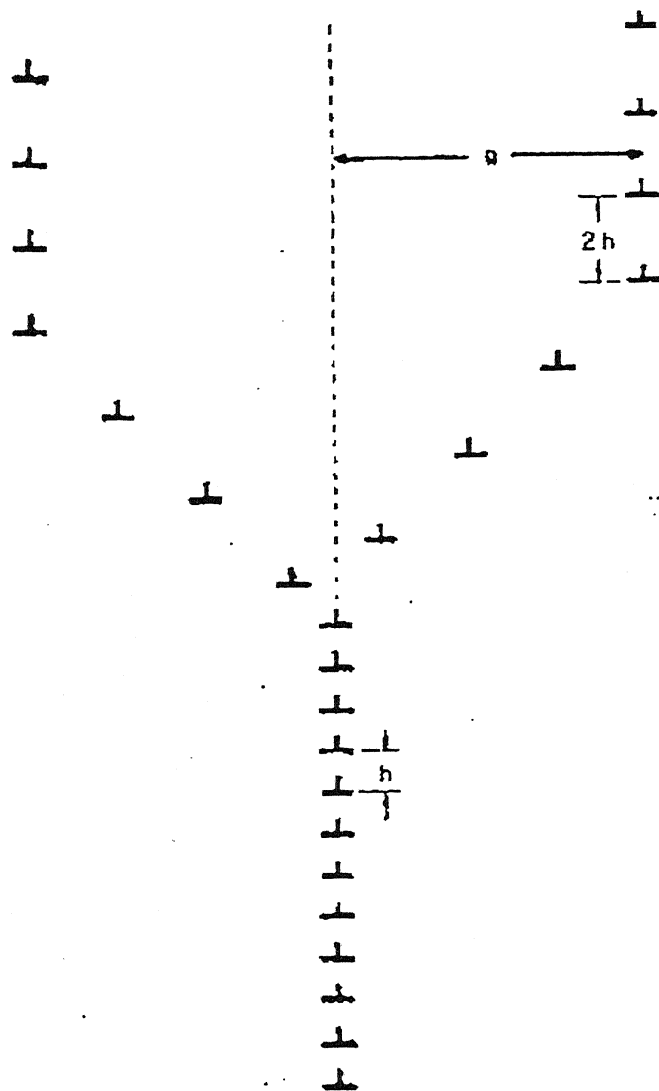
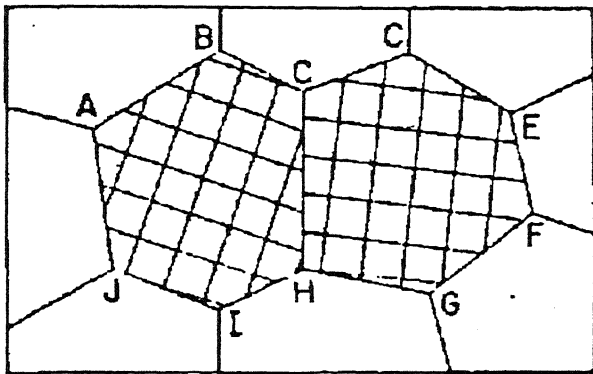
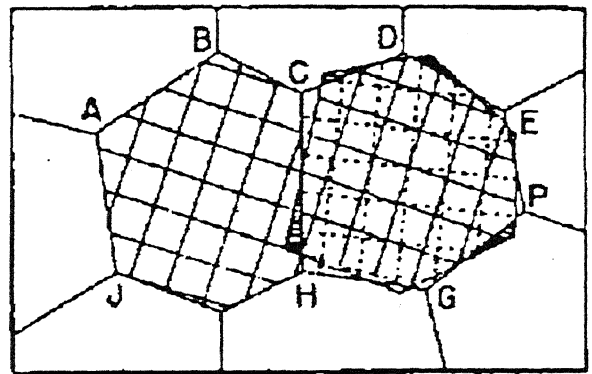


Figure 8. Dislocation structure at a Y-junction.



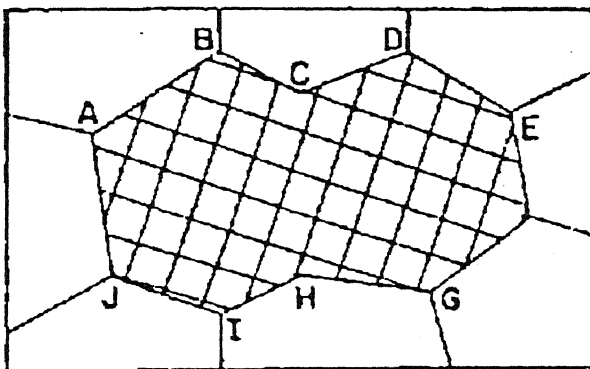
(a)

ORIGINAL SUBGRAIN STRUCTURE
BEFORE COALESCENCE



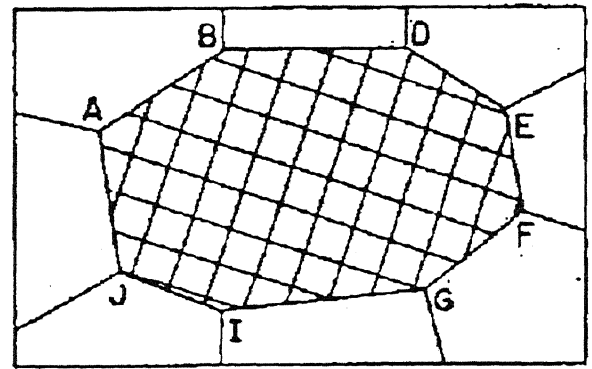
(b)

ONE SUBGRAIN IS UNDERGOING
A ROTATION



(c)

SUBGRAIN STRUCTURE JUST
AFTER COALESCENCE



(d)

FINAL SUBGRAIN STRUCTURE
AFTER SOME SUBBOUNDARY
MIGRATION

Figure 9. Schematic representation of sub-grain coalescence by sub-grain rotation.

The whole process probably requires some cooperative climb of dislocations along the disappearing sub-grain boundary and also some atom movements by vacancy diffusion around the sub-grains. The kinetics and thermodynamics of the coalescence process have been examined in detail by Li[20]

The energy of a sub-grain boundary, E , is related to the misorientation across it, θ , by the Read-Shockley equation[21]

$$E = E_0 \theta (A - \ln \theta) \quad (7)$$

Where, E_0 and A are both constants. An E versus θ plot is shown in Figure 10. This curve reaches a maximum when $\theta = e^{A-1}$. Hence,

$$E_{\max} = \theta_{\max} E_0 (A - \ln \theta_{\max}) \quad (8)$$

$$E_{\max} = \theta_{\max} E_0 \quad (9)$$

So, the equation (7) can now be also written as,

$$E / E_{\max} = \theta / \theta_{\max} (1 - \ln \theta / \theta_{\max}) \quad (10)$$

The equation (10) predicts that by lowering the misorientation across a sub-boundary the overall energy of the system is decreased. Li[20] considered the two neighbouring sub-groups of small misfit, could rotate naturally in a direction which enables low angle boundaries to decrease their angles of misfit.

2.5 Recrystallization

Recrystallization is a process in which grains of a given phase are replaced fully or partially by the same-phase grains having a lower energy. Recrystallization, like recovery, is a multi-stage process. The process can occur through the appearance and motion of high-angle boundaries (primary recrystallization) or only through the motion of such boundaries (grain growth and secondary recrystallization).

If a material in which primary recrystallization is completed is heated further at the same or a higher temperature, it will pass through the stage of grain growth and/or *secondary recrystallization*. In this process, grains which have grown from

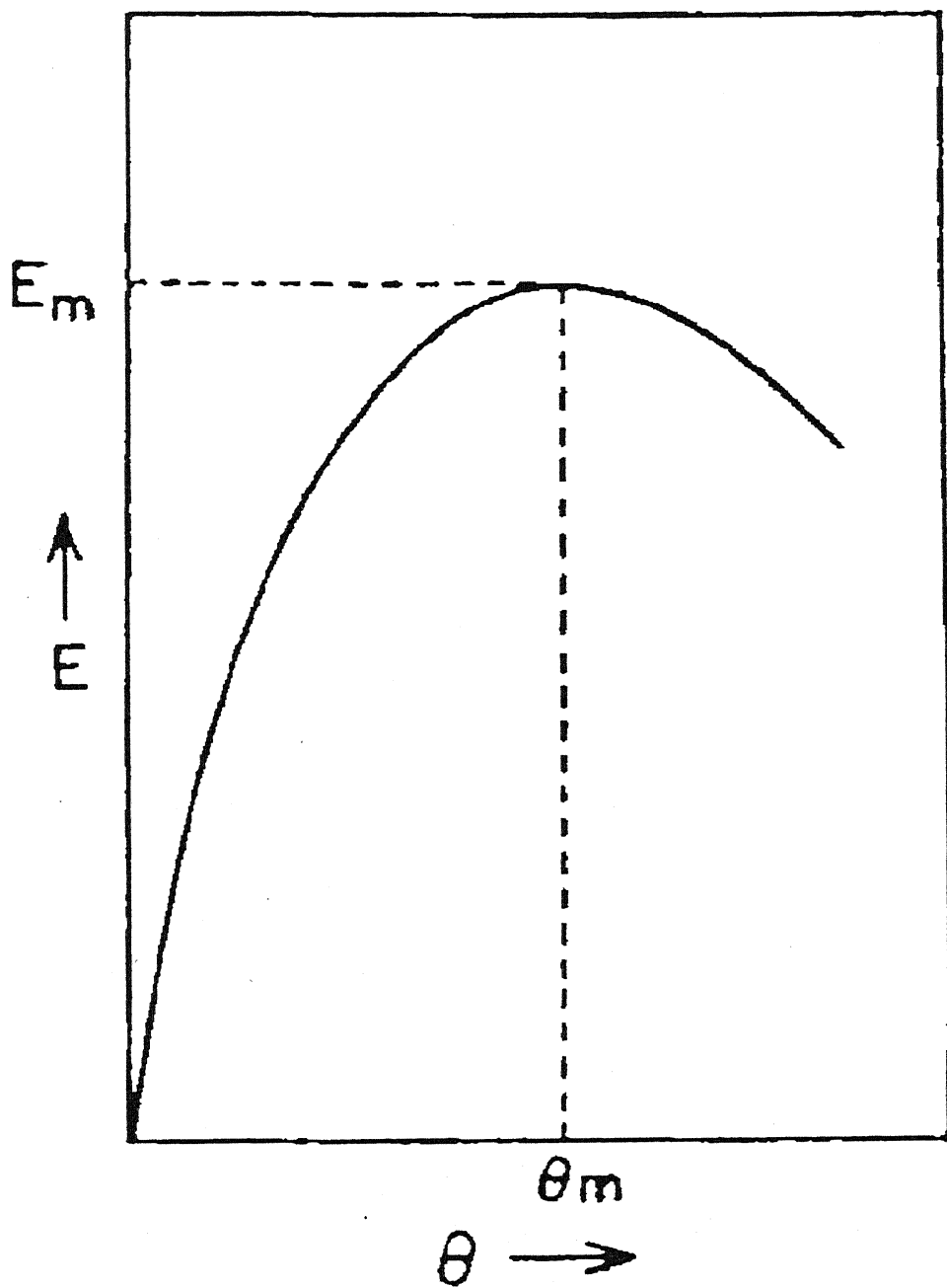


Figure 10. Plot of E vs θ .

primary recrystallization nuclei will grow further at the expense of their neighbours by migration of their high-angle boundaries. The size of grains and their distribution in size can vary upto the formation of single crystals (a rare but principally possible case), with their crystallographic orientation being also changed (recrystallization texture). These stages of recrystallization are also associated with reduction of the free energy of the system, though not so intensive as in primary recrystallization.

The difference between grain growth and secondary recrystallization consists in that the former process occurs uniformly whereas the latter does not since there are some grains which, for certain reasons, can grow at an appreciably higher speed than others and thus serve as secondary 'nuclei'.

2.5.1 Primary recrystallization

The first, most low-temperature, stage is called primary recrystallization. It can occur either immediately after polygonisation or at the same time with polygonisation occurring in the neighbouring portions. This stage reduces most radially the number of crystal structure defects introduced by prior deformation and accordingly the stored volume energy of deformation, up to full restoration of the structure and properties the material has had before the deformation.

The three principal models of nucleation are :

(i) *Classical nucleation model*

This model is based on the assumption that the nucleus which is stable and capable of growth is formed as a result of thermal fluctuations in the sense of the classical nucleation theory of phase transition. New grains should want to form only very small misfit angles with the matrix, since this would lead to lower values of the interfacial energy.

Thus plus point of this model is that it can account for existence of an incubation period. It also predicts the preferential nucleation of recrystallized grains in the most severely deformed regions. But on one of its disadvantage is that this theory predicts that new grains should always be close in orientation with respect to the adjacent cold-worked matrix. Another drawback of this theory is that no effect of

purity is allowed for, yet purity very often seems to be of paramount importance in recrystallization.

(ii) *Sub-grain growth model*

It is believed that by a process dislocation climb and rearrangement of small strain-free cells are formed in a deformed matrix from regions of high dislocation density. Once a sufficiently large dislocation free cell or sub-grain has formed it can grow into its neighbourhood.

Cahn[22] has suggested that when a sub-grain starts growing its boundaries sweep up most of the dislocations which they come in contact with. Thus, the periphery of a growing sub-grain acquires an even higher dislocation density. As the sub-boundary angle increases there varies a point at which the individual dislocation on a boundary begin to loose their identity and it is at this stage that the boundary changes its character from a sweeper up of dislocations to a destroyer of dislocations. With such a state of affairs the growth of the enlarging sub-grain may be expected to accelerate.

(iii) *Strain induced boundary migration*

Light microscopy by Beck and Sperry[23] showed that sometimes recrystallization does not involve any nucleation but only growth of strain-free regions brought about by grain-boundary migration. This process which has been termed as strain-induced boundary migration, consists of the irregular movement of an existing boundary with an irregular jagged front, shown schematically in Figure 13. This model of growth assumes that the unstable cold worked state already has large-angle boundaries of macroscopic or microscopic dimensions and that during recrystallization these boundaries simply bow out leaving strain-free material behind.

According to this model there is no incubation period, since no nucleus of new orientation has to be formed. Frequently it is observed that the victim grain is the one which is more severely work-hardened, the stored energy of this grain provides the driving force for the entire process. The grain with the larger cell-size will have the lower energy, so that recrystallization occurs by the movement of a portion of the boundary into the high energy grain having a smaller cell-size. According to

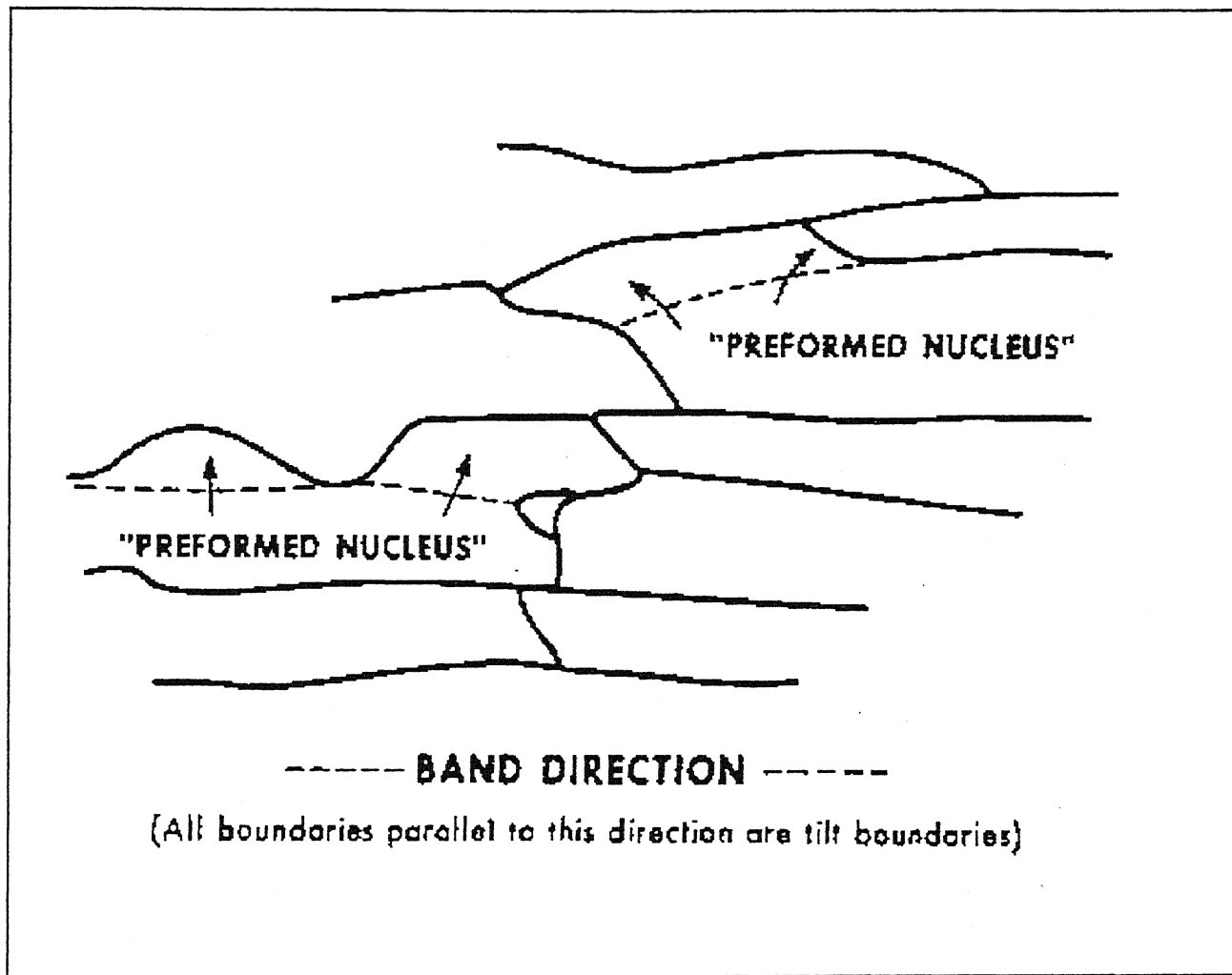
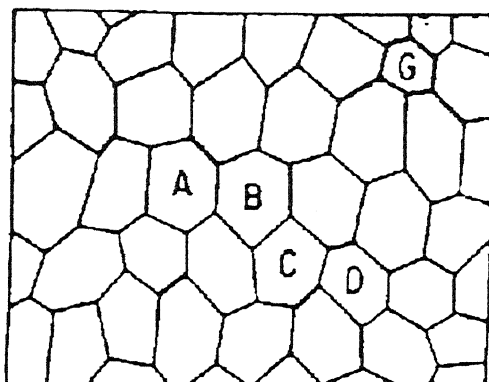
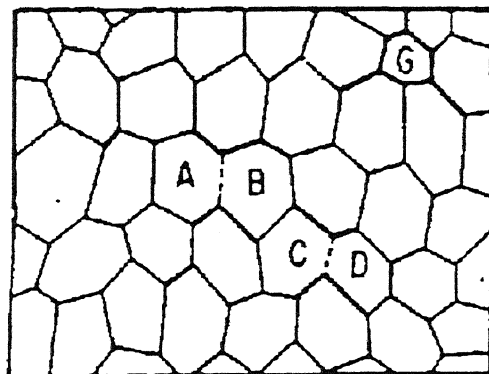


Figure 11. Nucleation by sub-grain growth in a deformation band.



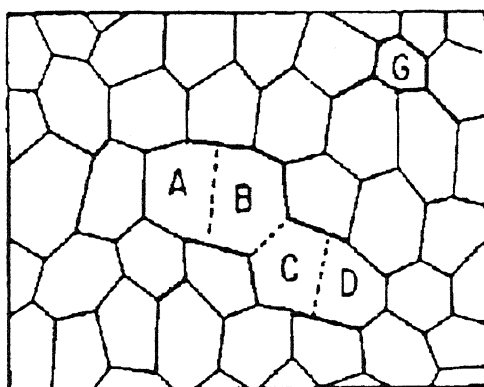
(a)

SUBGRAIN STRUCTURE BEFORE
NUCLEATION.



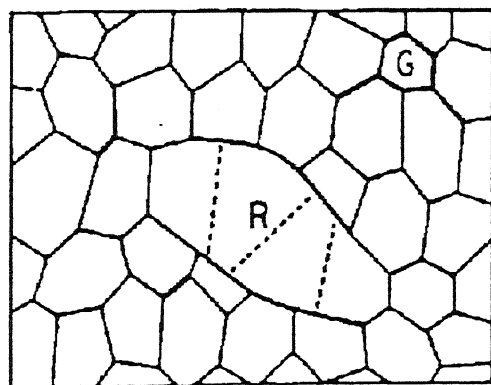
(b)

COALESCENCE OF SUBGRAIN A
AND B, AND C AND D.



(c)

FURTHER COALESCENCE OF
SUBGRAINS B AND C.



(d)

FORMATION OF A NUCLEUS WITH
HIGH ANGLE BOUNDARIES.

Figure 12. Schematic representation of the formation of a recrystallized grain by the coalescence of sub-grain.

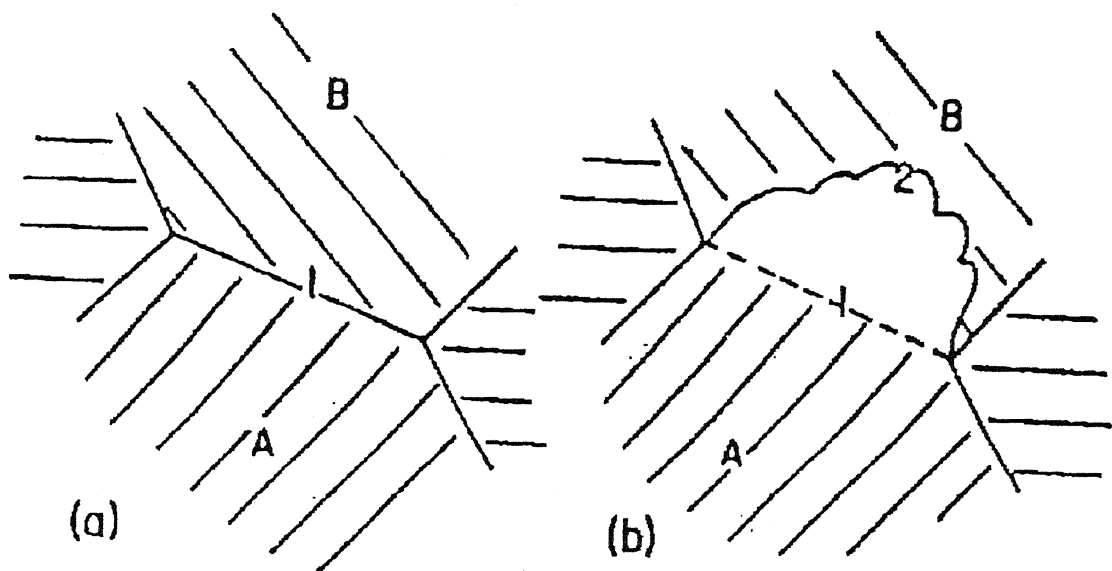


Figure 13. schematic Representation of strain induced boundary migration

(a) Configuration before annealing

(b) The Boundary between the cold worked grains A and B has migrated from position 1 to position 2.

Doherty[24], nucleation at a grain boundary by strain-induced boundary migration requires a heterogeneity of sub-grain size which was achieved (in Al) by sub-grain coalescence, but this coalescence only occurs where a deformation band was present. In iron reduced 40%, the heterogeneous strain allowed nucleation by a strain-induced boundary migration without the need of free coalescence.

Bailey[1] and Bailey and Hirsch[2] developed a simple model to analyze the energetics of this process. According to their model local regions of an original grain boundary migrate by bowing out into the shape of a spherical cap. Figure 14 shows how a length $2L$ of a grain boundary gradually bulges out to successively larger sizes. Bailey and Hirsch[2] have shown that growth rate of the recrystallizing grain can be written as,

$$\frac{dv}{dt} = Abf \left[E - \gamma \left(\frac{dA}{dv} \right) \right] \quad (11)$$

where, v = volume of the recrystallizing grain

A = area of the recrystallizing grain

E = difference in stored energy per unit volume across the migrating boundary

γ = specific grain boundary energy

b^3 = volume occupied by one atom

and

$$f = \left(\frac{\nu k}{RT} \right) \exp \left(\frac{-F_a}{RT} \right) \quad (12)$$

where ΔF_a = free energy difference per gram-atom between an atom in the initial state and the new activated state

R = gas constant

T = absolute temperature

K = atomic weight / density

and ν = atomic jump frequency.

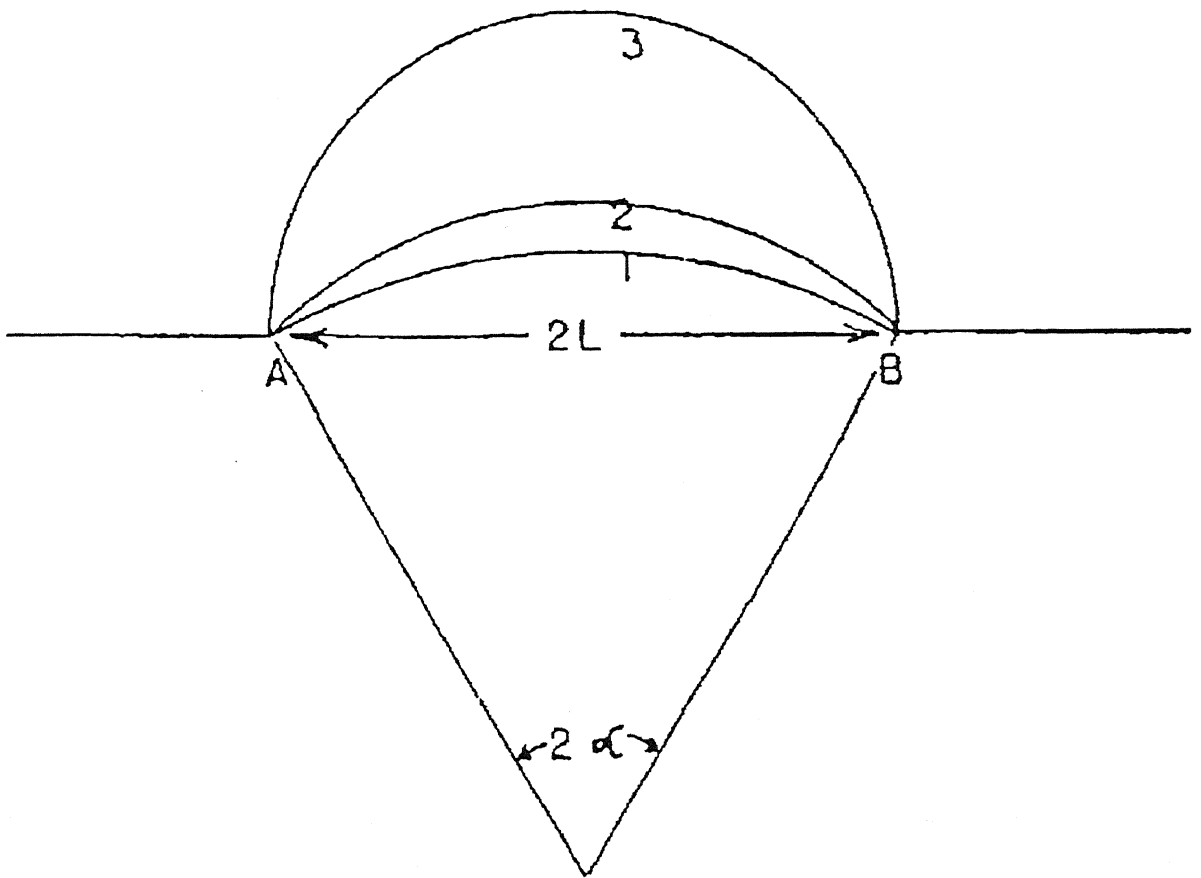


Figure 14. Model for high angle grain boundary migration process in recrystallization.

It has been shown that the condition for growth to occur can be given by the expression

$$L > \frac{2\gamma}{E} \quad (13)$$

Bailey and Hirsch found this criterion to be approximately satisfied in their own work on cold-rolled deformed silver.

2.5.1.a Grain boundary migration

Grain boundary migration is known to play an essential role in recrystallization and subsequent grain growth. A grain boundary may be defined as a layer of distorted material which is the result of atomic mismatch between two adjoining crystals of different orientations.

2.5.1.b Orientation dependence of boundary migration

Studies on the growth of new grains in strained single crystals have convincingly demonstrated that growth can be orientation dependent. This points to the fact that there is a marked orientation dependence of grain boundary migration. The highest migration rate in f.c.c. metals has been obtained when the growing grain is crystallographically related to the matrix by a 30°-40° rotation about a common $\langle 111 \rangle$ axis[25,26].

More work done on lead[27-29], aluminium[30] and copper[31] has shown that for very high purity zone-refined metals there is practically no preferred orientation relationship for high mobility, at least at high temperature.

In principle, the anisotropy of the boundary migration rate can be interpreted as due to the orientation dependence of either the driving force or the boundary mobility. In highly deformed materials which show a complex dislocation structure, the anisotropy of driving force can be ruled out as a possibility and hence an orientation dependence of boundary mobility is quite expected.

Theoretical treatments of the effect of impurities on grain boundary mobility have been presented by Cahn[32]. The theory is based on a common assumption that there is an interaction between the impurity atoms and the grain boundary and that during migration the solute atoms have to travel along with the boundary. If the

driving force is large enough to overcome the dragging effect of the impurities then the boundary might breakaway from the impurity atmosphere and this according to all theories will increase the mobility considerably.

According to Ray[33], recrystallization was found to be easier in foils made from the transverse and longitudinal sections than from ones parallel to the rolling plane. This is due to the fact that the cells produced by deformation are pancaked shaped with the cell boundaries lying nearly parallel to the rolling plane. Foils which were taken parallel to this plane may not contain a sufficient number of cells through the thickness to allow formation of a recrystallization nucleus with a high-angle boundary. In such foils growth may also be inhibited.

During initial stages of annealing of pure Cu, in the rolling plane section, the small grains having the orientation $(110)[1\bar{1}2]$ were found to nucleate in situ. In the later stages, however, cube-oriented grains appear to engulf small grains of the orientations. In contrast to rolling plane sections in transverse section foils of pure Cu $(110)[1\bar{1}2]$ oriented grains are found to grow to large sizes[33].

According to Novikov[34], the kinetics of secondary recrystallization is affected by (a) the value and the behaviour of pinning force and (b) the magnitude of the driving force for grain growth. The former depends on the volume fraction, the dispersion and the nature of the fine precipitates. The later is influenced by initial grain size distribution and the curvature of the moving boundaries. The two dimensional growth slows down the secondary recrystallization when the initial average grain size exceeds $1 / 10^{\text{th}}$ of the sheet thickness[34].

2.6 Continuous Grain Growth

Grain growth refers to the increase in the average grain size on further annealing, after all the cold worked material has recrystallized. As a reduction in the grain boundary area per unit volume of the material occurs during grain growth, there is a decrease in the free energy of the material.

Continuous grain coarsening is a recrystallization process which proceeds without nucleation[35]. Textures formed during this process are thus exclusively due to the orientation dependence of the grain boundary velocity which is the product of the driving force and grain boundary mobility. The mobility of a boundary depends

among others, on the orientation difference Δg_o of the continuous grains. The driving force in the grain coarsening is constituted by the deviation from equilibrium between the forces exerted by the grain boundaries a and b respectively as shown in Figure 15(a). These forces also depend on the orientation difference of the contiguous grains, i.e., g_o and g_{io} for a-boundaries and g_{io} and g_{jo} for the b-boundaries. In order to reduce the deviation from the equilibrium state, the system lowers its free energy by enlarging the grains, thereby reducing the surface free energy. So this is essentially a process, where a grain of a favoured orientation consumes other grains of unfavorable orientations. The interface boundary as shown in Figure 15(b) moves from region 2 to region 1.

Assumption : The grains are spherical

Now dn moles of material is transferred from 1 to 2 as a result of which size of 2 is increased. Chemical free energy is same for both regions.

Δg : free energy change per mole

Total change of free energy = change in surface area \times surface energy

$$\text{so, } \Delta g \, dn = dA \, \sigma \quad (14)$$

Let V_o be the molar volume. Then the change in volume of region 2 due to transfer of

$$dn \text{ moles} = V_o \, dn = dV$$

$$\text{or } dn = dV / V_o = 4\pi R^2 \, dR / V_o$$

$$\text{Now } V = 4\pi R^3 / 3 \text{ and } A = 4\pi R^2$$

$$\text{Therefore, } \Delta g \, 4\pi R^2 \, dR / V_o = \sigma \, 8\pi R \, dR$$

$$\text{Hence, } \Delta g = 2 \, \sigma \, V_o / R = 4 \, \sigma \, V_o / D \quad (15)$$

For a given system V_o and σ are constant. So $\Delta g \propto \frac{1}{D}$

During the grain coarsening the rate of increase of size $= \frac{dD}{dt}$

$$\text{Now growth rate } G = - V_o \, n \, A \, \nu \exp \left(\frac{-\Delta G}{kT} \right) \frac{\Delta g}{kT} \quad (16)$$

Where ΔG = energy barrier and ν = vibration frequency of atoms. For a given

$$\text{temperature } G \propto \Delta g, \text{ others being constant. So } G \propto \Delta g \propto \frac{1}{D} \text{ or } G = \frac{dD}{dt} = \frac{k}{D} \quad (17)$$

which gives $D \, dD = k \, dt$, integrating the relation we have $D^2 = kt$. Now general

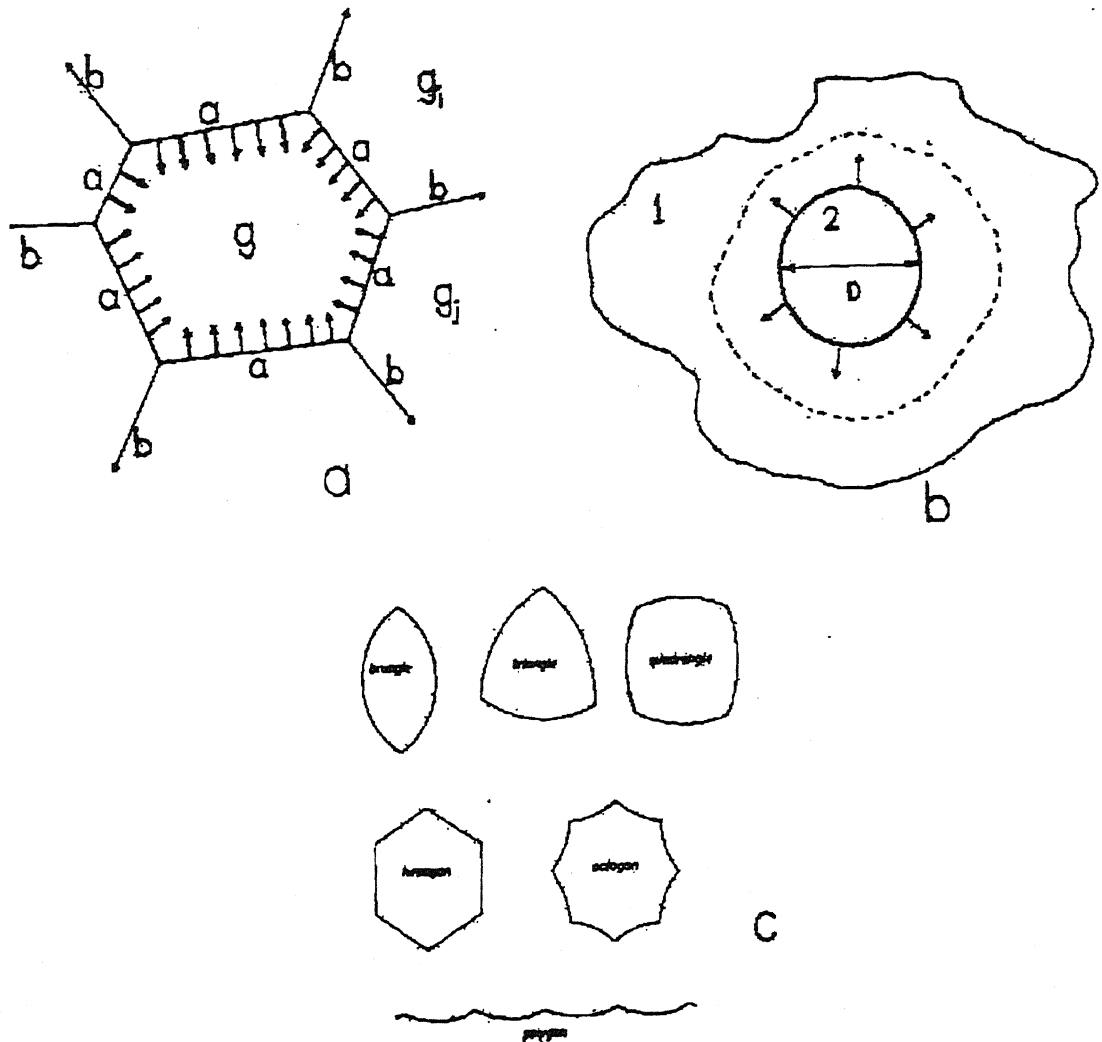


Figure 15(a). A grain of the orientation g is surrounded by grains of the orientations g_i and g_j . The energy of the a -boundaries tends to contract the grain whereas the b -boundaries tend to expand it

Figure 15(b). Growth of region 2 by the movement of interface boundary from region 2 to region 1

Figure 15(c). Curvature of grain boundaries in n -sided two dimensional grains.

relation is $D = k t^n$, $n = 0.5$ for ideal spherical shaped grains. In real situation, the value of n is observed to be less than 0.5. Usually values $n < 0.5$ were observed which were generally ascribed to the drag caused by dissolved or precipitated foreign atoms[36].

For an individual grain boundary it is not definite which way it should move so that the average grain size may increase. It will instead move towards its individual mean centre of curvature. This is determined by the condition that in equilibrium the three boundaries forming a grain edge should intersect at angles of 120° . Figure 15(c) shows in the two dimensional example that this condition gives small grains (having few sides) convex boundaries and large grains (having many sides) concave boundaries, so that larger grains will tend to grow at the expense of smaller ones. Once again, grain boundary curvature serves as the means to spread the localized driving forces over the boundary area.

2.7 Preferred Orientation or Texture

2.7.1 Introduction

The common metals of industrial practice are polycrystalline aggregates in which each of the individual grains has an orientation that differs from those of its neighbours. It is quite unusual for the grains in such metals to have a random distribution of orientations, and the non-random distributions that occur are called *preferred Orientations* or *Textures*. Textures are developed at all stages of the manufacturing process of metals but the precise nature of the texture is a complex function of the mechanical and thermal treatments as well as the material itself.

2.7.2 Determination of Texture

Rolling plane of the material and rolling direction (crystallographic planes and direction) are needed for the determination of texture. For example, a sheet is rolled on such a way that its rolling plane is (hkl) and direction is $[uvw]$, then its texture is represented as $\{hkl\} \langle uvw \rangle$, as shown in Figure 16. This is displayed by a *pole figure* which is nothing but the stereographic projection on the (hkl) plane, taking (uvw) pole as the north pole. The experimental procedure of the pole figure construction is briefly

(100) poles for the orientation $\{110\}\langle 001 \rangle$

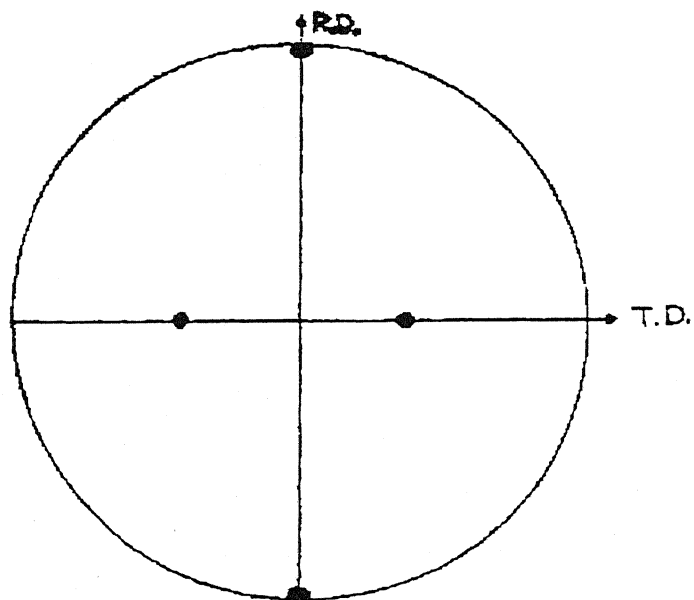
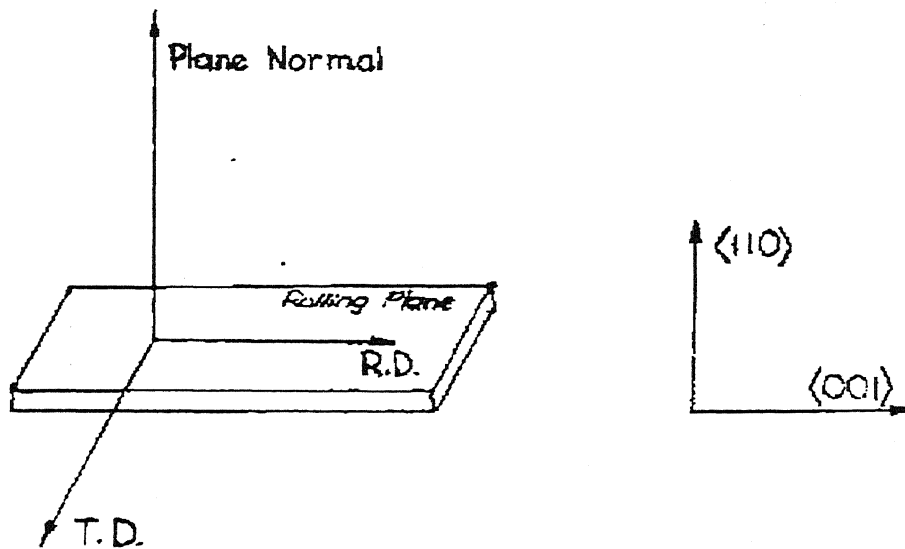


Figure 16. The rolling plane and rolling direction in a metal sheet subjected to rolling.

shown in Figure 17. The material is first subjected to X-ray diffraction, and the intensity vs. angle data is recorded. Then these data is transformed from a linear scale to a polar plot (pole figure). Several contours shown on the pole figure account for the different orientations of different densities.

There are few limitations of pole figure. Although exhibiting all the texture components of a material, in a pole figure, the pole of particular texture is not pinpointed, rather it is scattered throughout a zone and it becomes difficult to distinguish them perfectly. The resolution of pole figure is poor. Also, it gives only some qualitative idea about the strength of a particular texture component.

In order to overcome these problems another technique is frequently applied. The data they are represented in numerical, which is known as *orientation distribution function* (ODF). It is easily understood that a frame of three mutually perpendicular axes can be superimposed on another frame of three mutually perpendicular axes. The same principle is followed here, the specimen frame as shown in Figure 18(a) is superimposed on the crystallographic frame by means of three successive rotations (Figure 18(b)).

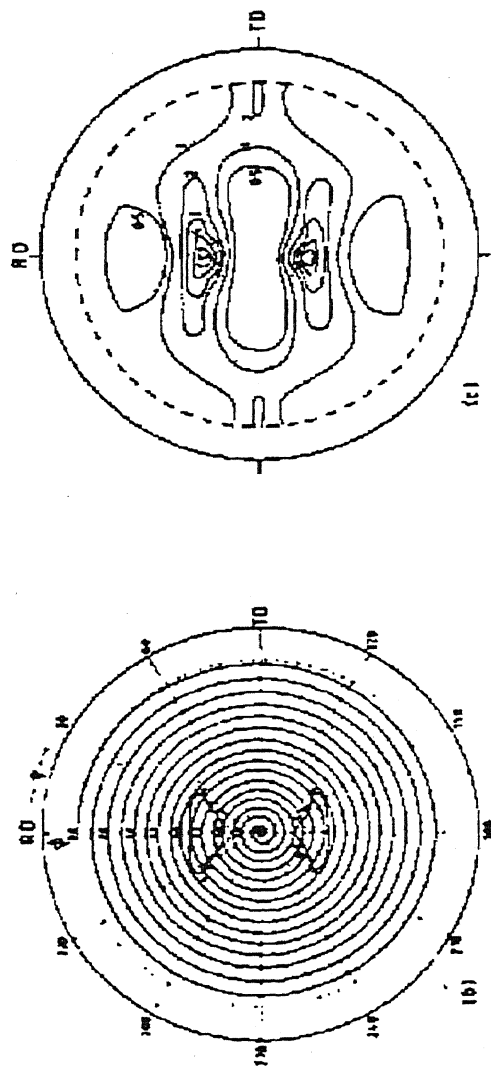
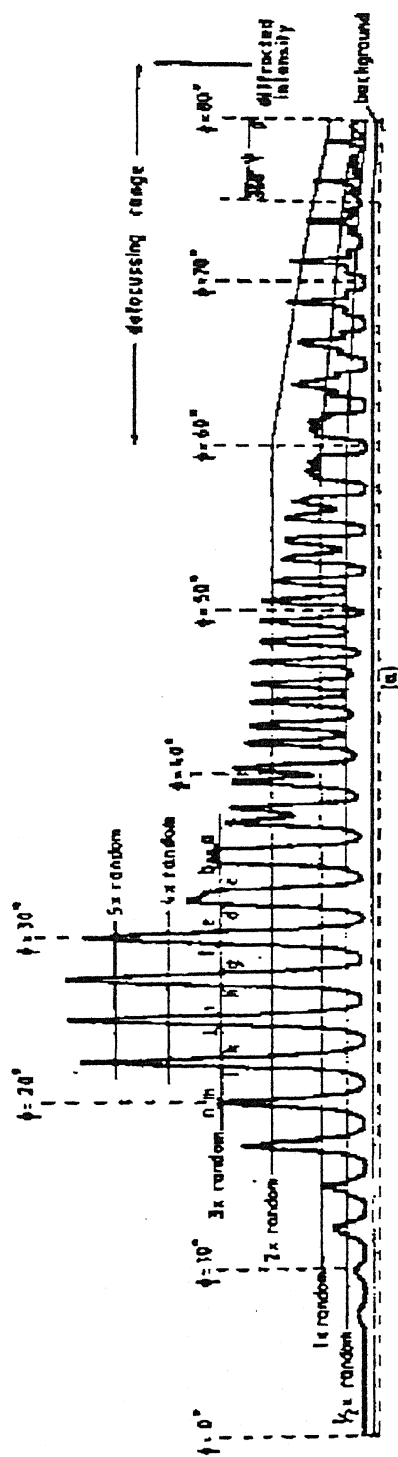
(a) A first rotation Φ_1 around ND transforms TD and RD into the new directions TD_1 and RD_1 respectively. Φ_1 has to have such a value that RD_1 will be perpendicular to the plane formed by ND and [001].

(b) A second rotation Φ around the new direction RD_1 with Φ having such a value that ND is transformed into [001] and TD into TD_2 .

(c) The third rotation Φ_2 with Φ_2 having such a value that RD_1 is transformed into [100] and TD_2 into [010].

So, Φ_1, Φ, Φ_2 ; the set of these three angles completely represent the orientation of a particular texture. Immediately for every set of $\{hkl\} \langle uvw \rangle$ values there is exactly one set of Φ_1, Φ, Φ_2 values. Now depending on this concept, a three dimensional space has been evaluated where three mutually perpendicular axes represent the values of Φ_1, Φ, Φ_2 ; from 0° to 90° . This is known as orientation space (Figure 18(c)), and widely used for universal texture notation [37].

The ODF technique is not more correct process than the pole figure technique is, but of course, the resolution is much higher in this system, and also it allows the quantitative measurement of the strength of a particular texture component in volume fraction.



(a) chart recording for the (111) reflection of cold rolled aluminium (compressed scale), (b) partly plotted pole figure showing the 3 x random contour, (c) final (111) pole figure.

Figure 17. schematic illustration of pole figure construction

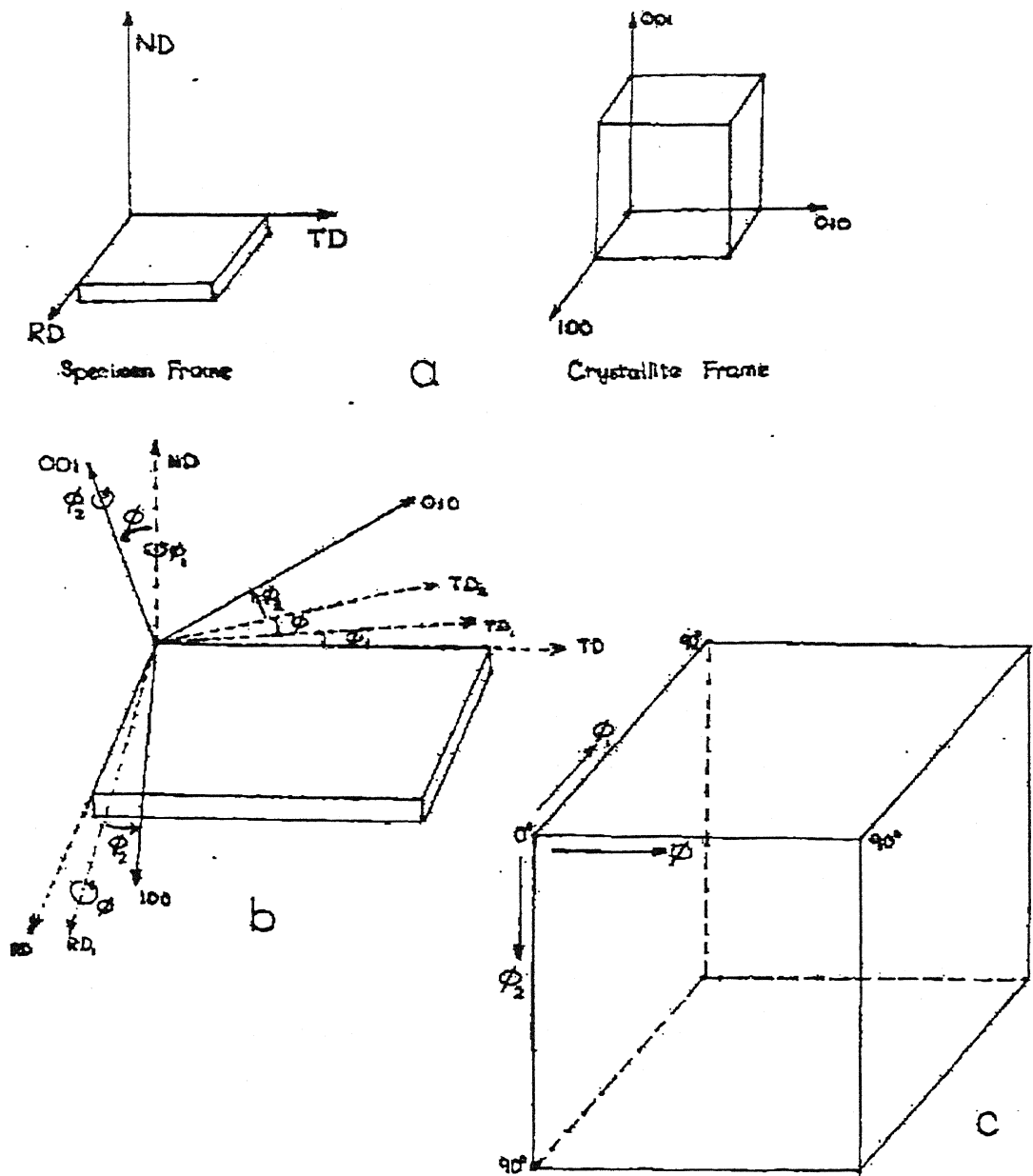


Figure 18(a). Specimen frame and crystallite frame

Figure 18(b). The rotations for superimposing crystallite frame on reference frame

Figure 18(c). Orientation space.

2.7.3 Rolling Texture

A random polycrystalline aggregate will develop preferred orientations, or textures, upon sufficient plastic deformation. The nature of the deformation texture depends essentially on the crystal structure of the metal and the characteristics of the flow. Many other factors, such as the initial texture, the chemical composition, the previous thermal or mechanical treatment, the temperature, rate, or physical constraints during deformation, may all affect the resulting texture to some extent. The fact that in a polycrystalline aggregate a texture develops only gradually with increasing deformation suggests that individual grains rotate into specific orientations at various stages during the deformation process. Once a grain has assumed the specific orientation, additional deformation does not alter its orientation. Thus, a texture is finally developed in the metal [38].

Deformation textures have their origins in the crystallographic nature of the common deformation processes of slip and twinning. Where large strains are involved, slip is usually the major factor but twinning can also be highly significant in texture development because of the massive re-orientations that are involved. During the slip process the crystal lattice rotates as a result of the shape change and the geometrical constraints of its surroundings. The restricted number of slip systems available produces rotations towards a limited number of end-points and so a deformation texture is produced. It is clear that the resulting texture will depend on the nature of the imposed stress (or strain) system, the extent of deformation, and the operative deformation modes which are themselves defined by the crystal structure and atomic bonding.

2.7.4 Annealing Texture

Annealing of cold worked metals is usually discussed in terms of three consecutive but overlapping processes, viz. Recovery, recrystallization and grain growth. In the first of these, most of the excess point defects are removed and the dislocations rearranged somewhat but there is virtually no change of texture. During recrystallization new grains are nucleated and grow at the expense of the cold worked matrix by migration of high angle grain boundaries. Locally there are large changes in orientation and the texture as a whole is modified to become a *primary*

recrystallization texture. There are frequently, but not always, components of texture which are common to both the deformed and recrystallized states. After recrystallization is complete grain growth occurs involving further grain boundary movement. If this process is normal and continuous there is a gradual change in texture, but if grain growth is abnormal or discontinuous only a few grains grow (to a very large size) and the texture change may be great. This latter process is sometimes called secondary recrystallization and usually results from the existence of a dispersion of second phase particles in the structure. However, secondary recrystallization may also occur in single phase metals and in such cases a necessary condition is the presence of a very strong primary recrystallization texture[39].

2.7.5 Rolling Texture and Annealing Texture of Ni-Co alloys

For higher stacking fault energy, the stacking fault width is very low, and the stacking faults are easily constricted. In that situation, the cross-slip becomes easier and the material undergoes slip deformation rather than twinning. When the deformation is governed by slip mode, the deformation texture is generally copper type $\{112\}\langle 111 \rangle$. Example, pure copper, pure nickel or nickel with low amount of cobalt, etc. The (111) pole figure for 95% cold rolled pure copper is shown in Figure 19(a). Along with the copper components of texture other components like Bs component $\{110\}\langle 112 \rangle$, S component $\{123\}\langle 634 \rangle$, Goss component $\{110\}\langle 001 \rangle$ etc, are present in very small percentage. The materials with lower SFE predominantly exhibit Bs type of texture. For lower SFE, the stacking fault width is much greater, which makes it difficult to create any constriction within the stacking fault region and the cross-slip becomes difficult. As a result of it, the critical resolved shear stress (CRSS) for twin becomes lower than that of slip and the plastic deformation is essentially governed by the twinning process. Figure 19(b) exhibits the typical Bs type texture of a Ni-Co alloy with a lower SFE.

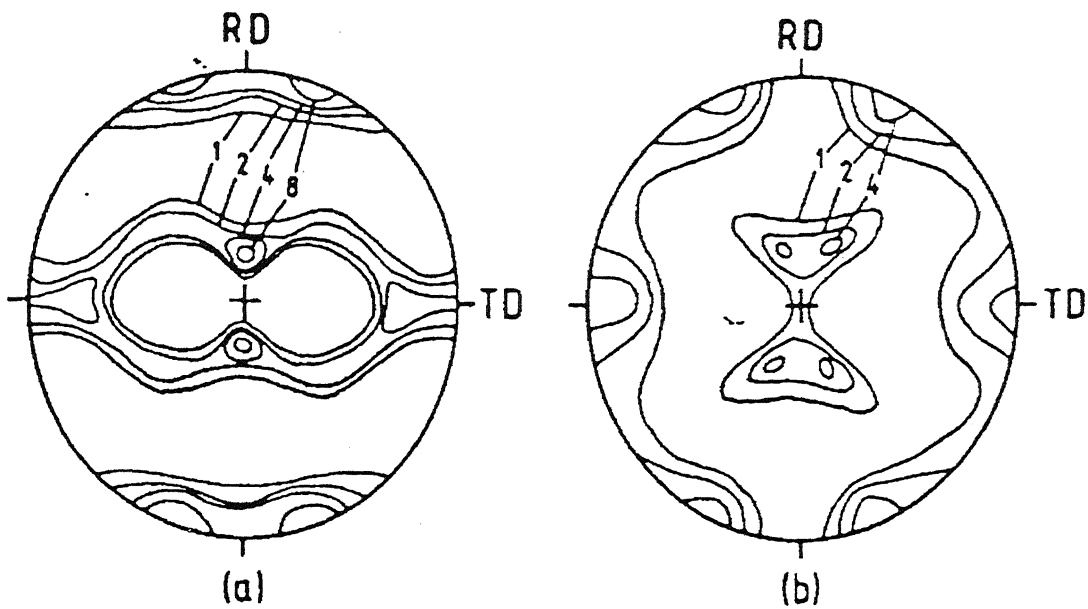


Figure 19. (111) pole figure of pure Cu (a) and 70:30 brass (b).

In Ni-Co alloy system, the SFE significantly decreases on increasing the Co percentage. Accordingly it is observed that the Cu component of rolling texture gradually decreases from pure nickel to Ni-30% Co (Figure 20). Ni-40 Co alloy shows a transition from Cu type to Bs type rolling texture, and Ni-60 Co alloy predominantly exhibits Bs type texture (Figure 21). This is also observed by Ray[40] that Cu type texture decreases with increasing amount of deformation. In case of Ni-40 Co alloy, the intensity of Cu type texture remarkably decreased from 40% cold rolling to 95% cold rolling.

In the ODFs of f.c.c. metals and alloys, three fibre textures have been generally recognized. These are

- (a) an α -fibre which extends from the Goss orientation $\{011\}\langle 100 \rangle$ through the Bs orientation $\{011\}\langle 211 \rangle$ to $\{011\}\langle 011 \rangle$;
- (b) a τ -fibre which extends from $\{001\}\langle 110 \rangle$ through the Cu position $\{112\}\langle 111 \rangle$ and going up to the Goss orientation $\{011\}\langle 100 \rangle$;
- (c) a β -fibre which runs from the Cu position $\{112\}\langle 111 \rangle$, through the S orientation $\{123\}\langle 634 \rangle$ and meets the α -fibre at the Bs position, shown in Figure 22.

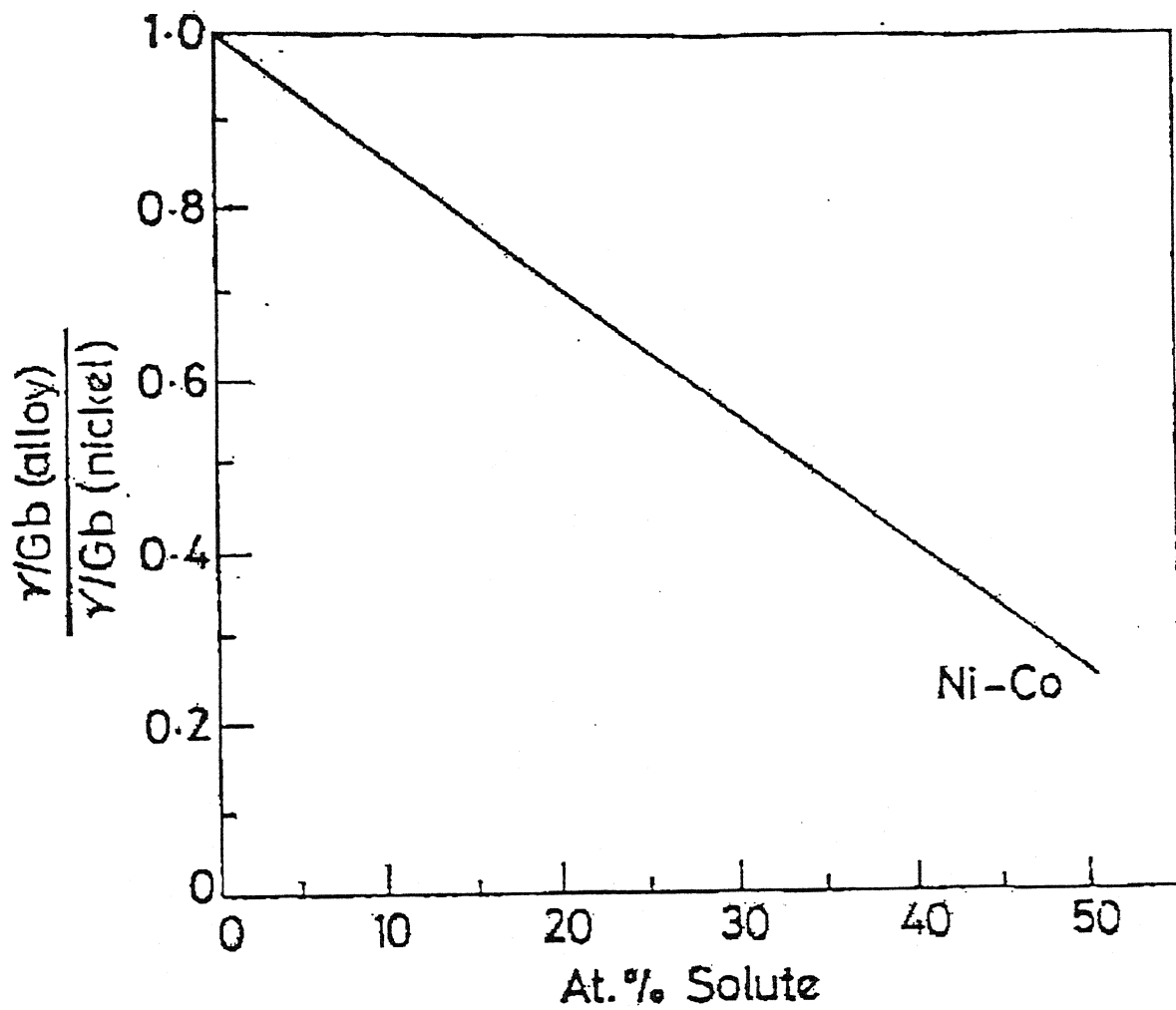


Figure 20. Effect of composition on stacking fault energy.

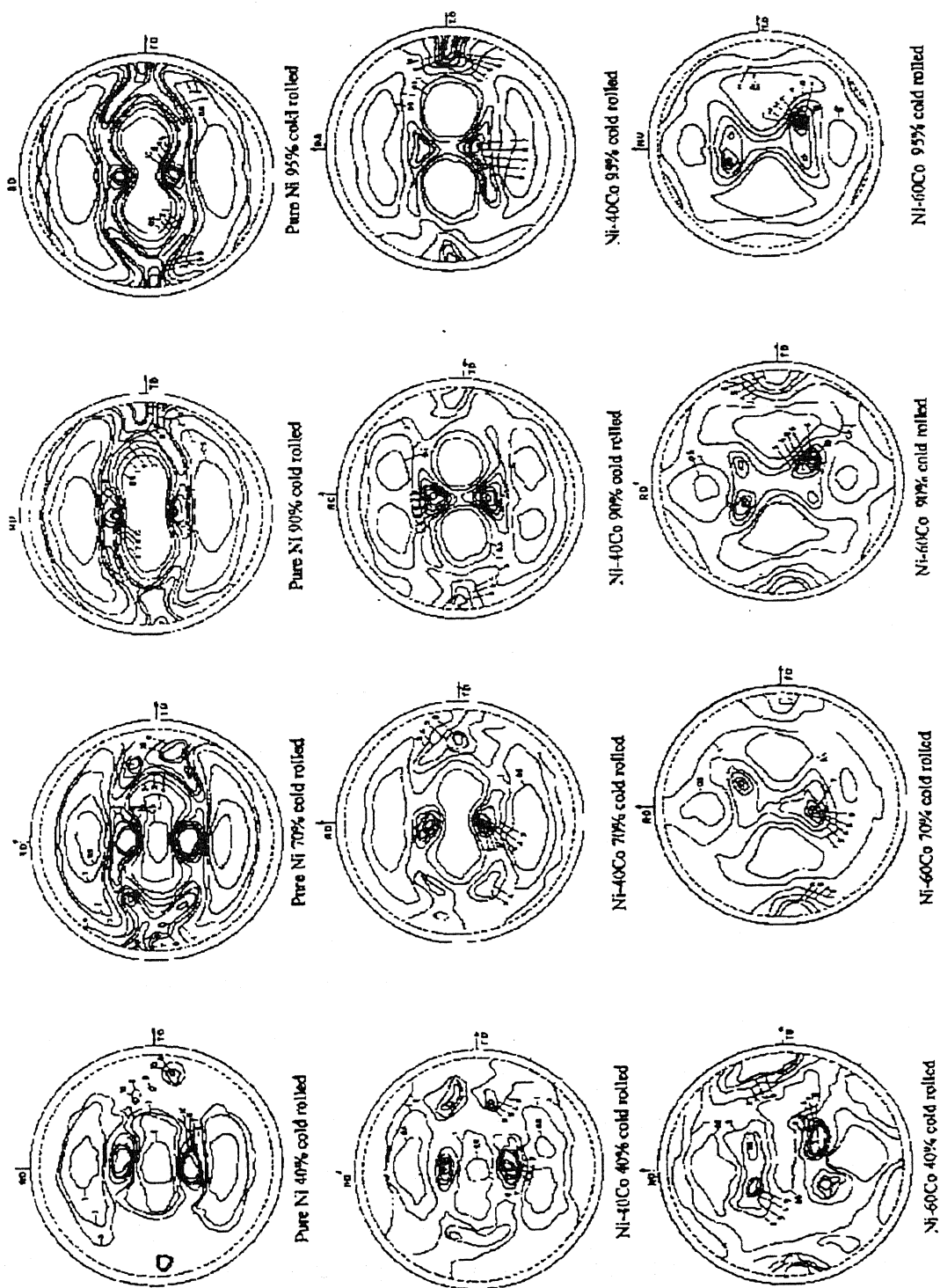


Figure 21. (111) pole figures showing the cold rolling textures developed in pure Ni and Ni-Co alloys.

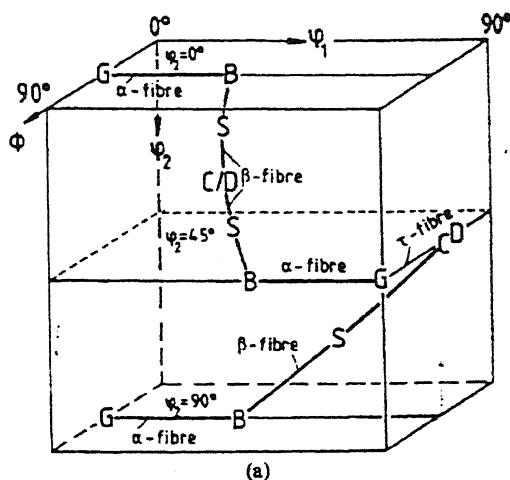


Figure 22. Position of the α , β and τ texture fibres in the Euler space.

An analysis of the ODF results for the Ni-Co alloys shows significant difference in the rolling texture of these alloys as a function of Co-content. The detailed analyses of the ODF results of pure Ni and Ni-Co alloys, done by Ray, are depicted in Figure 23 (a and d), shows that Ni-Co alloys with up to 30% cobalt, which show copper-type textures, exhibit only an inhomogeneous α -fibre or α -tube, but a strong and reasonably homogeneous β -tube. In the Ni-40% Co alloy the α -tube also is found to be reasonably strongly developed and this becomes more intense in the Ni-60% Co alloy. The intensity of the Goss position also improves in these two alloys. For convenience, an auxiliary Bs/Goss component, $\{011\}\langle 511 \rangle$, is introduced between the Bs and the Goss positions. Increase in Co-content leads to a systematic decrease in the $f(g)$ value of the Cu orientation, shown in Figure 23 (b). In fact, the intensity of the Cu orientation is very weak in the Ni-40% Co alloy and it is practically non-existent in the Ni-60% Co alloy. Furthermore, the twin Cu position shows a slight maximum for both the Ni-40% Co and Ni-60% Co alloys, but the positions of these maxima are found to be somewhat shifted towards the $\{332\}\langle 113 \rangle$ position. Figure 23 (d) shows that the positions of the texture components along the β -tube vary substantially depending on the Co-content of the alloys. In general, the

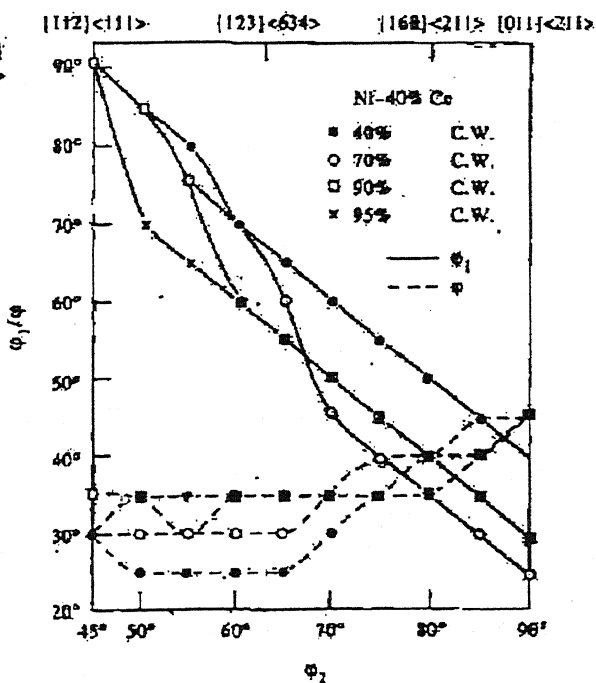
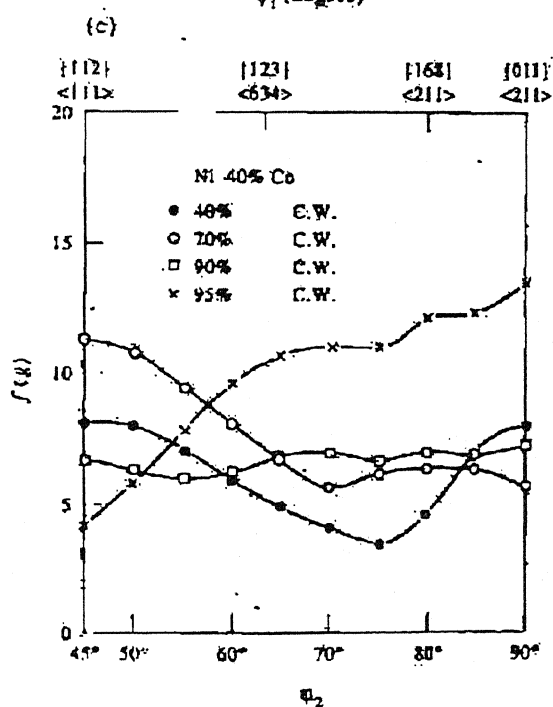
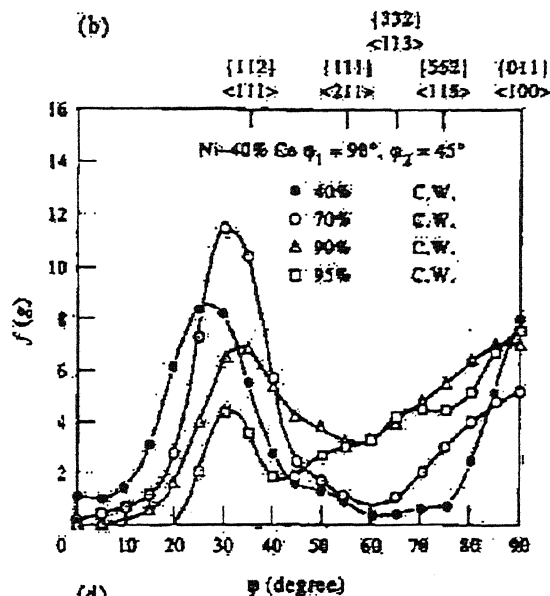
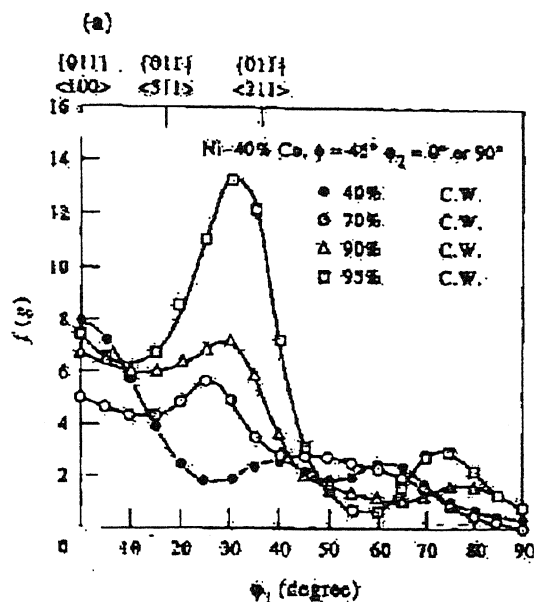


Figure 23(a). Plot of $f(g)$ vs ϕ_1 along the line $\phi = 45^\circ$, $\phi_2 = 0$ or 90° , Ni-40% Co

Figure 23(b). Plot of $f(g)$ vs ϕ along the line $\phi_1 = 90^\circ$, $\phi_2 = 45^\circ$, Ni-40% Co alloy

Figure 23(c). Plot of $f(g)$ vs ϕ_2 , Ni-40% Co alloy

Figure 23(d). Plot of ϕ_1/ϕ vs ϕ_2 , Ni-40% Co alloy.

locations of the texture components shift to lower Φ_1 and higher Φ values with increasing Co-content.

Wasserman has shown that if mechanical twinning is an available mode of deformation in addition to normal slip, the Cu component of the rolling texture $\{112\}\langle 111 \rangle$ will be transformed to $\{552\}\langle 115 \rangle$ by twinning. Further deformation of the twin orientation will then take place on the favourable slip systems which will rotate this twin orientation into the Goss position $\{011\}\langle 100 \rangle$ and finally in the Bs position $\{011\}\langle 112 \rangle$ by further rotation. In contrast, the major component of the alloy type texture will not be affected by twinning and retain its orientation during deformation.

In Ni-40% Co alloy, there are a host of orientations which do not contribute to the major texture components as such but constitute a large "random" background. The alloy in the transition range, Ni-40% Co, is likely to be the one where both slip and twinning will be taking place, probably with equal ease. As a result, there will be much more fragmentation of the grains in this case during deformation which will produce orientations that are widely scattered. This will eventually lead to a much sharper "background" texture component, shown in Figure 24.

Temperature also plays an important role for determining the rolling texture. The slip systems are activated in larger extent at high temperature, slip deformation is more probable than twinning. Exactly, the reverse effect is expected at lower temperatures. Pure copper which on rolling at room temperature gives very sharp Cu type texture exhibits totally Bs type texture when it is rolled at liquid nitrogen temperature.

On annealing a deformed material, the rolling texture completely or partially changes to a new texture, which is the recrystallization or annealing texture. It is also observed, that there is one-to-one correspondence between the rolling texture and annealing texture. So it can be inferred that the ultimate annealing texture of the material is dependent on the following factors:

- (a) Deformation mode
- (b) Degree of deformation
- (c) Temperature at which the rolling is carried out
- (d) Stacking fault energy
- (e) Critical resolved shear stress for slip and twinning.

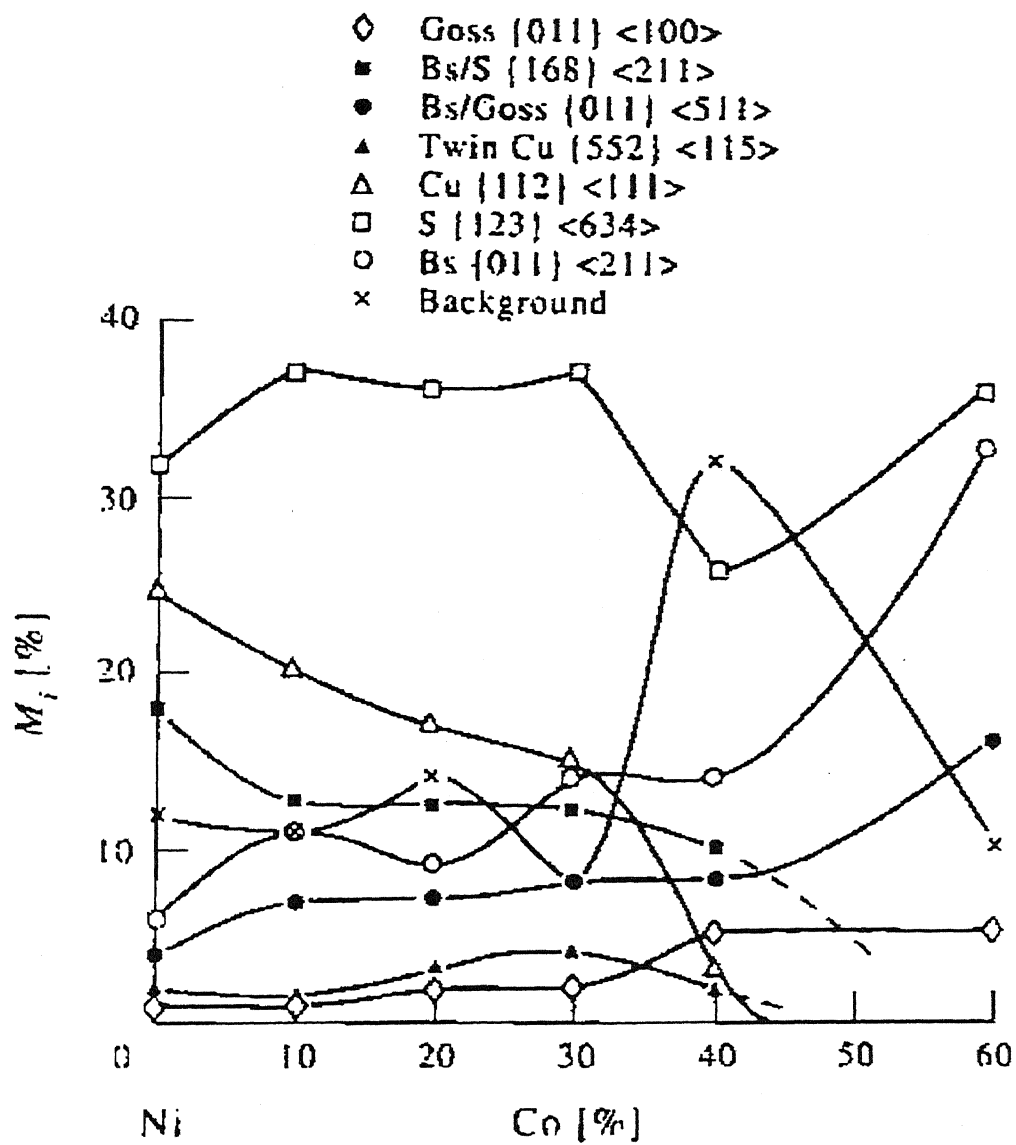


Figure 24. Plot showing the variation of M_i with % Co in Ni-Co alloys.

2.7.6 Recrystallization and Cube Texture

When the cold worked metal is annealed, the Cu type texture essentially changes to cube texture $\{100\}\langle 001\rangle$. This is a familiar phenomenon for the pure f.c.c. metals like Cu, Ni etc. except Al.

The reverse effect is observed in case of Bs type rolling texture. On recrystallization it does not yield Cu type texture. In a series of Ni-Co alloys, it has

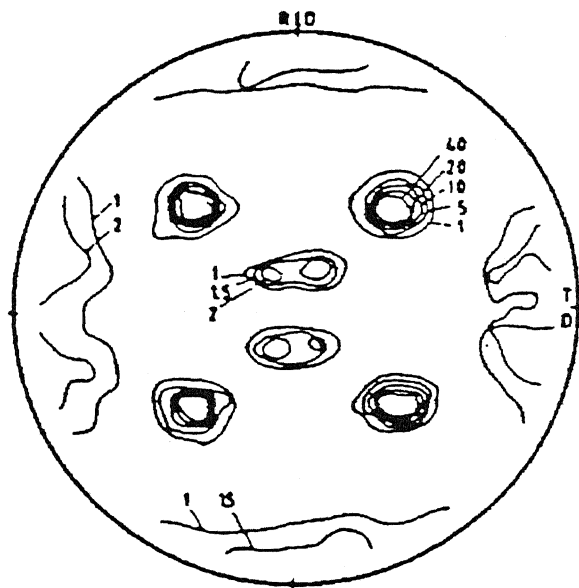


Figure 25. Typical Cube Texture in Nickel, $\{111\}$ poles shown in $\{100\}\langle 001\rangle$ texture.

already been observed that the compositions having higher magnitude of SFE (0, 10, 20, 30 % Co) yield cube texture. Composition of low SFE (Ni-60 Co) does not yield cube texture, rather the Bs texture transforms to $\{332\}\langle 113\rangle$ type texture. The intermediate composition Ni-40 co exhibits some amount of recrystallized cube texture along with some amount of twin of cube texture $\{122\}\langle 212\rangle$.

The formation of cube texture (shown in Figure 25) is not a desirable one so far as the material property is concerned. The formation of cube texture is a very fast process and just after the starting of recrystallization, the complete material

immediately becomes highly anisotropic. But the reason for the dominating characteristic of cube texture and its actual origin is still not known. The pole figure of 95% cold rolled pure copper and the recrystallized texture of the same have been juxtaposed in the Figure 26 from which it is clearly observed that in the cold deformed alloy, a high density of material is oriented within a range of orientations near $(211)[\bar{1}\bar{1}\bar{1}]$ 39° in the $\langle 100 \rangle$ - $\langle 111 \rangle$ boundary. In addition, substantial amount of material is also oriented near $(110)[\bar{1}\bar{1}\bar{2}]$ 55° to $(110)[00\bar{1}]$ 90° . One of the theories of recrystallization says that the nucleus of recrystallization texture remains in the cold rolled structure itself as small crystallites, and during the course of recrystallization they just grow by consuming the highly strained region. This is the strain induced boundary migration theory (Block Theory) which says that the nucleus of the cube texture should be present in the deformed structure itself, and it is observed that a small amount of material having orientations very near to the cube $(100)[001]$ is also present. Figure 26(b) shows that most of the material has cube orientation for fully recrystallized alloy. The twin related component of the cube texture also appeared, around $(221)[\bar{2}\bar{1}\bar{2}]$. In addition, small amounts of materials are also found having orientation spread over from $(531)[\bar{2}\bar{3}\bar{1}]$ 15° to $(553)[\bar{5}\bar{2}\bar{5}]$ 50° .

The formation of cube orientation and growth of cube oriented region have been carefully observed by the high voltage electron microscope, where a pure copper sample (95% deformed) was subjected to in situ annealing within the microscope. The process has been observed extremely fast. So it is concluded that the formation of cube texture is a highly favourable process both thermodynamically and kinetically.

Previously experiments already proved, that among all the criteria, the presence of a cube orientated region in the deformed matrix is the most important one. Cube grains start growing from cube orientated regions. The cube grains disproportionately larger than the grains of other orientation, because (1) early formation and (2) very high boundary migration rate.

The grain boundary migration gives rise to bulging out of grain boundary, which is a very important mechanism for recrystallization. During the recovery process, dislocation polygonisation process gives rise to strain free sub-grains, which in the later stage consumes the highly strained matrix in order to reduce the total free energy in the form of strain energy associated with dislocation and other crystal defects (Figure 27).

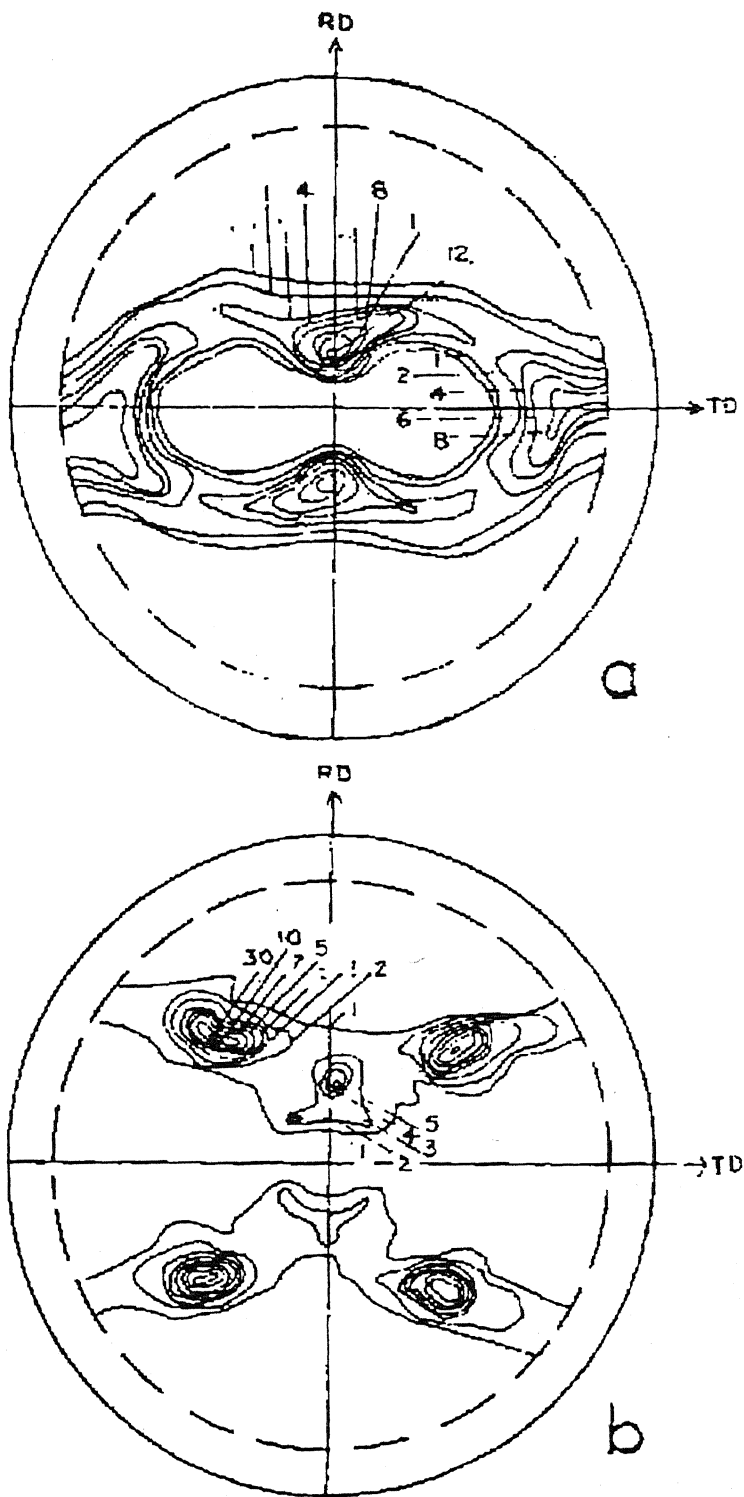


Figure 26. Pure Copper (a) Cu-type rolling texture
(b) Cube-type annealing texture.

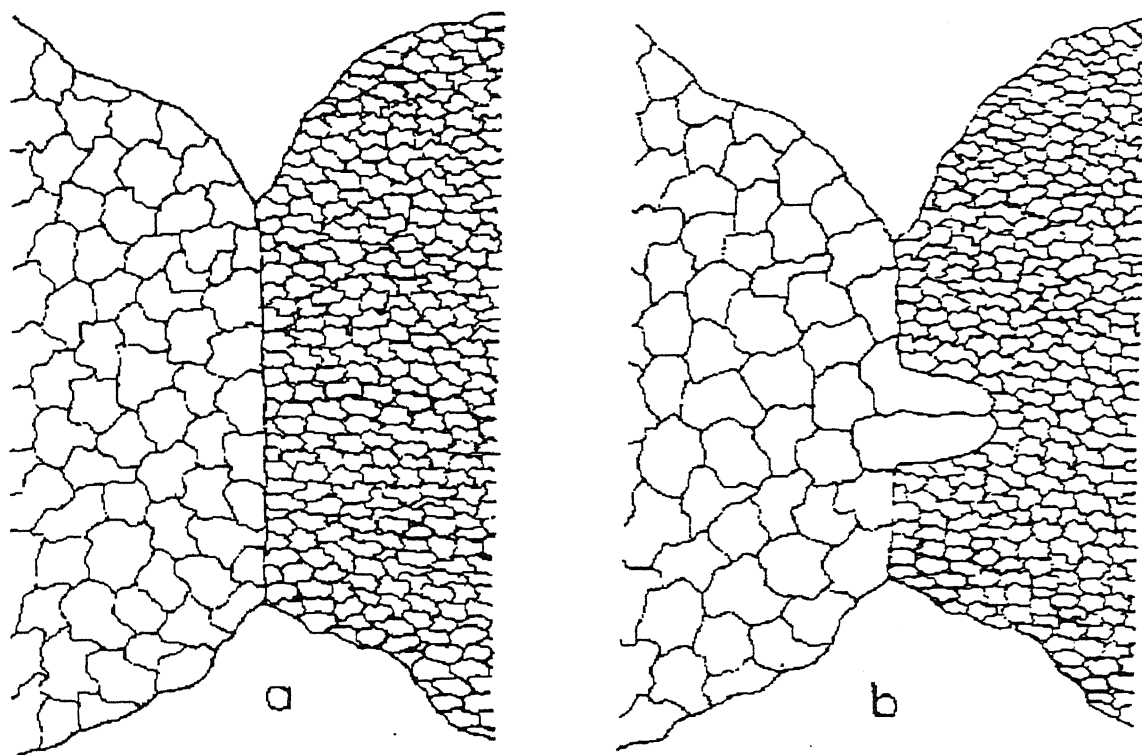


Figure 27. Grain Boundary Migration (a) Before Migration
(b) After Migration

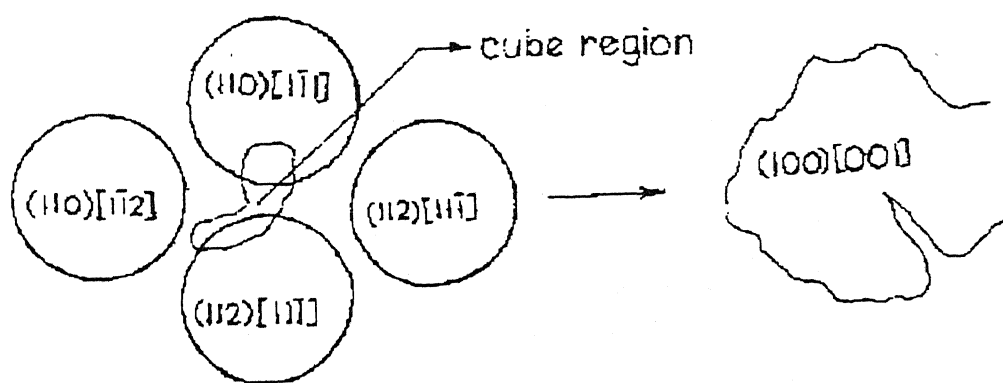


Figure 28. Growing of Cube Texture Region During Annealing

During the experiment carried out with pure copper, a well formed sub-grain having an orientation about 15° from the exact (001)[100] orientation has been observed to grow very fast consuming the neighbouring regions of other orientations (Figure 28).

During the growing of cube region, it is also observed that initially it avoids the regions where the dislocation density is locally high. But as time passes, dislocations from that concentrated region glide on some specific glide planes and ultimately form strain free cube oriented sub-grain structure.

The extraordinary sharpness of the cube texture has been explained on the basis of *oriented growth mechanism* of recrystallization. It is also observed that mobility of the grain boundary depends on the angle of the grain boundary. Low angle boundary shows lower mobility whereas higher angle grain boundaries exhibit higher mobility. In f.c.c. metals the fastest growing grains bear a particular orientation relationship to the deformed matrix. This is approximately 40° around a common $\langle 111 \rangle$ axis. For pure copper, this is around 30° . Also it maintains optimum angles with Cu, Bs textures. Grain growth is mainly a grain boundary migration and rotation process. Due to the optimum angle with the neighbouring orientations, grain rotation required for cube orientation is low, and probably this leads to the extremely low magnitude of activation energy for the growth of cube region, and the cube texture dominates over the other orientations. It has also been observed that a mobile high angle boundary can catalyze another nucleation event when it impinges on a suitable sub-grain, because essentially, sub-boundaries are the sites of nucleation.

2.8 Correlation of Literature Study with present investigation

The proposed work envisages study of the development of crystallographic texture in a Ni-40 Co & Ni-60 Co alloy during rolling deformation and subsequent recrystallization. The difference in the Stacking Fault Energies (SFE) of these two alloys is supposed to cause a difference in the mode of deformation during rolling. This could result in a difference in the deformation textures of the two alloys. Annealing of the deformed materials having different deformation textures is expected to result in totally different annealing textures. An attempt has been made to correlate textures with microstructure at different stages, so as to arrive at a definite conclusion regarding formation of textures in these two alloys during process.

CHAPTER 3

EXPERIMENTAL PROCEDURE

The Ni-Co binary system has been selected for the present investigation. The nominal compositions taken are

- (i) Ni-40 Co
- (ii) Ni-60 Co

The chemical compositions of the alloys (in weight percent) used in the present study are given in Table 1. Both nominal and detailed compositions of each alloy are given in that table. Two ingots — Ni-40Co and Ni-60 Co — were melted under vacuum. Segregation was avoided by magnetic stirring during melting. The ingots were cold-rolled 50% to a thickness of 10 mm and then homogenization annealed in vacuum at 1150°C for 24 hours. These were then again cold-rolled 50% and annealed at 1100°C for a period of 3 hours to yield the starting materials of most random texture and a grain-size of 0.1 mm.

3.1 Cold Rolling

The starting materials were cold-rolled by an amount of 95% reduction, using a laboratory rolling mill having 250 mm diameter rolls. Strips cut from the thick sheets were cold rolled. The direction of the strips were reversed end to end after each pass. In between any two successive passes, the strips were dipped into cold water bath to minimize any unwanted rise in temperature. The change in thickness after each pass was noted. In order that homogeneous deformation throughout the specimens might be achieved, the ratio of the length of contact with the rolls to specimen thickness was maintained at a value greater than unity[41]. In this way all the materials were rolled to 95% deformation and the same rolling schedule was followed for the two alloys.

3.2 Recrystallization Anneal

From the strips of the two alloys, a number of small pieces (about 4 mm x 6 mm) were cut out. These were subjected to heat treatment at 800°C for 15 minutes to 50 hours, in a Vertical Tube Furnace using argon atmosphere. After the heat treatment the samples were quenched in water.

3.3 Optical Microscopy

After heat treatment, the small pieces of all the materials were mounted using cold setting resin, for optical microscopy purpose. After mounting, these samples were subjected to conventional metallographic polishing and then etching. The etching reagent was prepared by mixing 50% (by volume) conc. HNO_3 with 50% (by volume) glacial acetic acid. Sometimes, a few drops of hydrofluoric acid were added for better and instant effect. To get the best effect, always freshly prepared etching reagent was used.

The etched samples were examined under Lieca Optical Microscope, and a number of photographs of each sample were taken.

3.4 Electron Microscopy

For this purpose, thin slices of size (20 x 20 mm²) cut from the rolling plane sections of each alloy, cold worked as well as annealed, were polished mechanically and then chemically and finally thinned down by electropolishing before examination under the Transmission Electron Microscope(TEM)[42].

A solution containing HNO_3 98% (by volume) and HF 2% (by volume) was used for chemical polishing. The chemically polished samples were further thinned down to the extent of electron transparency using twin-jet electro-polishing unit operating at 35 V. An electrolyte containing 12% (by volume) water, 70% (by volume) ethanol, 10% (by volume) ethylene mono butyl ether and 7.8 % (by volume) perchloric acid was used. All TEM work were carried out in a JEOL JEM-2000FX microscope operating at 160 kV.

3.5 Determination and Representation of Texture

For each sample (area $14 \times 24 \text{ mm}^2$) the texture was determined by plotting ordinary pole figures as well as Orientation Distribution Functions (ODF) which describe the crystalline orientation densities in a three-dimensional orientation space defined by the Euler angles ϕ_1, ϕ, ϕ_2 . For this purpose, from each texture sample four incomplete pole figures — $\{111\}$, $\{200\}$, and $\{311\}$ — were measured using $\text{CuK}\alpha$ radiation, in the range of azimuth = $5\text{-}85^\circ$. From these data the ODF was calculated after correction and symmetrization using the series expansion method[37,43,44] with a limit of $l_{\text{max}} = 22$. The resulting ODFs were approximated by model ODFs consisting of a superposition of isotropically scattering Gauss distributions[45-48]. This procedure made it possible to describe the rather complicated looking texture plots by only a few parameters, such as the volume fraction M_i and scattering widths ψ_i of the Gauss-type texture components g_i . The volume fraction M_i of a texture component can be written as[49]

$$M_i = \frac{96}{2\sqrt{\pi}} \cdot s_i \cdot \psi_i \cdot [1 - \exp(-\psi_i^2/4)] \quad (18)$$

where s_i denotes the maximum density (height) of the relevant texture component. The peak density f_i (g), directly observable in the true ODF, is no longer equal to s_i of the component I of the model. Moreover, in deriving M_i , since not only the height s_i but also the width ψ_i of the peaks are taken into account, the volume fractions of two components, characterized by similar f (g) values, may differ substantially. A random background component (BG) was included to take care of the additional weak components and irregular scattering. It has been shown[50] that the use of model ODFs also helps to correct the experimental ODFs of the so called ‘ghost error’ especially in orientation regions of low intensity. Another advantage of the Gauss model method is that by its use the multiplicity Z_i of different orientations is automatically taken care of[49].

All the ODFs mentioned in this thesis have been corrected in the manner stated above and, therefore, represent “true” (or “complete”) ODFs.

Table 1. Chemical composition of alloys (wt%).

	Alloy Nominal composition	Detailed composition (wt%)					
		Co	C	S	Si	Cu	Ni
A	Ni-40% Co	41.05	0.006	0.004	0.03	0.03	Bal.
B	Ni-60% Co	60.50	0.006	0.004	0.06	0.03	Bal.

पुरुषोत्तम काशीनाथ केलकर पुस्तकालय

भारतीय प्रौद्योगिकी संस्थान कानपुर

141867

अवधि क्र० A.....

CHAPTER 4

RESULTS

4.1 Optical Microscopy

To ascertain the microstructural features of the deformed and recrystallized samples, optical microscopy of polished and etched specimens were carried out. A series of optical micrographs of the samples which are 95% cold worked and recrystallized at 800°C for different lengths of time were taken using a Lieca Optical Microscope. A few typical optical micrographs of Ni-40 Co and Ni-60 Co alloys of 95% cold worked and recrystallized samples are shown in Figures 29 and 30.

The deformed microstructure for the Ni-40 Co alloy (Figure 29) consists of a large number of cells. Due to the limitations of the resolution of the microscope, it is not possible to describe the details of this microstructure. This will be done later in the subsection on TEM micrographs.

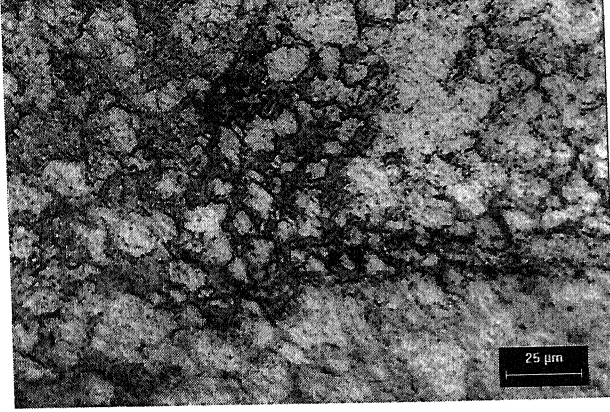
The annealed microstructures all indicate that the material has been recrystallized right from the earliest stage of annealing, namely after 15 minutes. The recrystallized grains grow as annealing time increases. Plenty of annealing twins are also seen within the recrystallized grains. These features are shown typically in Figure 29.

The optical microstructures of the deformed and annealed samples of Ni-60 Co alloy are quite similar to the corresponding microstructures of the Ni-40 Co alloy. Some typical microstructures of this alloy are shown in Figure 30.

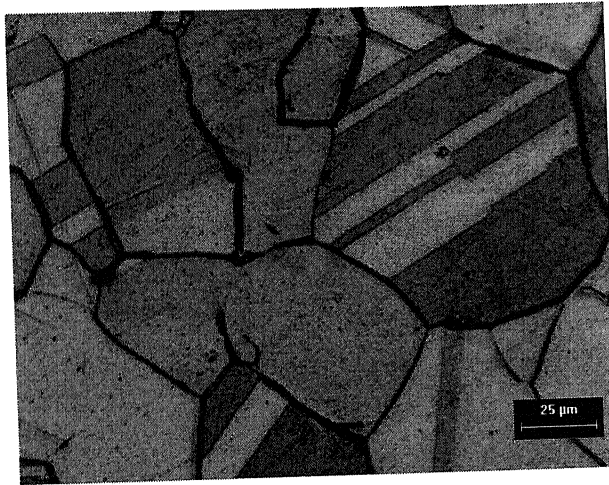
4.2 Electron Microstructures

4.2.1 Ni-40 Co Alloy

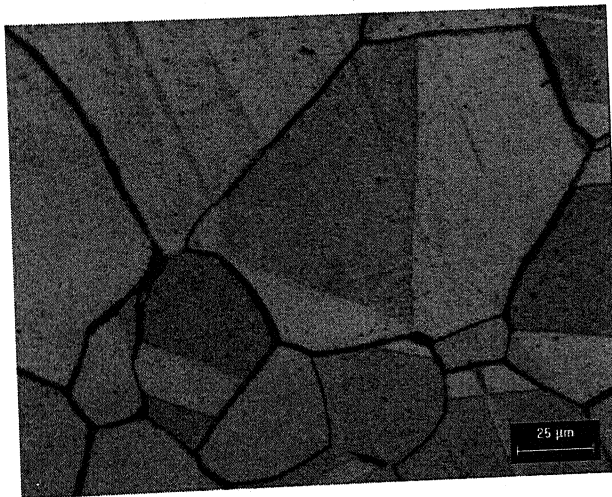
The TEM (Transmission Electron Microscopy) micrographs from the rolling plane sections of the 95% cold worked samples shows features typical of heavily deformed materials. Lots of cells have been seen and over and above the cells, some parallel twin like features has been seen along high dislocation density network of the



(a) 95% Cold Worked

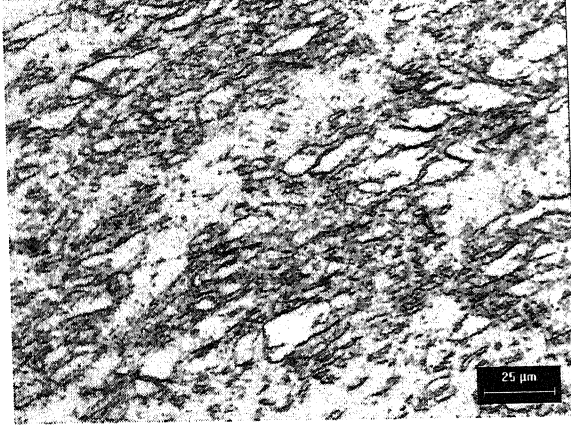


(b) Recrystallized at 800°C for 3 hours

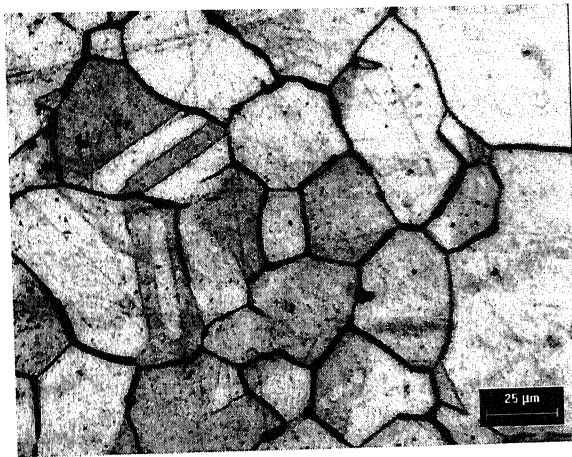


(c) Recrystallized at 800°C for 50 hours

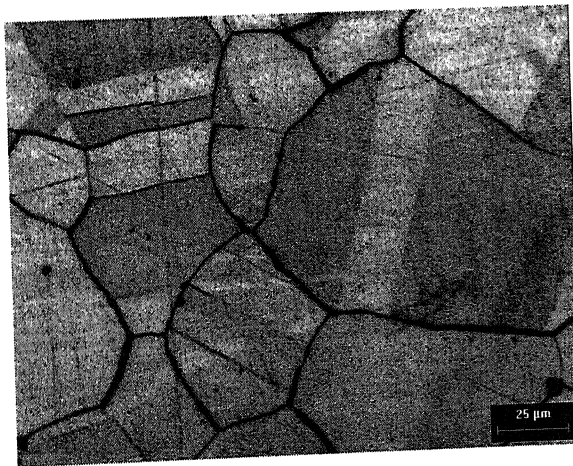
Figure 29. Optical Micrographs of Ni-40 Co alloy.



(a) 95% Cold Worked



(b) Recrystallized at 800°C for 3 hours



(c) Recrystallized at 800°C for 50 hour

Figure 30. Optical Micrographs of Ni-60 Co alloy.

deformed material. The selected Area Diffraction Pattern (SADP) of Figure 31(c) has been given in Figure 31(d).

After annealing the 95% cold worked Ni-40 Co alloy for 15 minutes at 800°C fully recrystallized grains have been formed. A typical micrograph has been shown in Figure 32(a) which also shows a large number of bend contours. SADPs taken from areas A, B, C, D and E of Figure 32(a) are shown in Figure 32(b) to (f). The foil planes at these locations have been identified in the figures. It is interesting to note the presence of a few twin spots in Figure 32(f).

Figure 33 shows a triple point which was observed in case of the 30 minutes annealed sample. Here the foil planes of all the three grains have been identified as $\{110\}$ type, however, they are rotated by a small angle in case of A and B and a large angle ($\sim 40^\circ$).

On further increasing the annealing time to 1 hour, lots of annealing twins have been found and this is typically presented in Figure 34(a). Twin spots however were not seen in the SADPs taken from areas A and B, whose matrix planes are $\{110\}$ and $\{310\}$ respectively. The SADP from area C shows that the foil plane here is $\{110\}$.

A high density of annealing twins were observed in the micrographs of the 3 hours annealed samples, shown typically in Figures 35(a) and (b). The SADP taken from the area A in Figure 35 (b) shows a $\{110\}$ pattern along with some weak twin spots. The foil plane at the location B also is $\{110\}$.

A typical triple point showing three recrystallized grains after 5 hours annealing is presented in Figure 36. Although the foil plane at all the three locations has been identified as $\{110\}$, the patterns from A and B are related by $\sim 50^\circ$ rotation, while there is an angle of $\sim 10^\circ$ between the SADPs of B and C.

The recrystallized grains observed after 10 hours annealing are shown typically in Figure 37 along with the SADPs from three different areas. The SADP of area C could be identified as due to a foil plane of $\{110\}$.

Big annealing twins present in the Ni-40 Co alloy after annealing for 20 hours, along with their SADPs are shown in Figure 38. After 50 hours of annealing also large annealing twins are observed in the big recrystallized grains, shown typically in Figure

39. The matrix area A and twin area B show basically $\{111\}$ spots. The SADP from area C could not be identified.

4.2.2 Ni-60 Co Alloy

The TEM micrographs of the 95 % cold rolled Ni-60 Co alloy (Figure 40(a) and (c)) show nearly complete Debye rings in their SADPs, indicating the presence of large number of crystallites of different orientations.

Figure 41 shows a typical area of this alloy after 15 minutes annealing, showing an annealing twin in area C.

After annealing for 30 minutes, large twins are observed in the microstructures of this alloy, shown typically in Figure 42. The foil plane at all the three locations, A, B and C shows that these are $\{110\}$ planes, rotated with respect to one another around the perpendicular to the foil plane.

A typical area after annealing for 1 hour is shown in Figure 43. The SADP from the area around location A shown $\{122\}$ spots plus some weak spots which may arise from the twin at B. The foil planes determined from area B, C and D as observed from their SADPs are $\{122\}$, $\{110\}$ and $\{123\}$ respectively.

The foil planes from most of the locations are of $\{110\}$ type is shown in Figures 44(a to e), taken from the 3 hours annealed sample.

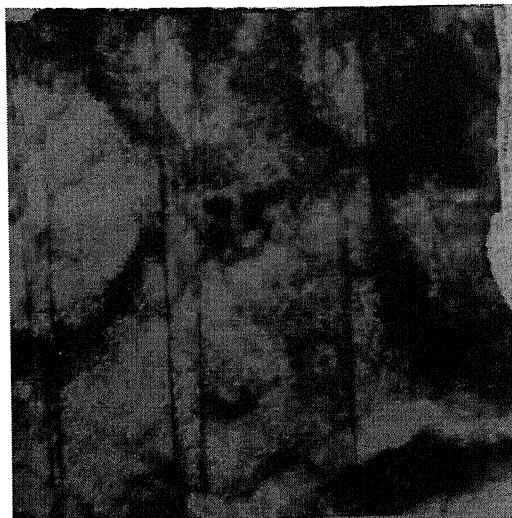
The foil planes such as $\{110\}$ and $\{122\}$ are quite common in the TEM micrograph of the 5 hours annealed sample also (Figure 45).

Three different locations with foil planes parallel to $\{110\}$ but rotated around $[110]$ have been observed from location A, B and C in the TEM micrograph of the 10 hours annealed sample (Figure 46).

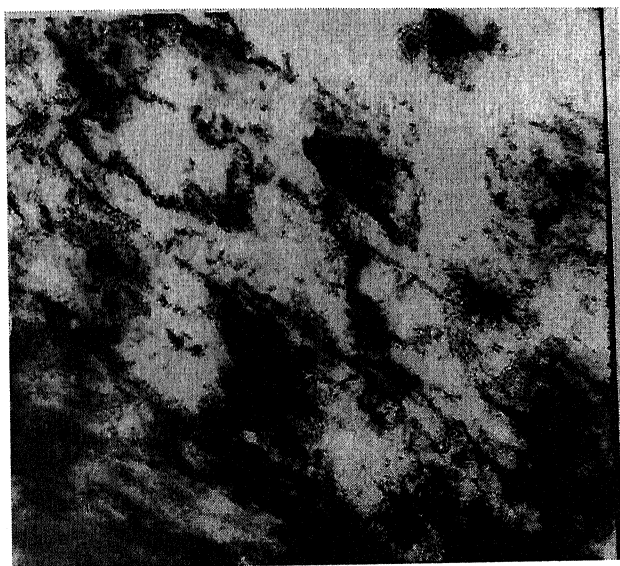
Large twins were also observed in case of the 20 hours annealed sample (Figure 47). The foil planes observed in both this case and for the 50 hours annealed sample (Figure 48) have again been found to be predominantly $\{110\}$ type planes.



(a) BF X 100k



(b) BF X 62.5k

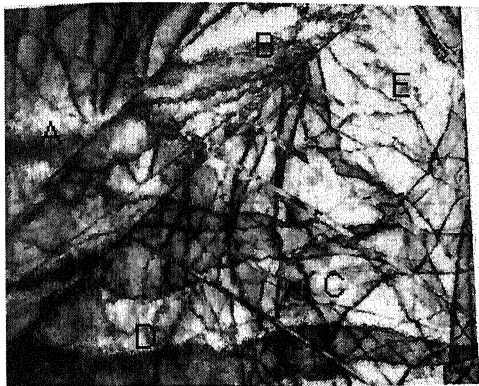


(c) BF X 30k



(d) SADP of figure (c)
Foil plane $\{112\}$

Figure 31. Microstructure of Ni-40 Co alloy (95 % Cold Worked).



(a) BF X 20k



(b) SADP of area 'A'
Foil plane {110}



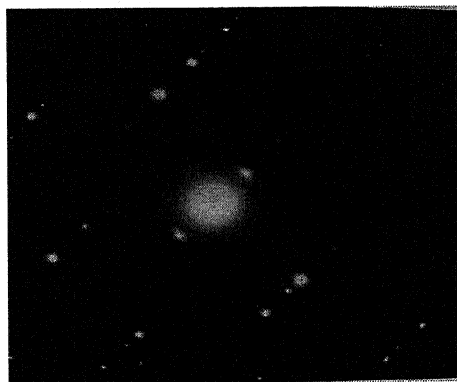
(c) SADP of area 'B'
Foil plane {110}



(d) SADP of area 'C'
Foil plane {310}

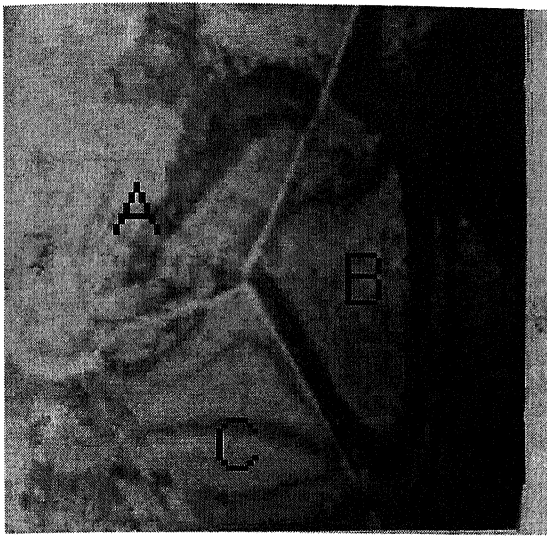


(e) SADP of area 'D'
Foil plane {110}

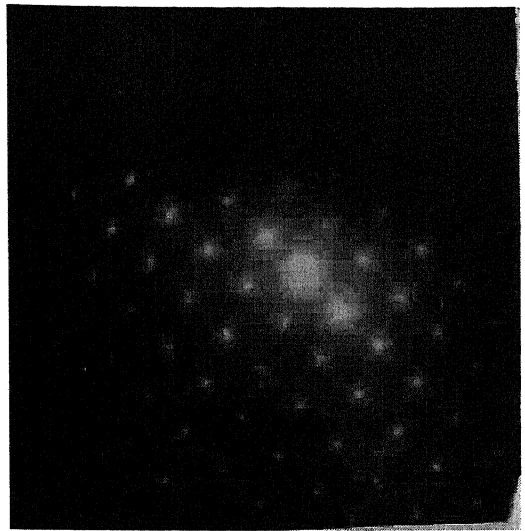


(f) SADP of area 'E'
Foil plane {110}

Figure 32. Microstructure of Ni-40 C0 alloy (annealed for 15 minutes at 800°C).



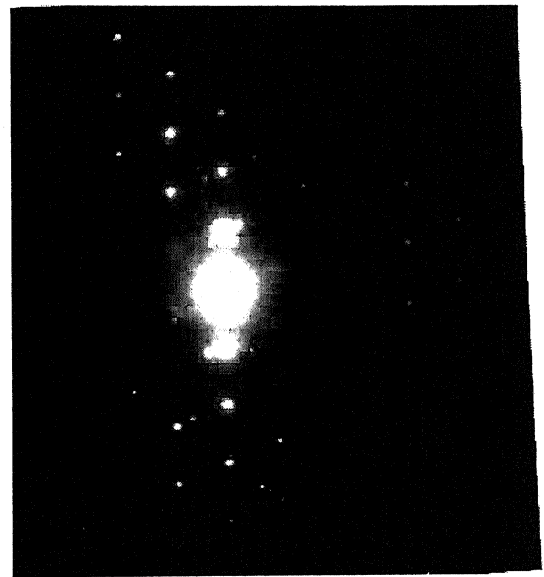
(a) BF X 15k



(b) SADP of area 'A'
Foil plane {110}

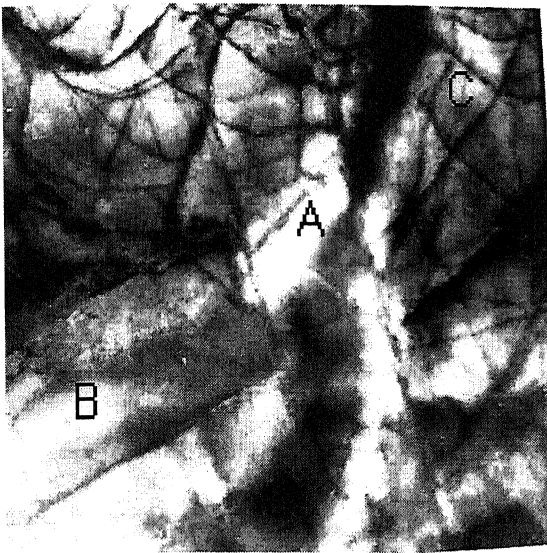


(c) SADP of area 'B'
Foil plane {110}

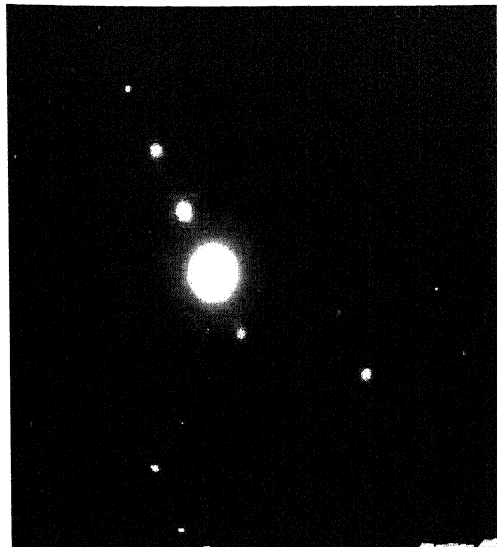


(d) SADP of area 'C'
Foil plane {110}

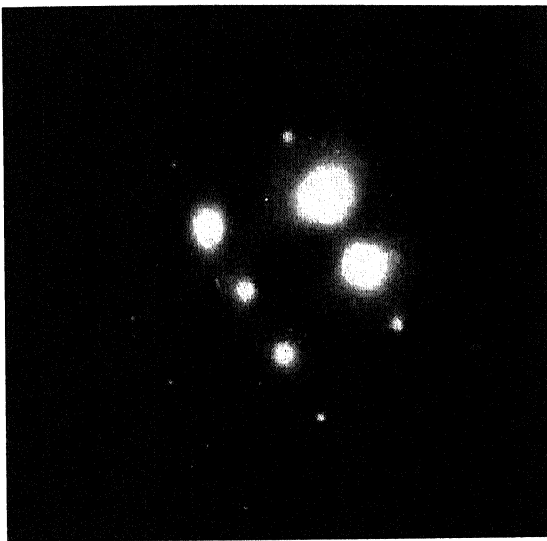
Figure 33. Microstructure of Ni-40 C0 alloy (annealed for 30 minutes at 800°C).



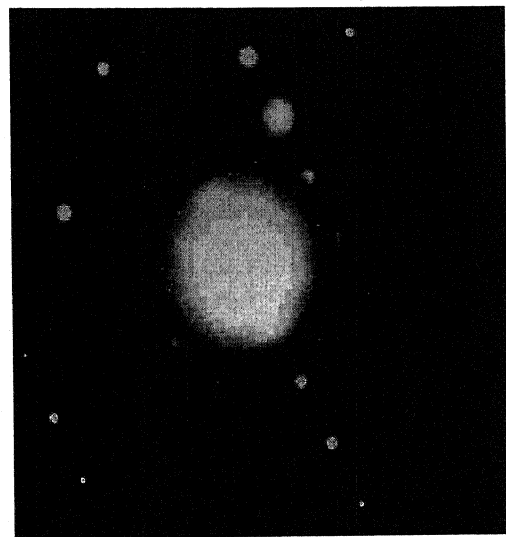
(a) BF X 25k



(b) SADP of area 'A'
Foil plane $\{110\}$

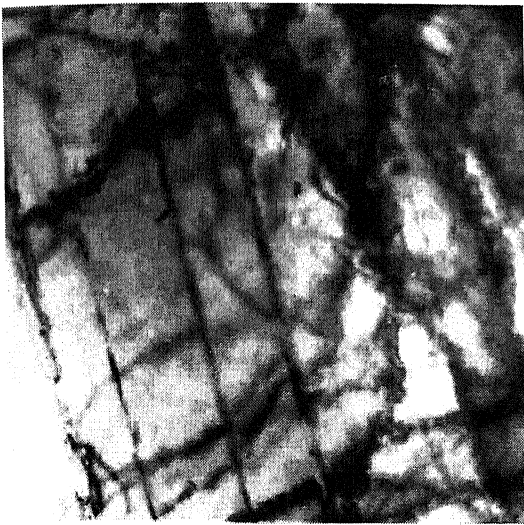


(c) SADP of area 'B'
Foil plane $\{310\}$

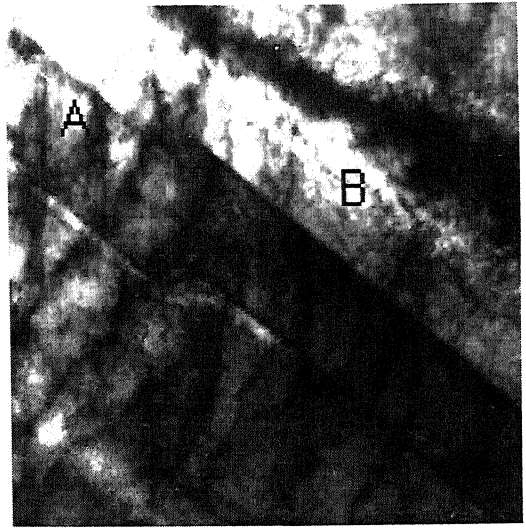


(d) SADP of area 'C'
Foil plane $\{310\}$

Figure 34. Microstructure of Ni-40 CO alloy (annealed for 1 hour at 800°C).



(a) BF X 75k



(b) BF X 25k

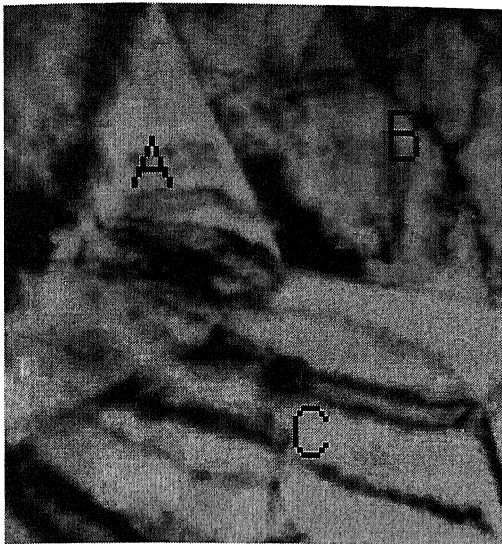


(c) SADP of area 'A'
Foil plane $\{110\}$

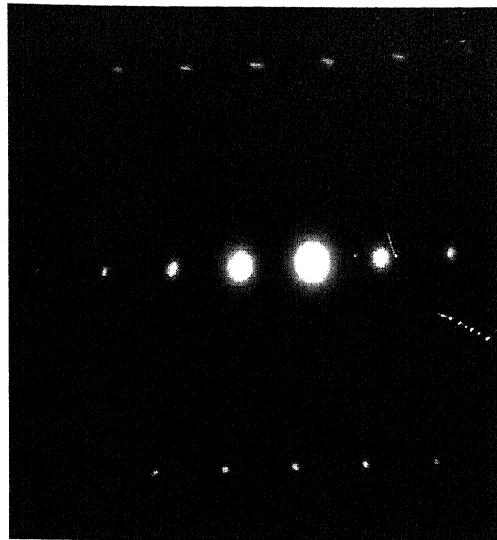


(d) SADP of area 'B'
Foil plane $\{110\}$

Figure 35. Microstructure of Ni-40 Co alloy (annealed for 3 hours at 800°C).



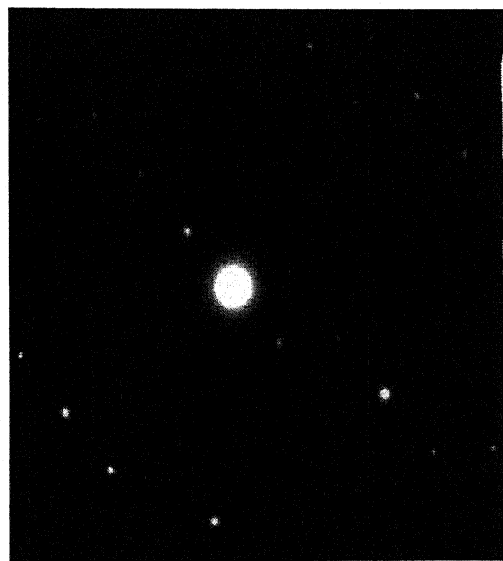
(a) BF X 25k



(b) SADP of area 'A'
Foil plane {110}

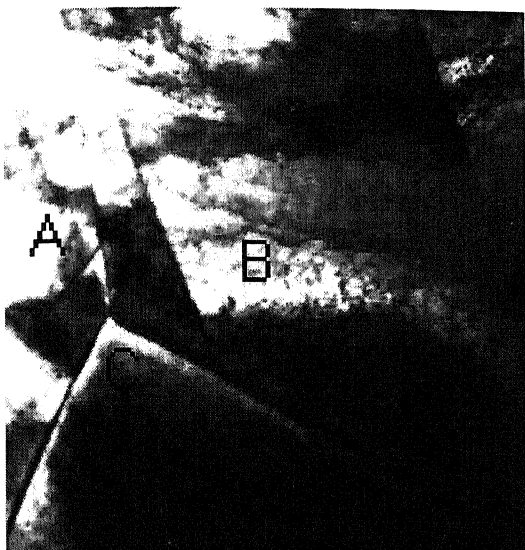


(c) SADP of area 'B'
Foil plane {110}



(d) SADP of area 'C'
Foil plane {110}

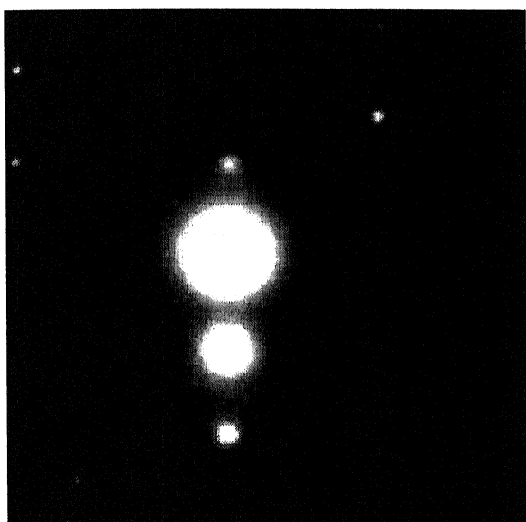
Figure 36. Microstructure of Ni-40 C0 alloy (annealed for 5 hours at 800°C).



(a) BF X 15k



(b) SADP of area 'A'

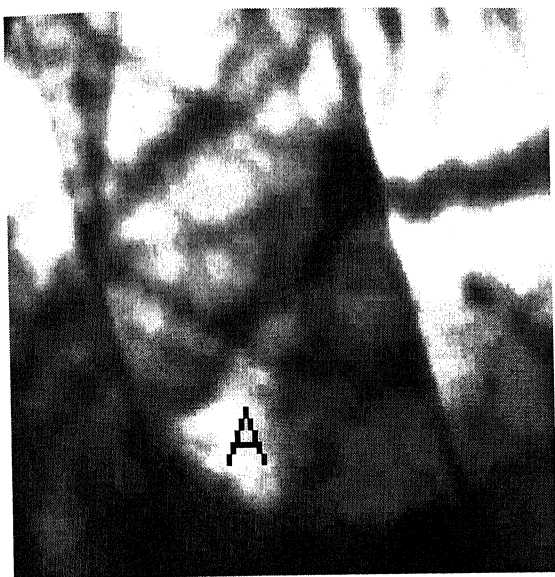


(c) SADP of area 'B'



(d) SADP of area 'C'
Foil plane {110}

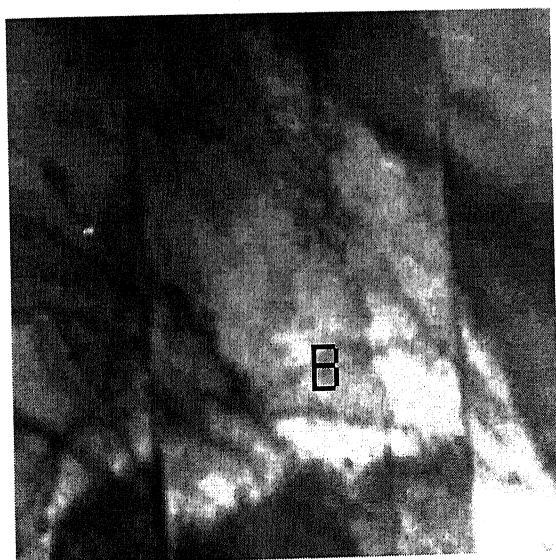
Figure 37. Microstructure of Ni-40 C0 alloy (annealed for 10 hours at 800°C).



(a) BF X 12.5k



(b) SADP of area 'A'

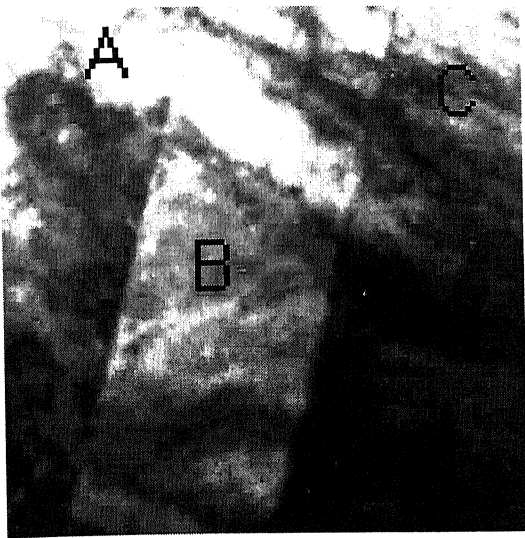


(c) BF X 20k



(d) SADP of area 'B'

Figure 38. Microstructure of Ni-40 C0 alloy (annealed for 20 hours at 800°C).



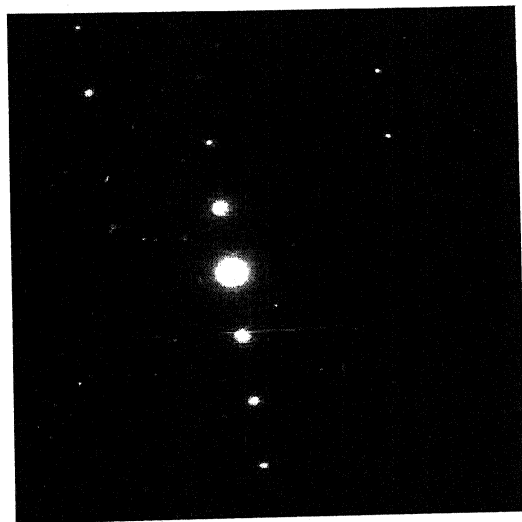
(a) BF X 20k



(b) SADP of area 'A'
Foil plane {111}

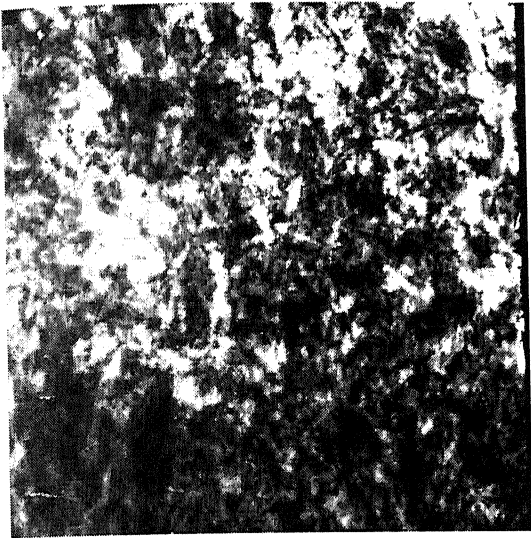


(c) SADP of area 'B'
Foil plane {111}

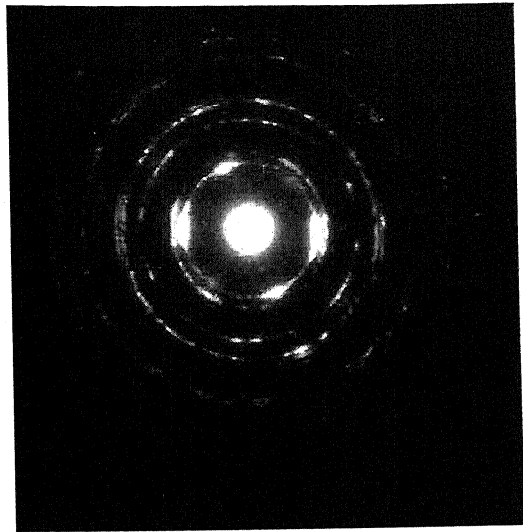


(d) SADP of area 'C'

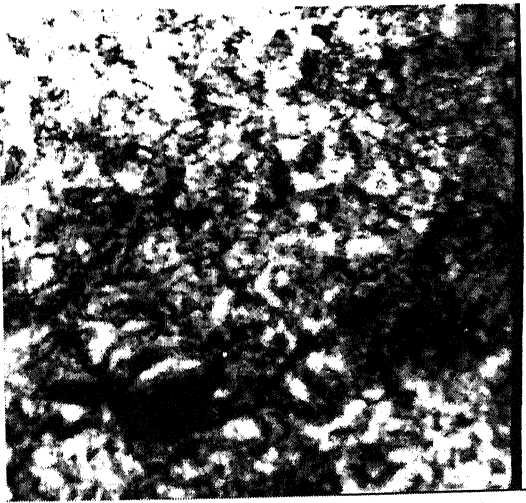
Figure 39. Microstructure of Ni-40 C0 alloy (annealed for 50 hours at 800°C).



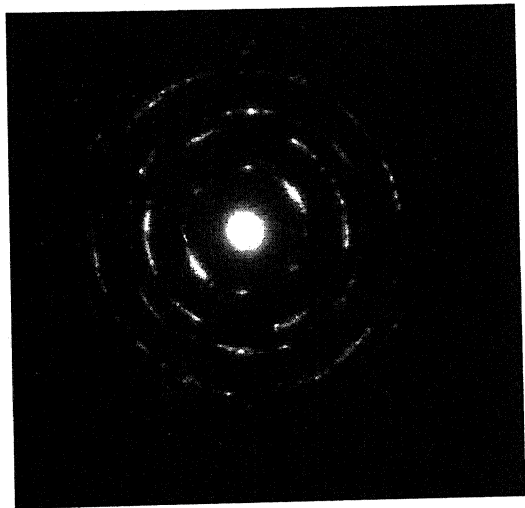
(a) BF X 37.5k



(b) SADP of figure (a)

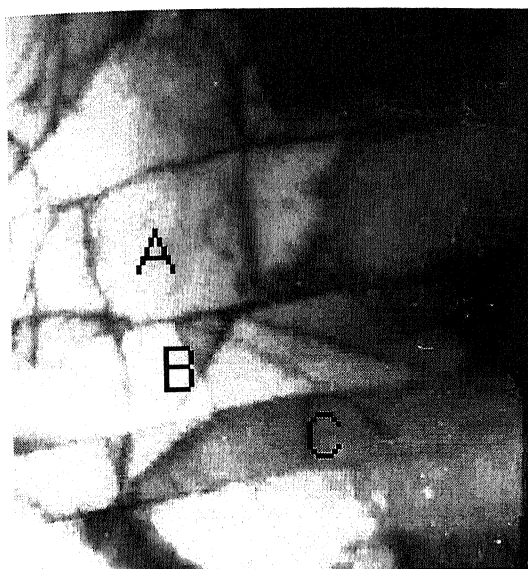


(c) BF X 62.5k



(d) SADP of figure (c)

Figure 40. Microstructure of Ni-60 Co alloy (95 % Cold Worked).



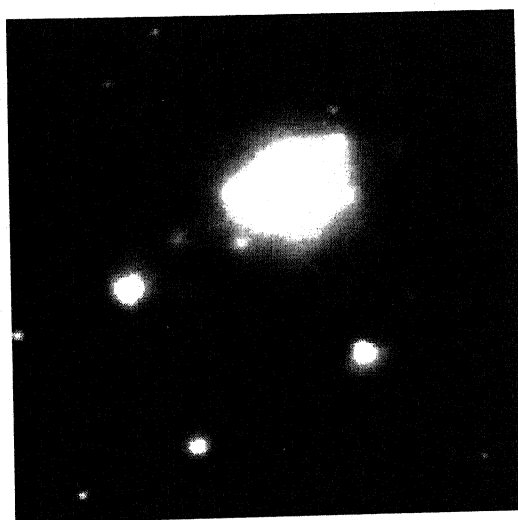
(a) BF X25k



(b) SADP of area 'A'

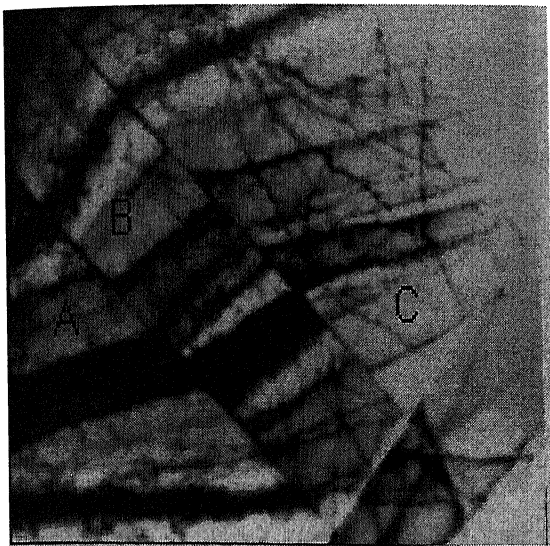


(c) SADP of area 'B'

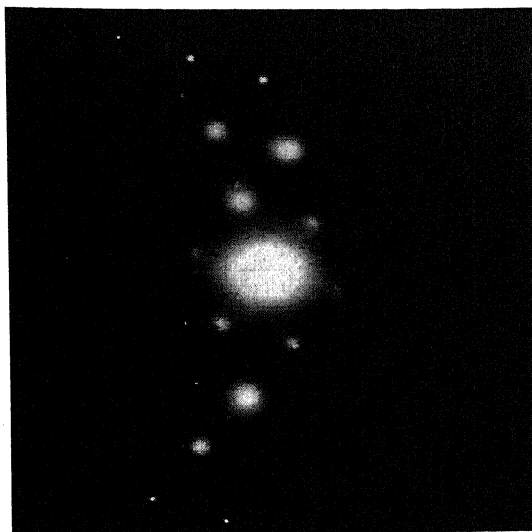


(d) SADP of area 'C'
Foil plane {110}

Figure 41. Microstructure of Ni-60 Co alloy (annealed for 15 minutes at 800°C).



(a) BF X 25k



(b) SADP of area 'A'
Foil plane {110}

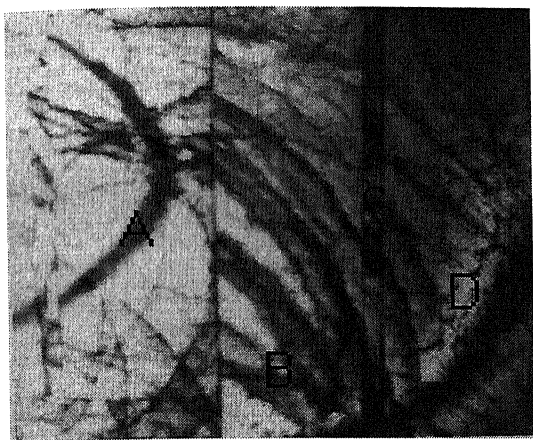


(c) SADP of area 'B'
Foil plane {110}



(d) SADP of area 'C'
Foil plane {110}

Figure 42. Microstructure of Ni-60 C0 alloy (annealed for 30 minutes at 800°C).



(a) BF X 10k



(b) SADP of area 'A'
Foil plane {122}



(c) SADP of area 'B'
Foil plane {122}

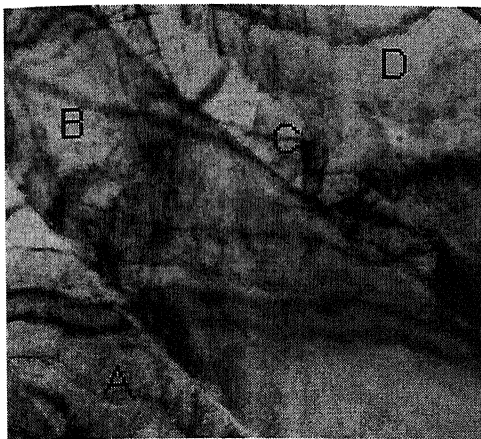


(d) SADP of area 'C'
Foil plane {110}



(e) SADP of area 'D'
Foil plane {123}

Figure 43. Microstructure of Ni-60 Co alloy (annealed for 1 hour at 800°C).



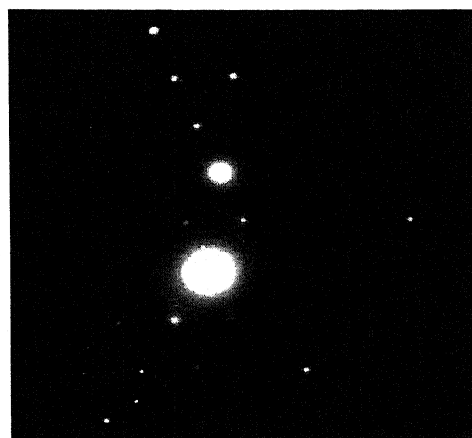
(a) BF X 20k



(b) SADP of area 'A'



(c) SADP of area 'B'
Foil plane {110}

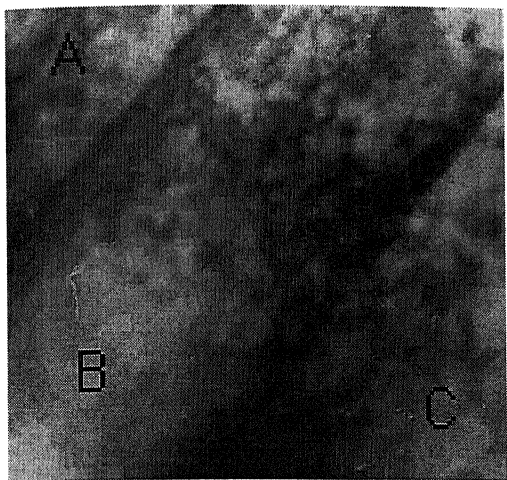


(d) SADP of area 'C'
Foil plane {110}



(e) SADP of area 'D'
Foil plane {110}

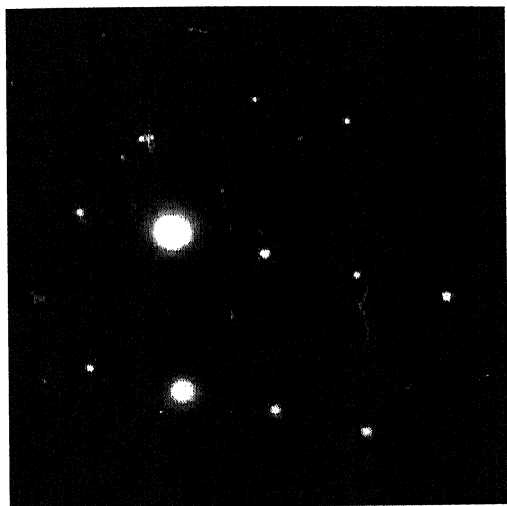
Figure 44. Microstructure of Ni-60 Co alloy (annealed for 3 hours at 800°C).



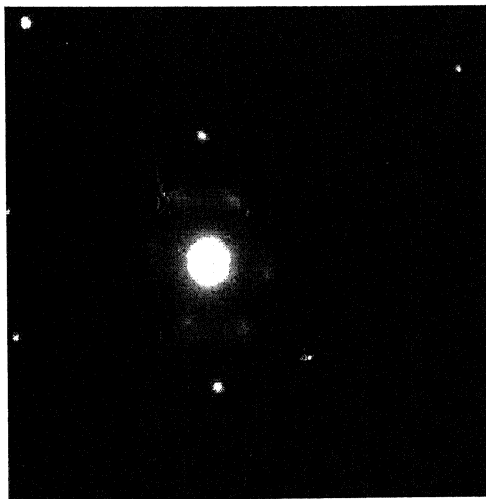
(a) BF X 37.5k



(b) SADP of area 'A'
Foil plane $\{110\}$

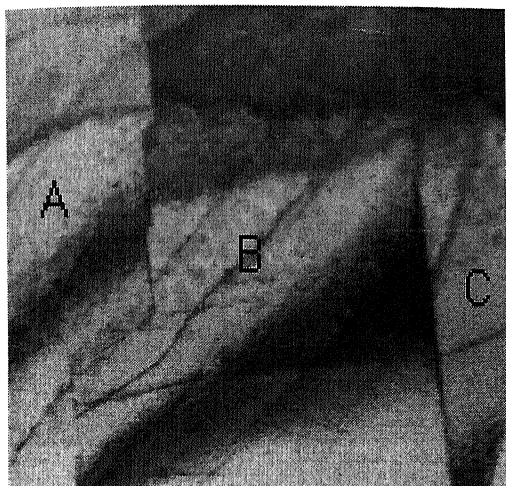


(c) SADP of area 'B'
Foil plane $\{122\}$

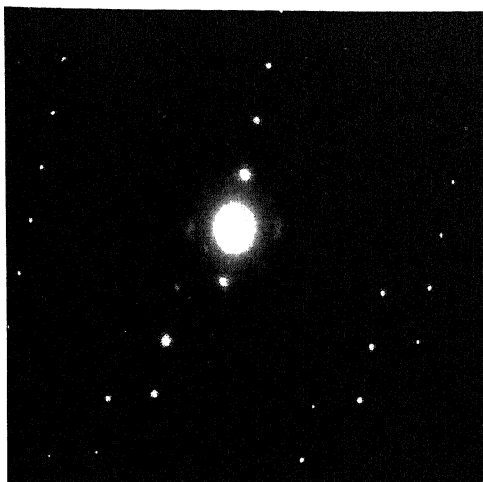


(d) SADP of area 'C'
Foil plane $\{110\}$

Figure 45. Microstructure of Ni-60 C0 alloy (annealed for 5 hours at 800°C).



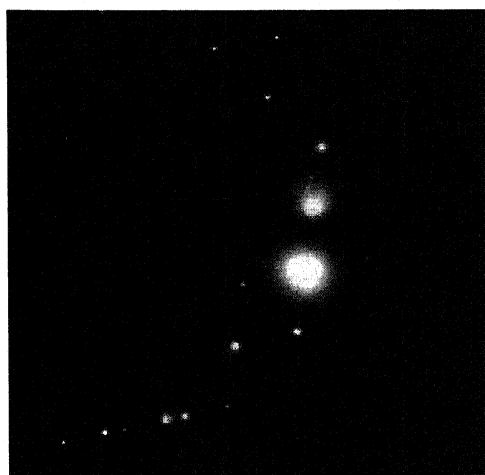
(a) BF X 30k



(b) SADP of area 'A'
Foil plane {110}

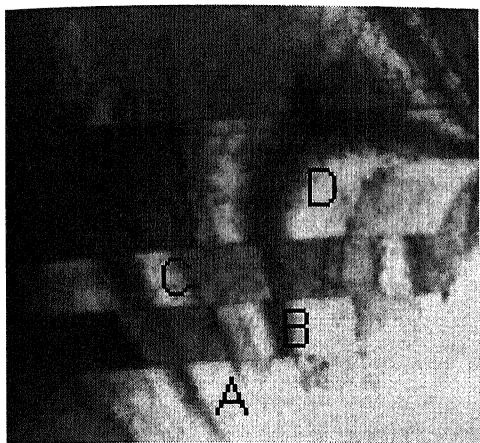


(c) SADP of area 'B'
Foil plane {110}



(d) SADP of area 'C'
Foil plane {110}

Figure 46. Microstructure of Ni-60 Co alloy (annealed for 10 hours at 800°C).



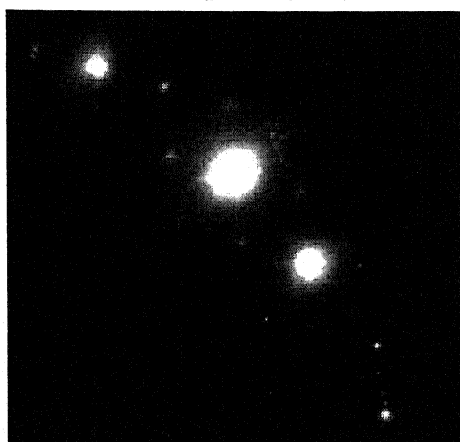
(a) BF X 10k



(b) SADP of area 'A'
Foil plane {110}



(c) SADP of area 'B'
Foil plane {110}

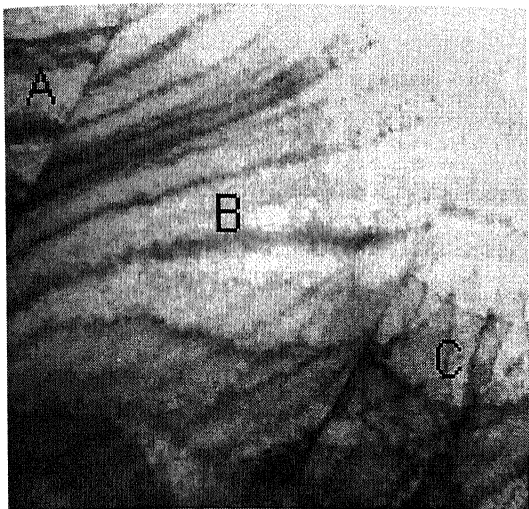


(d) SADP of area 'C'
Foil plane {110}



(e) SADP of area 'D'
Foil plane {110}

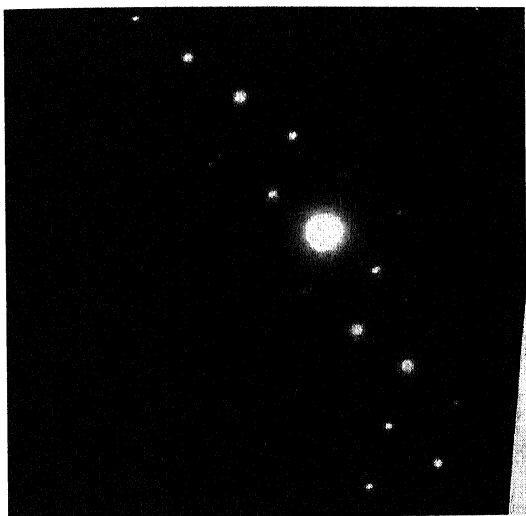
Figure 47. Microstructure of Ni-60 C0 alloy (annealed for 20 hours at 800°C).



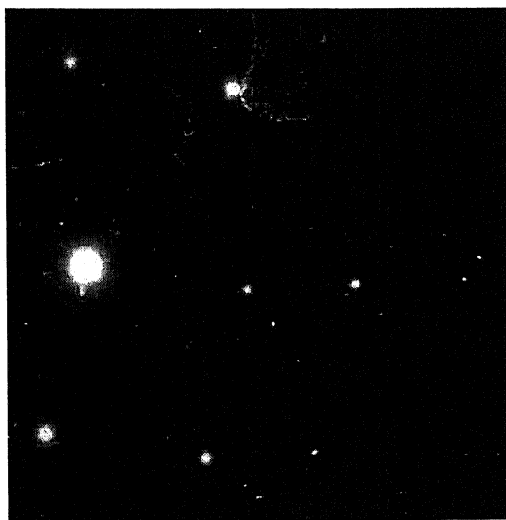
(a) BF X 12.5k



(b) SADP of area 'A'
Foil plane {110}



(c) SADP of area 'B'
Foil plane {110}



(d) SADP of area 'C'
Foil plane {110}

Figure 48. Microstructure of Ni-60 Co alloy (annealed for 50 hours at 800°C).

4.3 Crystallographic Texture

To determine the crystallographic textural changes of Ni-40 Co and Ni-60 Co alloys (95% cold worked and recrystallized at 800°C for various time durations), a detailed Orientation Distribution Function (ODF) analysis was carried out.

4.3.1 Ni-40 Co alloy

The ODF of the 95% cold rolled alloy is presented in Figure 49. The most predominant texture component here is the Bs, followed by some S, with very little Cu component. The volume fractions of the different components have been shown in Table 2.1.

The texture changes drastically after the cold worked material is subjected to the recrystallization anneal. The ODFs were measured at every stage of annealing. Some typical ODFs, after annealing for 15 minutes, 20 hours and 50 hours, are shown in Figures 50, 51 and 52. The locations of the important texture components and their volume fractions, as measured from the respective ODFs, are given in Table 2.2 to 2.7. The volume fraction, M_i , and pole density, $f(g)$, of the different texture components have been plotted against annealing time in Plots 1 and 2. It is clear from the volume fraction versus annealing time diagram, that the major component, after recrystallization of this alloy, is the nearly Rotated Cube(\sim RC) $\{258\}<121>$. The volume fraction of this component is quite large right from the earliest stage of annealing and maintains a high value of nearly 50% over the whole duration of annealing upto 50 hours.

The next two prominent components are the S $\{123\}<634>$, and Brass Recrystallized(Bs R) $\{326\}<232>$. As can be seen in Plot 1, the volume fraction versus annealing time plots for these two components show some kind of a mirror image relationship, in the sense that when the weighing of one component is large, that of the other component is small. Ultimately, after 50 hours annealing the volume fraction of the Bs R component far outweighs the volume fraction of the S component.

The Cube component $\{100\}<001>$, reaches a maximum volume fraction of $\sim 15\%$ after 3 hours annealing and then decreases and maintains a volume fraction of $\sim 10\%$ throughout the annealing process. The Goss component $\{011\}<100>$, is rather weak and

increases marginally, reaching a volume fraction of ~10% after 50 hours of annealing. Another weak component, $\{025\}\langle 100\rangle$, has been observed which is present in small amount after 15 minutes annealing and then vanishes completely after longer annealing periods. The Cu component $\{112\}\langle 111\rangle$, which was present to the tune of ~8% after 15 minutes annealing, decreased very rapidly, becoming zero after longer annealing period. Another component, $\{511\}\langle 171\rangle$, has a volume fraction of ~20% after 15 minutes annealing. It vanishes completely after 30 minutes of annealing and onwards.

4.3.2 Ni-60 C0 Alloy

The ODF of the 95% cold rolled alloy is presented in Figure 53. The most predominant texture components here are the Bs $\{011\}\langle 211\rangle$ and S $\{123\}\langle 634\rangle$ followed by some Bs/G $\{011\}\langle 511\rangle$ component and a little G $\{011\}\langle 100\rangle$. The volume fractions of the different components have been shown in Table 2.8.

ODFs were also measured for the annealed material. Some typical ODFs after annealing for 15 minutes, 20 hours and 50 hours have been shown in Figure 54, 55 and 56. The locations of the important texture components and their volume fractions with pole densities, as measured from the ODFs, are given in Table 2.9 to 2.14.

The volume fraction, M_i , and pole density, $f(g)$, of the different texture components have been plotted against annealing time in Plots 3 and 4. It is clear from the volume fraction versus annealing time diagram that the major texture components here are the Bs/G and Rotated Goss(RG) $\{110\}\langle 011\rangle$. Both these components are quite prominent right after the initial stage of annealing and they maintain their strengths during continued annealing, reaching a volume fraction of ~35% individually after prolonged annealing of 50 hours.

Two other prominent components are $\{415\}\langle 272\rangle$ and the Bs/S $\{168\}\langle 211\rangle$. Both of these components increases in volume fraction right from the early stage of annealing, reaching a maximum volume fraction of ~25% each and then decline rapidly as annealing progresses. The plots for Bs/G and the $\{415\}\langle 273\rangle$ seem to have a mirror image relationship between them. Similarly, the Rotated Goss and the Bs/S have a mirror image relationship between them. In addition to these, there are two minor components,

Recrystallized Brass(Bs R) $\{236\}\langle 385\rangle$ and G which maintain a rather low volume fraction throughout the annealing process.

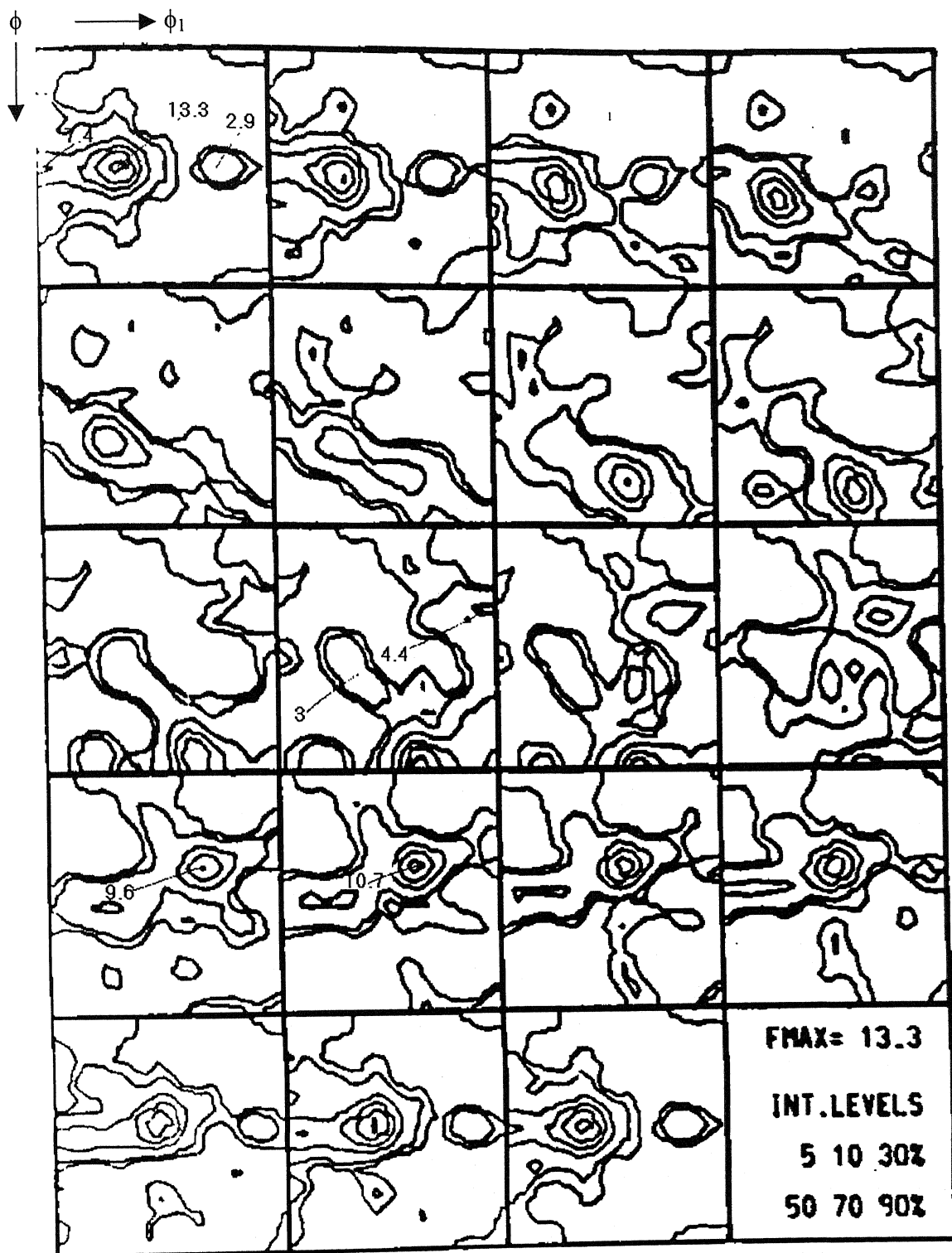


Figure 49. ODF of 95% cold rolled Ni-40 Co alloy.

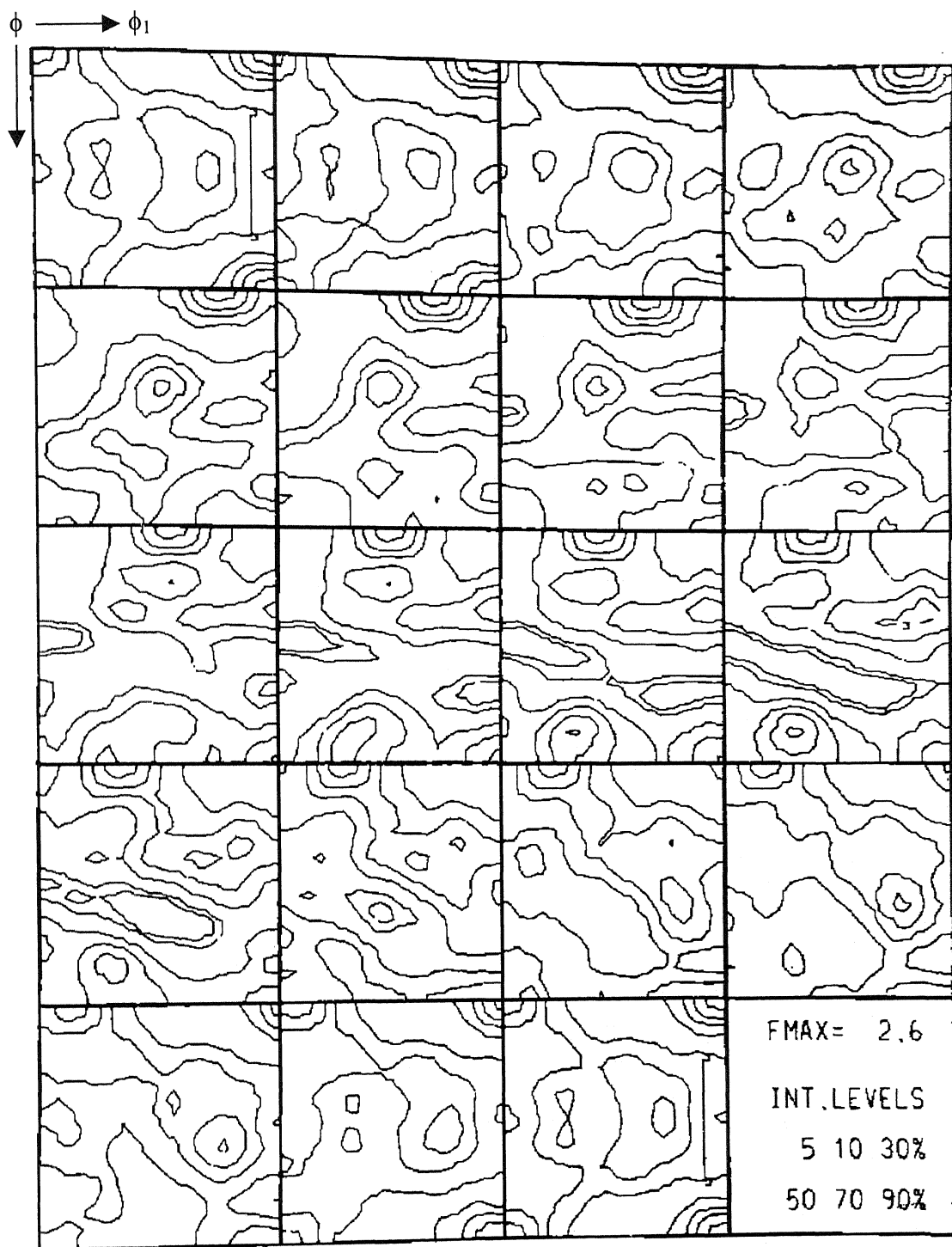


Figure 50. ODF of 15 minutes annealed Ni-40 Co alloy at 800°C.

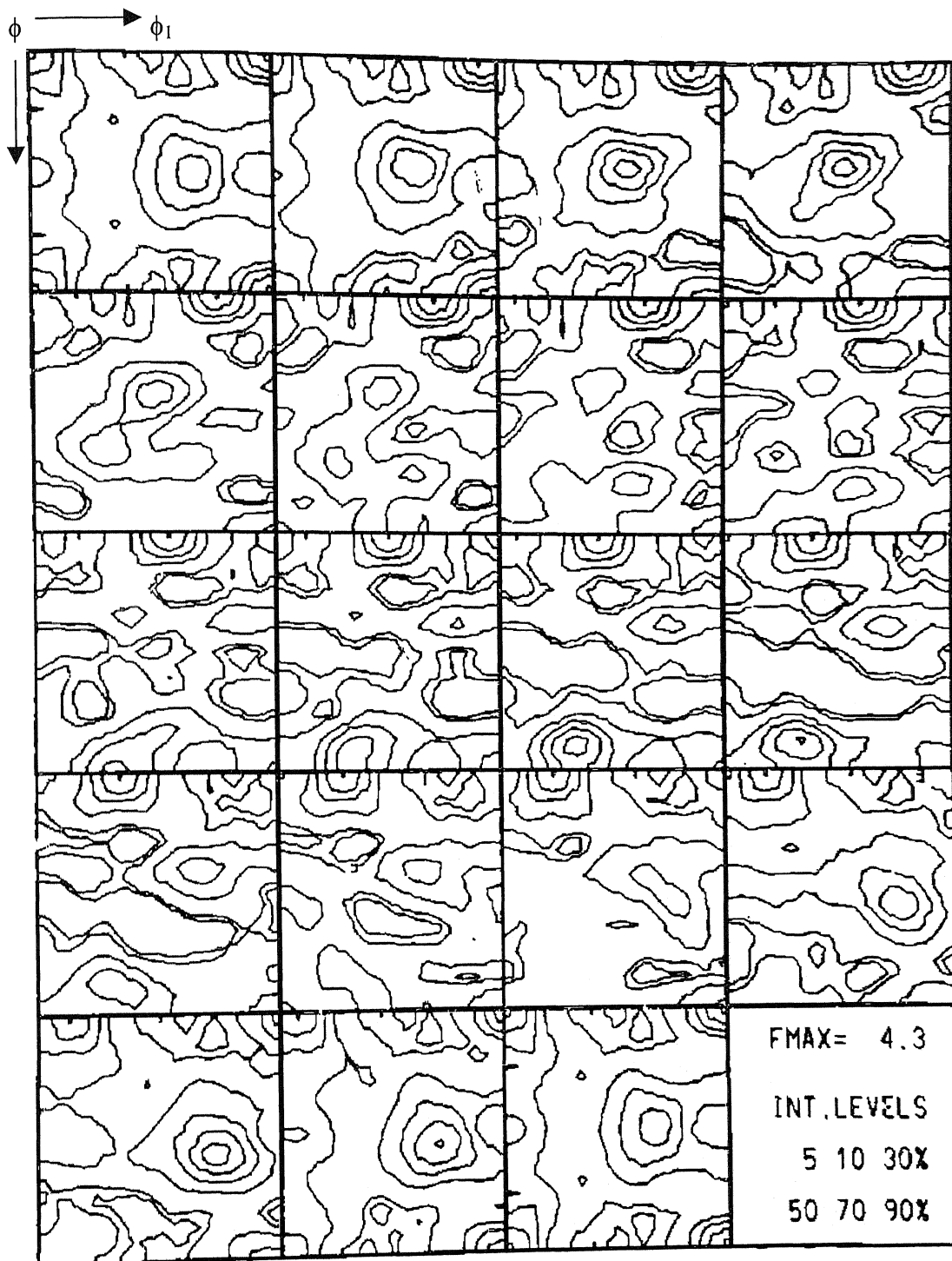


Figure 51. ODF of 20 hours annealed Ni-40 Co alloy at 800°C.

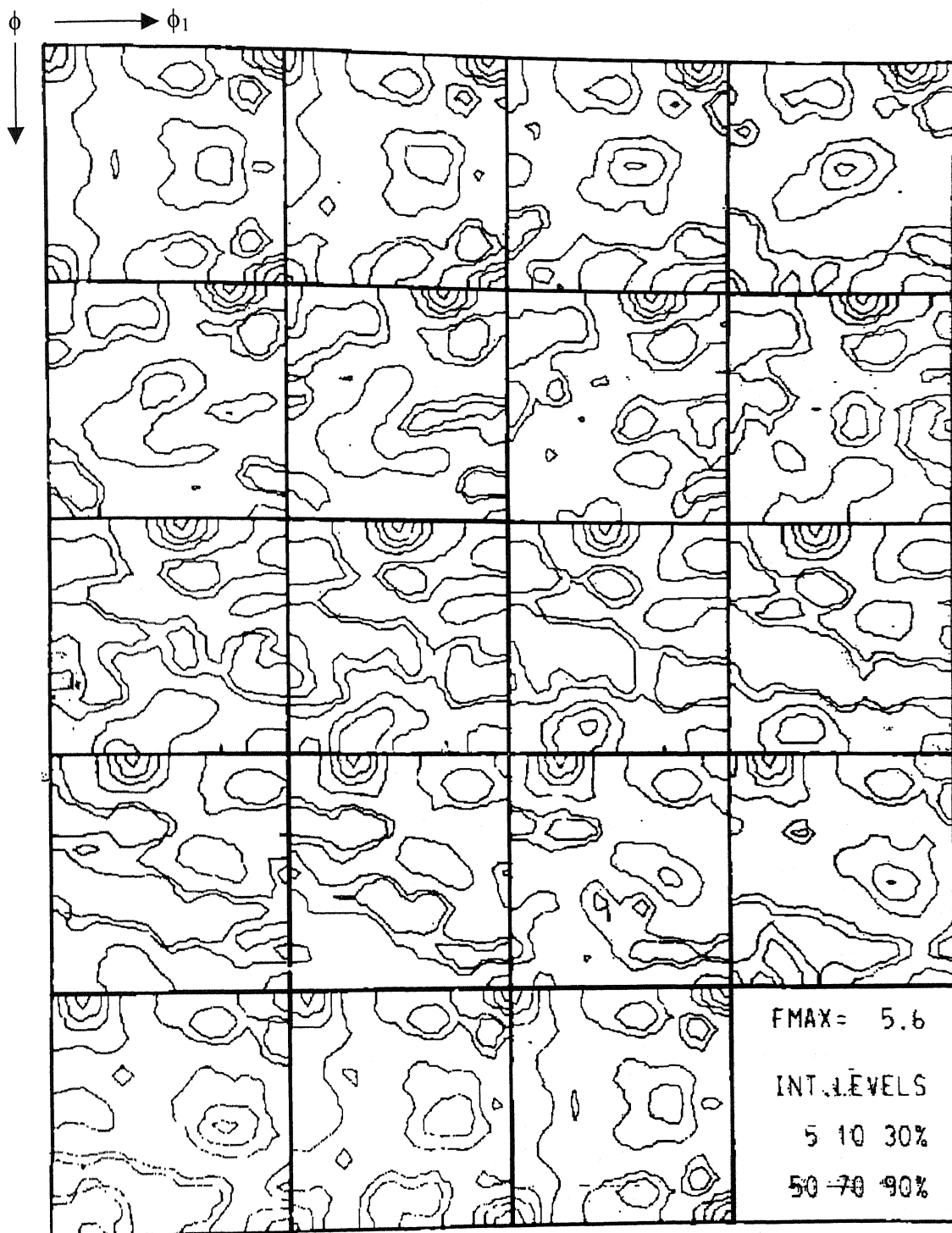


Figure 52. ODF of 50 hours annealed Ni-40 Co alloy at 800°C.

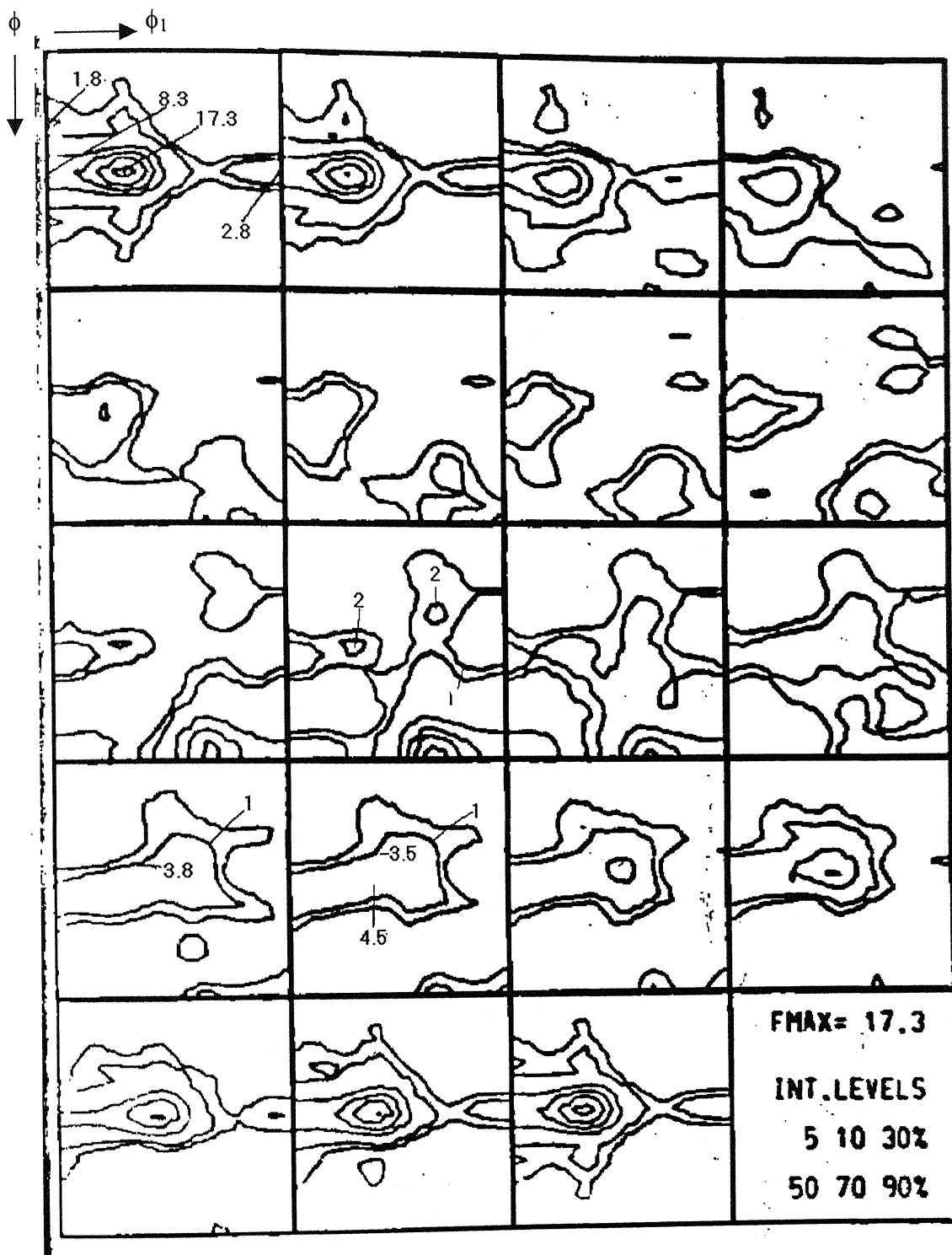


Figure 53. ODF of 95% cold rolled Ni-60 Co alloy.

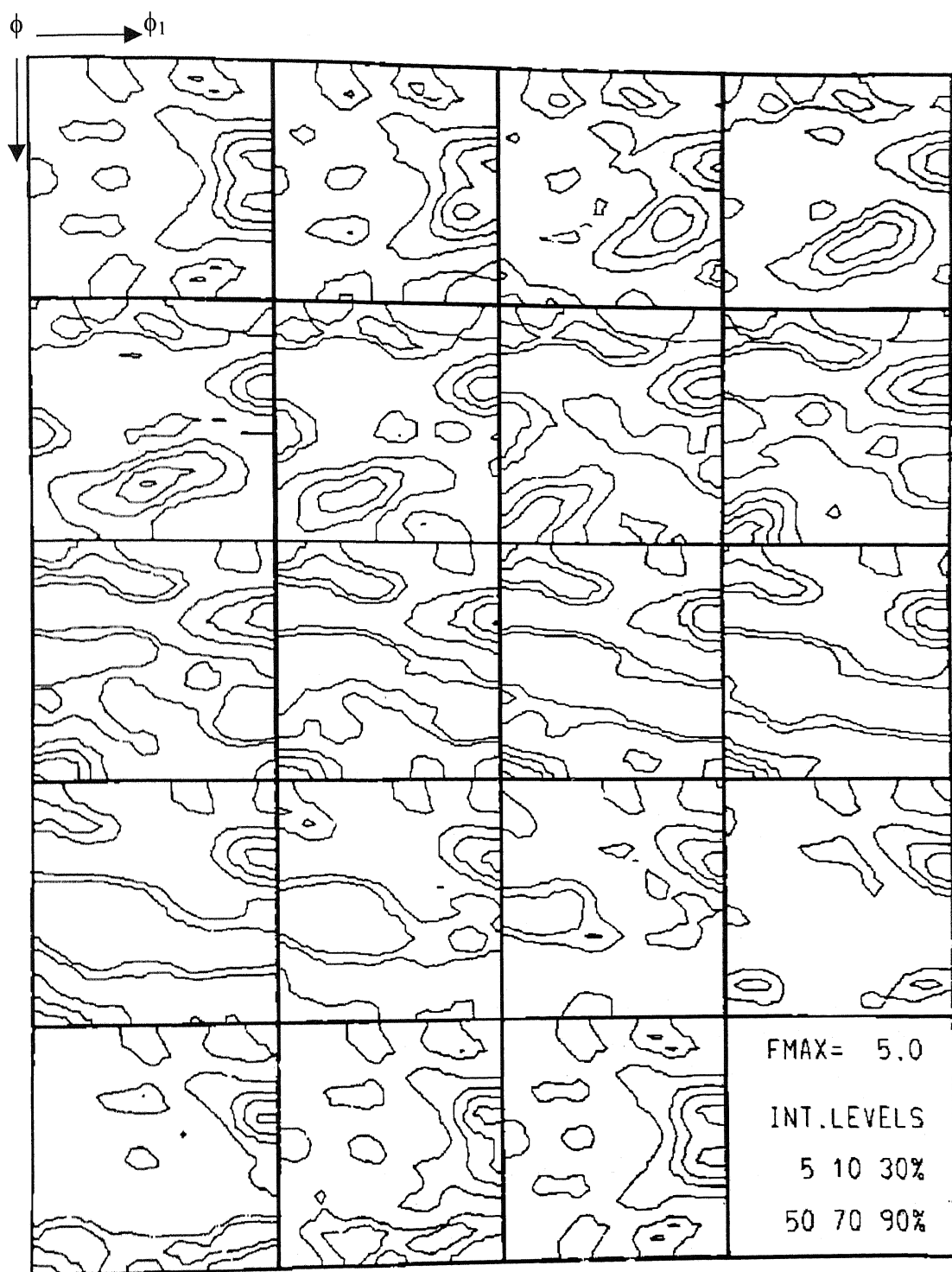


Figure 54. ODF of 15 minutes annealed Ni-60 Co alloy at 800°C.

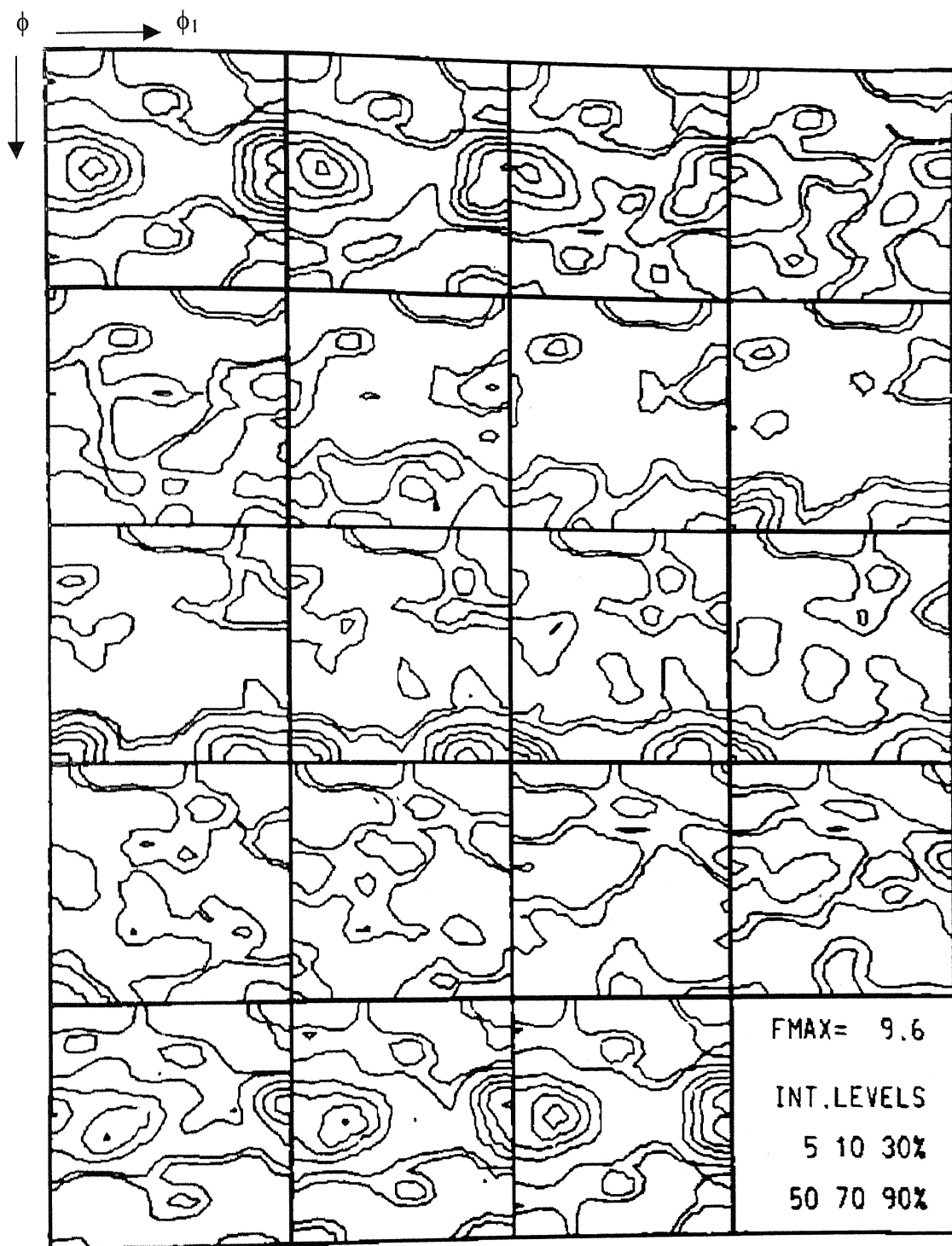


Figure 55. ODF of 20 hours annealed Ni-60 Co alloy at 800°C.

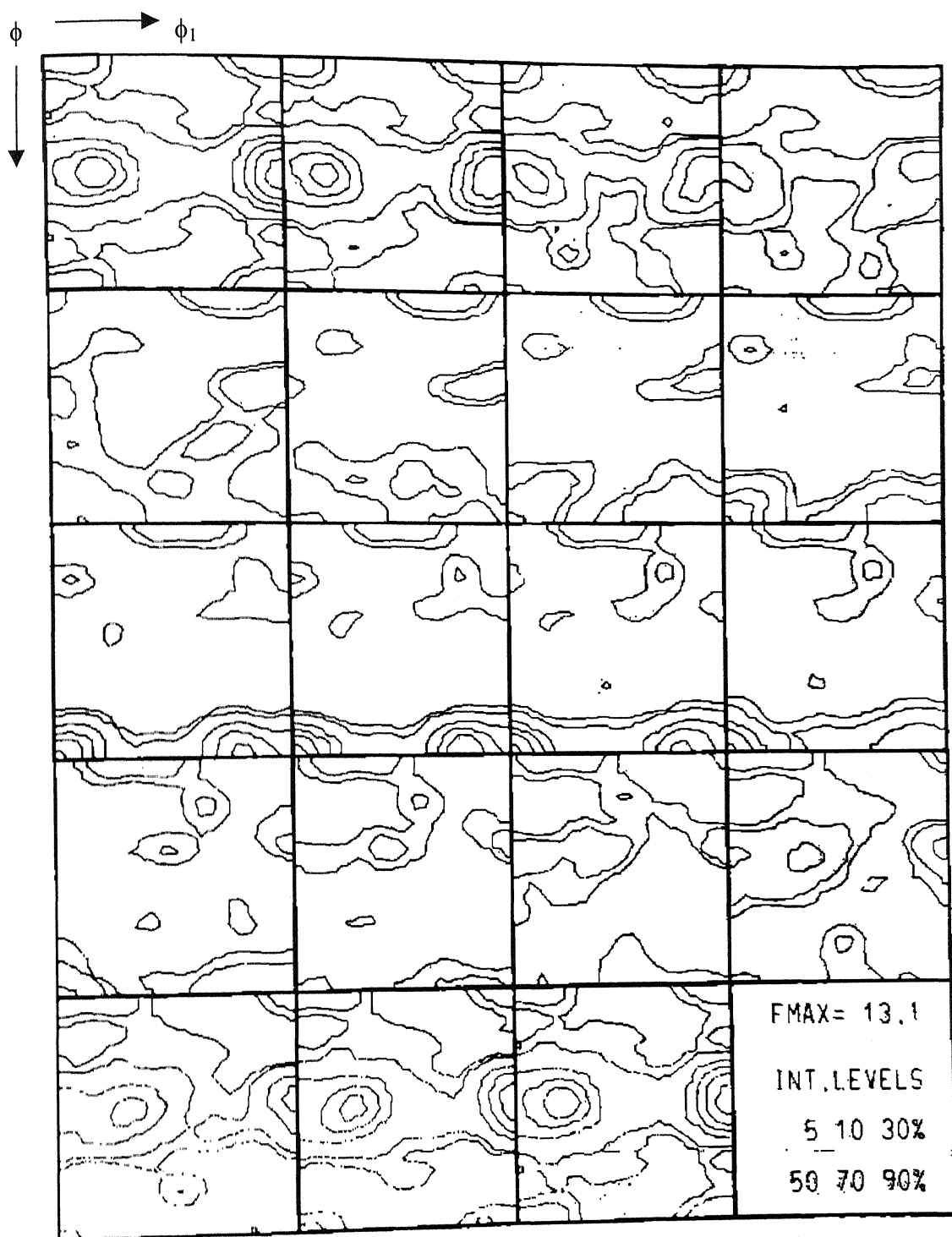


Figure 56. ODF of 50 hours annealed Ni-60 Co alloy at 800°C.

TABLE 2. Texture components and their weightage

Table 2.1. Ni-40 Co 95 % C.W.

S.No.	Component I.D.	Euler angles			$f(g)$	Vol. % ($M_i\%$)
		ϕ_1	ϕ	ϕ_2		
1	G {011}<100>	0	45	0	7.4	7.54
2	Bs {011}<511>	30.4	45	0	13.39	20.71
3	S <123><634>	55.3	35.2	65	10.7	26.68
4	{6 5 12}<634>	71.6	34.6	50	5.9	11.07
5	Bs/G {011}<511>	15	45	0	6.7	11.93
6	Twin Cu {552}<115>	10.1	45.6	75	4.9	2.68
7	Bs/S {168}<211>	45.1	38.4	75	11.4	14.50
8	Cu {112}<111>	90	30	45	4.4	3.78

Table 2.2. Ni-40 Co 95 % C.W. and annealed at 800°C for 15 minutes

S.No.	Component I.D.	Euler angles			$f(g)$	Vol. % (M_i %)
		ϕ_1	ϕ	ϕ_2		
1	C {100}<001>	0	0.5	0	2.57	3.17
2	nearly RC {258}<121>	48.2	39.1	16.9	2.46	37.94
3	Cu {112}<111>	90	30.1	45	2.15	7.79
4	S <123><634>	58.7	35.4	61.8	1.98	25.17
5	G {011}<100>	0	45	0	1.93	2.07
6	{511}<171>	20.8	19.4	83.5	1.72	20.49
7	{025}<100>	0.6	23.2	0	1.69	2.26

Table 2.3. Ni-40 Co 95 % C.W. and annealed at 800°C for 1 hour

S.No.	Component I.D.	Euler angles			$f(g)$	Vol. % (M_i %)
		ϕ_1	ϕ	ϕ_2		
1	nearly RC {258}<121>	49.9	37.4	13.2	4.61	52.91
2	C {100}<001>	0	0.5	0	3.78	7.69
3	G {011}<100>	0	45	0	2.5	3.94
4	S <123><634>	60.3	35.3	60	2.1	7.62
5	Bs R {326}<232>	70.3	33.3	50	2.3	16.65

Table 2.4. Ni-40 Co 95 % C.W. and annealed at 800°C for 3 hours

S.No.	Component I.D.	Euler angles			$f(g)$	Vol. % (M_i %)
		ϕ_1	ϕ	ϕ_2		
1	S <123><634>	55.5	36.8	61.1	2.51	24.30
2	G {011}<100>	0	45	0	2.05	2.38
3	C {100}<001>	0	0.6	0	4.58	15.84
4	nearly RC {258}<121>	49.9	39.2	13.2	4.25	43.72
5	Bs R {326}<232>	69.4	34.4	50	2.1	12.31

Table 2.5. Ni-40 Co 95 % C.W. and annealed at 800°C for 10 hours

S.No.	Component I.D.	Euler angles			$f(g)$	Vol. % (M_i %)
		ϕ_1	ϕ	ϕ_2		
1	G {011}<100>	4.8	45	0	2.3	5.90
2	C {100}<001>	0	0.6	0	3.3	9.95
3	nearly RC {258}<121>	51.7	39.1	12.4	4.12	51.07
4	S <123><634>	64.2	35.8	60.2	2.34	16.88
5	Bs R {326}<232>	75.5	33.2	45	2.18	14.49

Table 2.6. Ni-40 Co 95 % C.W. and annealed at 800°C for 20 hours

S.No.	Component I.D.	Euler angles			$f(g)$	Vol. % (M_i %)
		ϕ_1	ϕ	ϕ_2		
1	G {011}<100>	0	45	0	2.37	4.33
2	C {100}<001>	0	0.5	0	3.93	7.02
3	nearly RC {258}<121>	51.6	39.6	12.3	4.4	53.2
4	S <123><634>	62.9	35.3	57.4	2.71	20.57
5	Bs R {326}<232>	69.9	34.2	50	2.6	13.16

Table 2.7. Ni-40 Co 95 % C.W. and annealed at 800°C for 50 hours

S.No.	Component I.D.	Euler angles			$f(g)$	Vol. % (M_i %)
		ϕ_1	ϕ	ϕ_2		
1	C {100}<001>	0	0.7	0	5.62	11
2	nearly RC {258}<121>	47.2	40.4	13.5	4.3	48.48
3	S <123><634>	60.9	38.2	59	2.7	6.46
4	Bs R {326}<232>	70.7	34.3	45	2.34	23.03
5	G {011}<100>	0	45	0	2.6	9.77

Table 2.8. Ni-60 Co 95 % C.W.

S.No.	Component I.D.	Euler angles			$f(g)$	Vol. % (M_i %)
		ϕ_1	ϕ	ϕ_2		
1	Bs {011}<211>	29.6	45	0	17.34	29.88
2	G {011}<100>	0	45	0	8.3	5.10
3	RC {233}<311>	20.9	49.5	59.7	4.48	5.73
4	S {123}<634>	50.3	40.8	65	4.58	42.53
5	Bs/G {011}<511>	14.6	45	0	10.7	16.51

Table 2.9. Ni-60 Co 95 % C.W. and annealed at 800°C for 15 minutes

S.No.	Component I.D.	Euler angles			$f(g)$	Vol. % (M _i %)
		ϕ_1	ϕ	ϕ_2		
1	G {011}<100>	0	45	0	1.94	2.15
2	{013}<123>	56.1	21.1	0	1.95	32.02
3	Cu {112}<111>	90	28.6	45	4.63	22.76
4	RG {110}<011>	90	35.8	0	4.9	36.66
5	Bs {011}<211>	30	45	0	1.7	5.42

Table 2.10. Ni-60 Co 95 % C.W. and annealed at 800°C for 1 hour

S.No.	Component I.D.	Euler angles			$f(g)$	Vol. % (M _i %)
		ϕ_1	ϕ	ϕ_2		
1	Bs/G {011}<511>	19.2	45	0.2	7.41	28.75
2	RG {110}<011>	90	39.9	0	13.51	47.07
3	Bs/S {168}<211>	54.1	38.8	10	2.2	4.55
4	{415}<273>	33.6	41.6	75	4.2	2.07
5	BsR {236}<385>	81.2	33.7	30	4.7	17.90

Table 2.11. Ni-60 Co 95 % C.W. and annealed at 800°C for 3 hours

S.No.	Component I.D.	Euler angles			$f(g)$	Vol. % (M_i %)
		ϕ_1	ϕ	ϕ_2		
1	Bs/G {011}<511>	15.5	45	0.1	7.39	37.40
2	RG {110}<011>	90	39.7	0	11.4	43.07
3	Bs/S {168}<211>	49.4	38.1	10	2	3.59
4	{415}<273>	34.5	41.8	75	3.9	2.69
5	BsR {236}<385>	81.3	34	30	3.3	13.20

Table 2.12. Ni-60 Co 95 % C.W. and annealed at 800°C for 10 hours

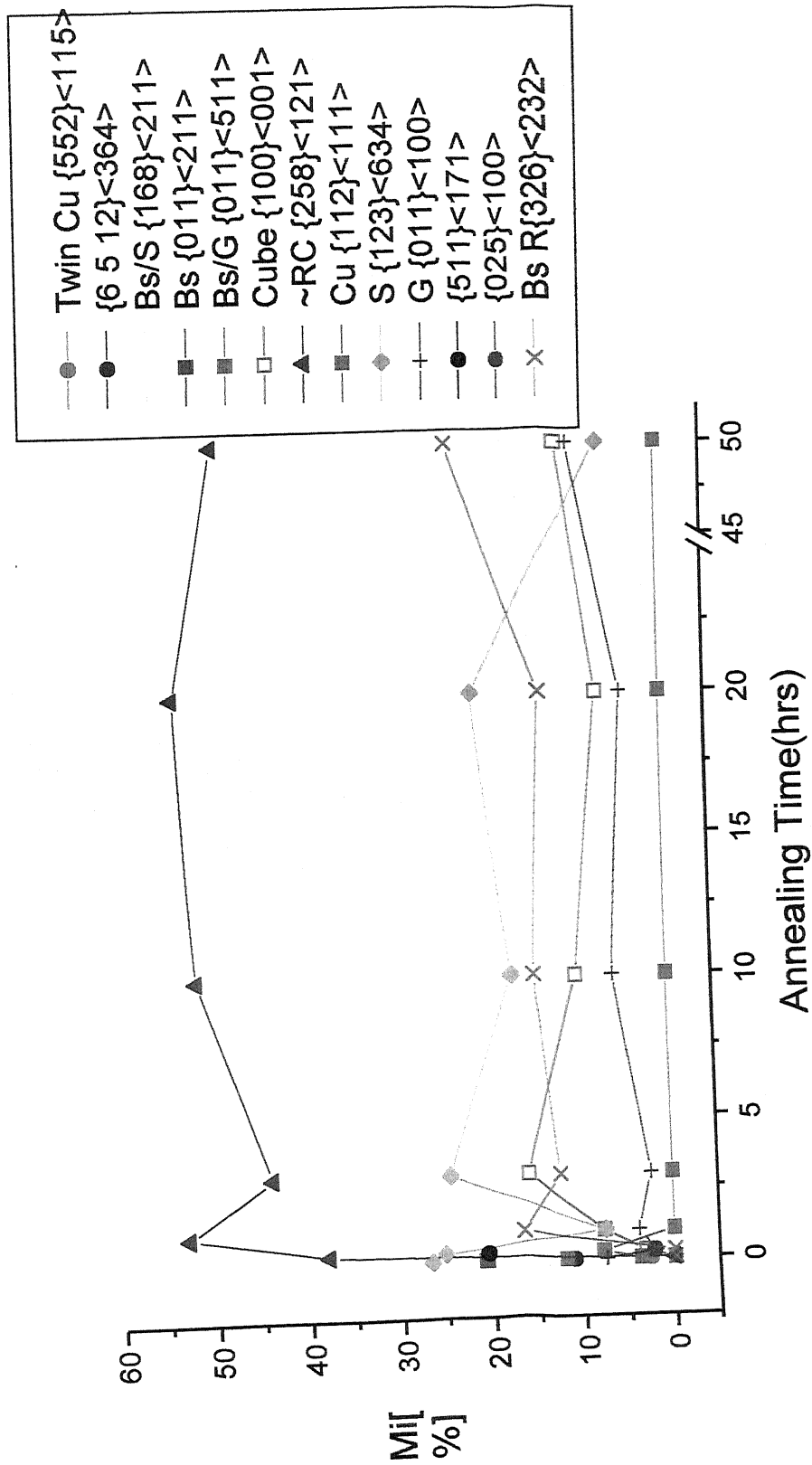
S.No.	Component I.D.	Euler angles			$f(g)$	Vol. % (M_i %)
		ϕ_1	ϕ	ϕ_2		
1	Bs/G {011}<511>	15.3	45	0	10.02	42.42
2	Bs/S {168}<211>	44.8	35.6	3.2	2.28	25.28
3	{415}<273>	30	41.6	75	4.5	1.41
4	RG {011}<110>	90	45	0	10.7	30.93

Table 2.13. Ni-60 Co 95 % C.W. and annealed at 800°C for 20 hours

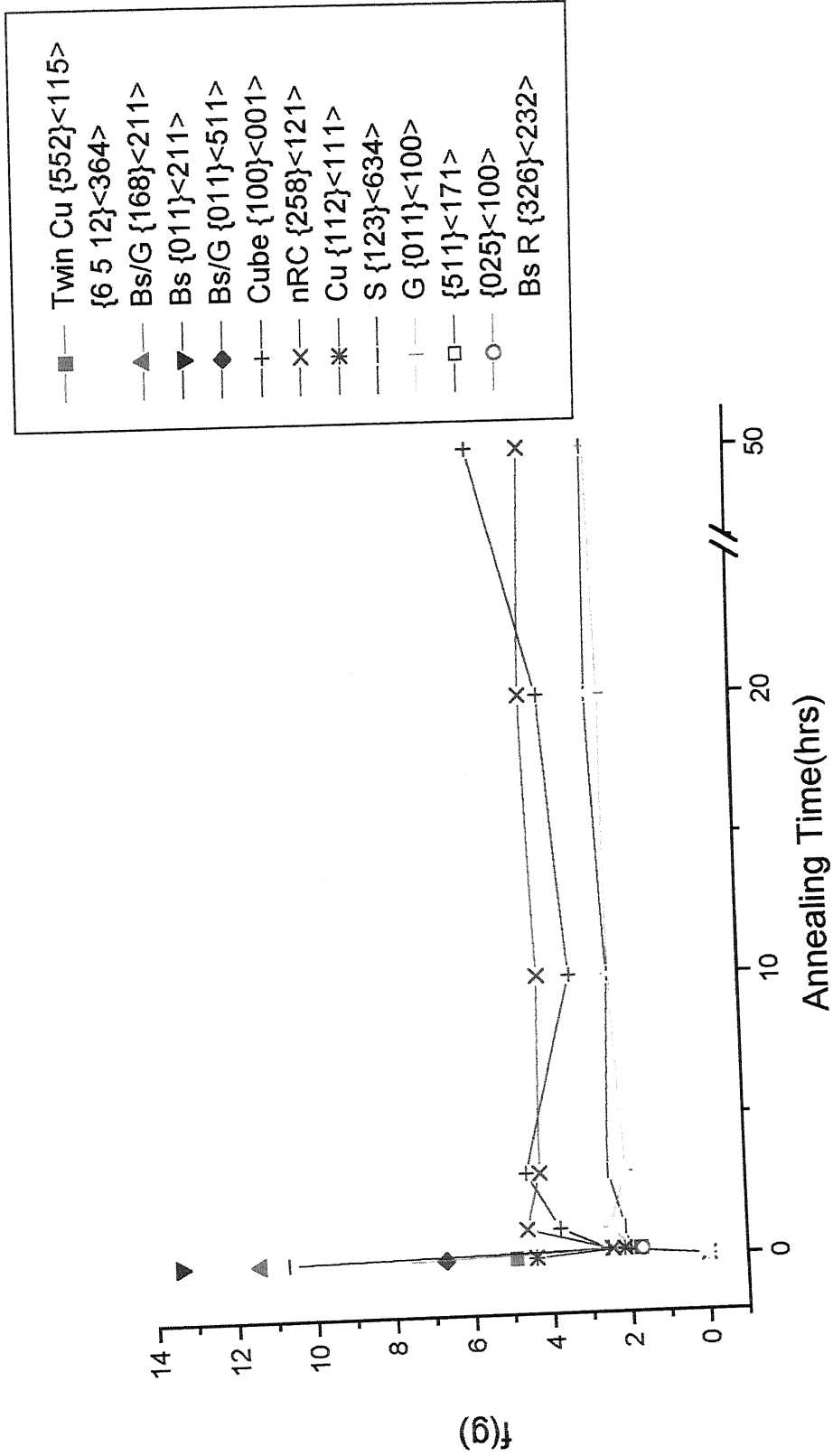
S.No.	Component I.D.	Euler angles			$f(g)$	Vol. % (M_i %)
		ϕ_1	ϕ	ϕ_2		
1	RG {110}<011>	90	40	0	9.25	29.56
2	Bs/G {011}<511>	15.1	45	0	9.63	23.40
3	Bs/S {168}<211>	49.7	39.3	8.7	2.03	7.79
4	{415}<273>	34.2	41.5	75	4.29	24.99
5	G {011}<100>	0	40	0	5.5	6.45
6	BsR {236}<385>	85.3	33.1	30	2.4	7.93

Table 2.14. Ni-60 Co 95 % C.W. and annealed at 800°C for 50 hours

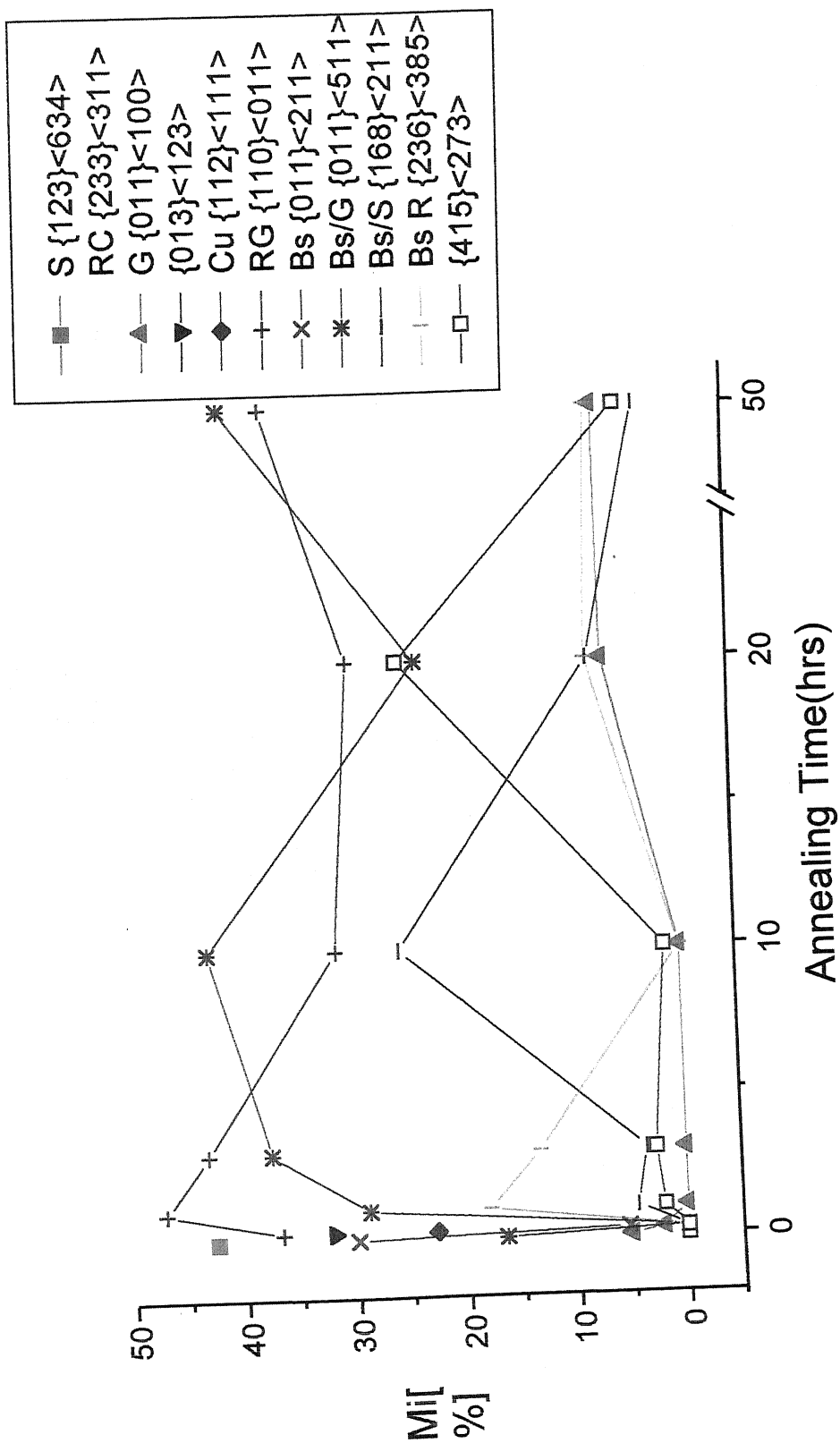
S.No.	Component I.D.	Euler angles			$f(g)$	Vol. % (M_i %)
		ϕ_1	ϕ	ϕ_2		
1	Bs/G {011}<511>	18.3	45	0	11.97	40.63
2	RG {110}<011>	90	45	0	13.15	36.96
3	G {011}<100>	0	45	0	6.5	6.92
4	Bs/S {168}<211>	49	40.2	5	2.2	3.17
5	{415}<273>	30.2	40.7	75	5.2	4.85
6	BsR {236}<385>	84.6	35.2	25	2.8	7.53



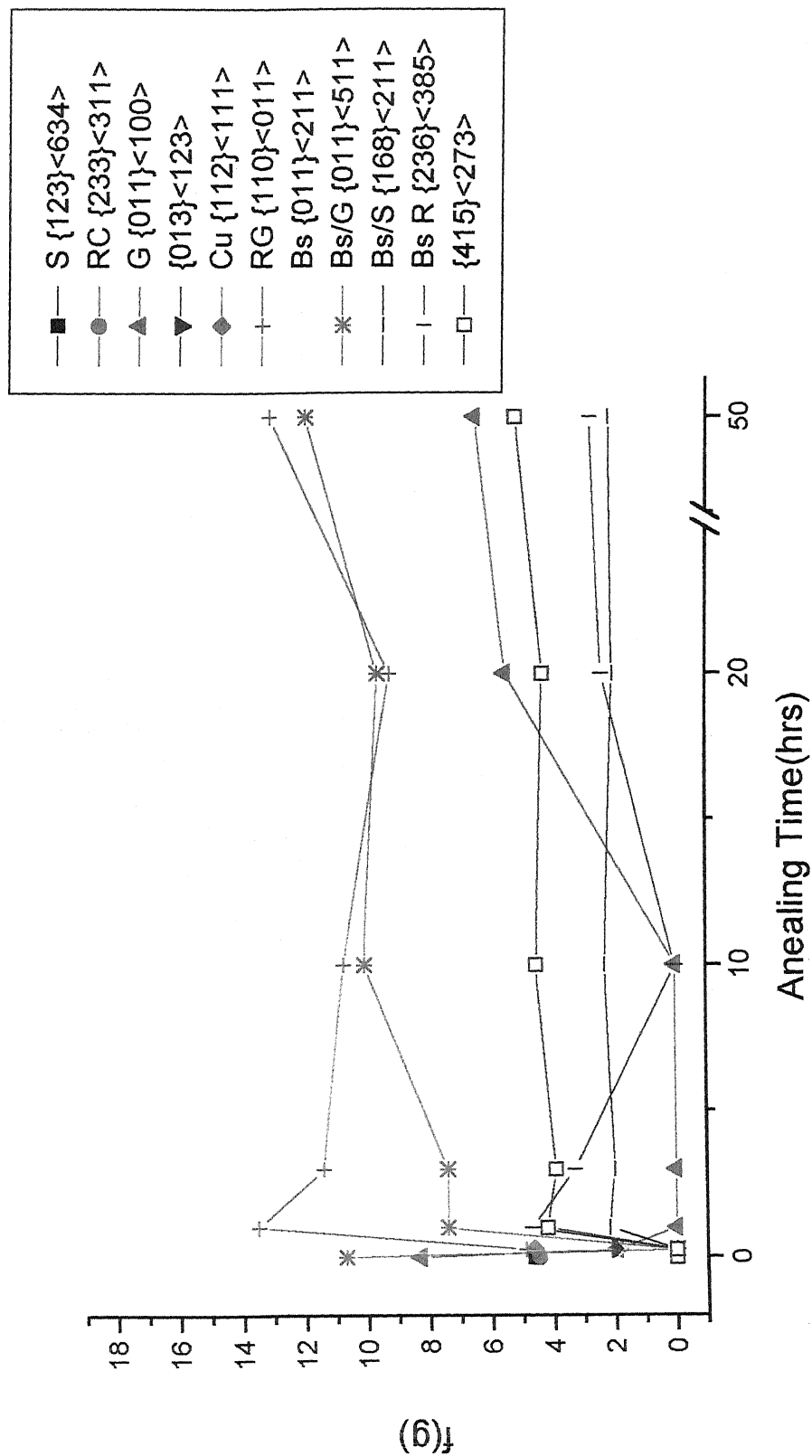
Plot1. Plot showing the variation of M_i [%] with annealing time in Ni-40 Co alloy.



Plot 2. Plot showing the variation of pole density, $f(g)$ with annealing time (hrs) in Ni-40 Co alloy.



Plot 3. Plot showing the variation of Mi[%] with annealing time(hrs) in Ni-60 Co alloy.



Plot 4. Plot showing the variation of pole density, $f(g)$ with annealing time (hrs) in Ni-60 Co alloy.

CHAPTER 5

DISCUSSION

The development of rolling texture in Ni-Co alloys with Co content ranging between 10 to 60 weight percent was earlier reported by Ray[40]. However till date no systematic work on the evolution of annealing textures in this series of alloys has been carried out. The present work was undertaken to elucidate the development of annealing textures in two Ni-Co alloys, namely, Ni-40 Co and Ni-60 Co. The Ni-60 Co alloy is known to develop an alloy type or α -brass type deformation texture, whereas the Ni-40 Co alloy is a transition composition in the Ni-Co series of alloys in the sense that it develops a deformation texture which lies in between pure metal-type and alloy-type. It was thought that there should be interesting differences in the annealing texture of these two alloys.

The microstructure of the 95% cold rolled Ni-40 Co alloy shows mainly deformed cells and some deformation twins. On the other hand nearly complete Debye rings were observed in the electron diffraction patterns of the 95% Ni-60 Co alloy, indicating that the sizes of the crystallites in this deformed alloy are quite small in comparison with those of the Ni-40 Co alloy. This could be due to the finer initial grain size of the Ni-60 Co alloy in the starting annealed material before cold rolling.

The crystallographic textures of the two alloys after 95% deformation have been shown in the form of ODFs in Figures 49 to 56. It is quite clear from these patterns as well as the Tables 2.1 to 2.14 that the deformation texture of the Ni-40 Co alloy is made up of a number of major components such as the Cu, Bs and S. The intensity of Cu component here is rather small, indicating that this particular composition does not possess either the pure metal-type or alloy-type texture, rather it has characteristics common to both the types. The presence of both deformed cells and deformation twins in the TEM microstructures of this alloy clearly indicate that both slip and twinning modes of deformation are possible for this alloy. On the other hand, the ODF of the deformed Ni-60 Co alloy(Figure 53) and the corresponding Table(Table 2.8) clearly show that the

deformation texture of this alloy is predominantly alloy type, with the Bs component as the most intense.

It has been observed that the crystallographic textures of both the Ni-Co alloys vary substantially on annealing from the deformed textures. In the Ni-40 Co alloy, the S and the Bs components are the most predominant ones with a little volume fraction of G and Cu components in the overall deformation texture. Upon annealing it at 800°C for various time durations, nearly Rotated Cube(RC), $\{258\}\langle 121 \rangle$, becomes the major component of the annealing texture. It has been known for a long time that f.c.c. materials with pure metal-type (Cu-type) deformation texture, upon recrystallization, produce an annealing texture with the Cube $\{100\}\langle 001 \rangle$ as a predominant component. The Ni-40 Co alloy, because it contains only a very small volume fraction of the Cu component in the deformation texture, is found to produce only a small cube component after recrystallization annealing. Because of the transitional nature of the deformation texture of Ni-40 Co alloy, the Bs component is also present which is likely to change over to the Bs R component upon annealing. This particular annealing texture component is found in the recrystallization texture of many alloys with large Bs component in the deformation texture. The S component of the deformation texture appears to nucleate grains of the same orientation during annealing and thus adds the S component in the recrystallization texture also.

It has been observed that volume fraction plots of the S and the Bs R components (Plot 1) seem to have a mirror image relationship. It therefore appears that there is a strong interaction between these two components as annealing progresses. Depending on the relative grain boundary mobility, at some instance, one of the components may be enlarging at the expense of the other as annealing continues. Thus the S component appears to dominate till upto 20 hours annealing, beyond which the Bs R predominates. The Goss component intensity, after recrystallization, appears similar to its intensity in the deformed condition, the intensity improves marginally after 50 hours annealing.

Overall, the annealing texture of the Ni-40 Co alloy is very different from the annealing texture of f.c.c. metals and alloys with high or medium stacking fault energy.

That is also very different from that of low SFE f.c.c. materials, such as Ni-60 Co alloy, will be clear from the following photographs.

The Ni-60 Co alloy, which has a predominantly Bs component in its rolling texture produces a totally different texture after recrystallization. Upon annealing at 800°C, the Rotated Goss(RG), $\{110\}\langle 011\rangle$, and Bs/G, $\{011\}\langle 511\rangle$, are found to be the two most predominant components in its texture. As no Cube or Rotated Cube components are found in the annealing texture of Ni-60 Co alloy it can be safely said that this could be due to nonavailability of the Cu component in the rolling texture of Ni-60 Co alloy.

The Bs/G understandably might have arisen from the Bs components of rolling texture of Ni-60 Co alloy. The plot of the volume fraction of the Bs/G component is found to have a mirror image relationship with the $\{415\}\langle 273\rangle$ component, also found in the annealing texture of the Ni-60 Co alloy(Plot 3). This could very well suggest a competitive growth between these two components which ultimately results in the Bs/G component outweighing over the $\{415\}\langle 273\rangle$ beyond 20 hours of annealing.

The S component which is very much predominant in the rolling texture of Ni-60 Co alloy could also provide the nuclei upon recrystallization to produce the Bs/S component. The plot showing the volume fraction of the Bs/S component again seem to have a mirror image relationship with the rotated Goss(RG) which means that these two components could be competing with each other, ultimately resulting in the RG component outweighing the Bs/S beyond 20 hours of annealing(plot 3).

The Goss(G) component which was present to the extent of ~5% by volume in the cold rolled sample remains more or less constant after annealing over a long period of time.

The nonavailability of the Bs component in the annealing texture of Ni-60 Co alloy suggests its conversion to components such as Bs R, Bs/G and Bs/S components which were found to be important components of the annealing texture. Thus the annealing texture development in the Ni-60 Co alloy appears to be quite a dynamic process in which the individual components compete with one another to become the predominant texture component. The volume fraction of a particular component after a particular annealing time depends on how its natural growth is affected by grains of other

orientations and also on the relative mobility of the grain boundaries surrounding the grains of such orientations.

CONCLUSIONS

1. Ni-60 Co alloy shows alloy-type rolling texture while Ni-40 Co alloy shows the transition between pure metal-type and alloy-type rolling texture.
2. After annealing, the recrystallization texture of Ni-40 Co and Ni-60 Co alloys change completely from their deformation textures.
3. After recrystallization, nearly Rotated Cube becomes the predominant component of the annealing texture of Ni-40 Co alloy. On the other hand, Bs/G and RG are the dominant components in the annealing texture of the Ni-60 Co alloy.
4. The nonavailability of the Cu component in the deformation texture of the Ni-60 Co alloy is considered to be responsible for the total suppression of the Cube texture in that alloy on annealing. On the other hand, presence of a small volume fraction of the Cu component in the deformation texture of the Ni-40 Co alloy could be the reason why some amount of the cube component forms in the annealing texture of this alloy.
5. The annealing texture development in both the alloys appears to proceed by a competitive growth process during the entire period of annealing.

REFERENCES

1. J.E.Bailey, Phil.Mag; 5, 8.33 (1960).
2. J.E.Bailey and P.B.Hirsch, Proc.Roy.Soc., 11, A267 (1962).
3. P.Gordon, Trans.A.I.M.E., 203, 1043 (1955).
4. H.M.Clarebrough, M.E.Hargreaves and G.W.West, Proc.Roy.Soc. (London), A232 252 (1955).
5. F.Haessner, 'Recrystallization of Metallic Materials', Ed.F.Haessner, p.5, Dr. Reidorer-verlag, GMBH, Stuttgart (1971).
6. P. Polukin, S. Gorelik and V. Vorontsov, 'Physical Principles of Plastic deformation', Mir Publishers, Moscow, p. 251 (1983).
7. J.G.Byrne, 'Recovery, Recrystallization and Grain Growth', p.37 (1965), The Macmillan Co., New York.
8. H.Hu, Trans. A.I.M.E., 224, 75 (1962).
9. A.S.Keh, 'Direct Observation of Imperfections in Crystals', New York (InterScience), (1962).
10. J.C.M.Li, Recrystallization, Grain Growth and Textures', p.45 (1966), A.S.M., Metals Park, Ohio.
11. P.B.Price, Phil.Mag., 5, 873 (1960).
12. C.N.J.Wagner, Acta Met., 5, 427 (1957).
13. R.W.Cahn, J.Inst.Met., 76, 121 (1949).
14. R.W.Cahn, 'Progress in Metal Physics', 2, 151 (1950).
15. C.G.Dunn and F.W.Daniels, Trans. A.I.M.E., 191, 147 (1951).
16. J.J.Gilman, Acta Met., 3, 277, (1955).
17. J.C.M.Li, Acta Met., 8, 563 (1960).
18. N.a.Bryshko, V.V.Gubernatorov, B.K.Sokolov, I.V.Gervaseva and V.N.Gundyrev, Dokl.Akad.Nauk.SSR, 255 (6), 1367-1369.
19. H.Hu and A.Szirmae, Trans. A.I.M.E., 221, 839 (1961).
20. J.C.M.Li, J.Appl..Phys., 33, 2958 (1962).

21. W.T.Read, 'Dislocations in crystals', (1953), New York (McGraw-Hill).
22. R.W.Cahl, 'Recrystallization of Metallic Materials', ed.F.Haessner, p.43 (1971), Dr. Riedorer-Verlag, GMBH, Stuttgart.
23. P.A.Beck and P.R.Sperry, J.Appl.Phys., 21, 150 (1950).
24. R.D.Doherty, 'Metal Odlew', 5(2), 179-196 (1979).
25. B.B.Rath and H.Hu, Trans. A.I.M.E., 236, 1193 (1966).
26. S.Kohara, M.N.Parthasarathi and P.A.Beck, Trans. A.I.M.E., 212, 875 (1958).
27. K.T.Aust and J.W. Rutter, Trans. A.I.M.E., 215, 119 (1959).
28. K.T.Aust and J.W. Rutter, Trans. A.I.M.E., 215, 820 (1959).
29. J.W. Rutter and K.T.Aust, Trans. A.I.M.E., 218, 682 (1960).
30. C.Frois and O. Dimitrov, Compt.Rend., 252, 1465 (1961).
31. K.T.Aust, G.Ferran and O.G.Cizeron, Compt.Rend., 257, 3595 (1963).
32. J.W.Cahn, Acta Met., 10, 789 (1962).
33. R.K.Ray, Ph.D. Thesis, March, 1973, Univ. of Birmingham.
34. V.Yu.Novikov, Poverkhn. Fiz., Khim. Mekh. 1982, 5, 47-49.
35. G.Abbuzzese, K.Lucke and H.Eichelkraut, Grain Growth in the presence of Textures.
36. R.K.Ray, W.B.Hutchinson, F.M.C.Besag and R.E.Smallman, J.Microscopy, 97, 217 (1973).
37. H.J.Bunge, Mathematische Methoden der Texturanalyse. Academic Press, Berlin (1969).
38. Hsun.Hu, r.S.Cline and S.R.Goodman, Recrystallization, Grain Growth and Textures, A.S.M., 295 (1965).
39. I.L.Billmore and S.F.H.Fletcher, Recrystallization, Grain growth and Textures, A.S.M., 448 (1965).
40. R.K.Ray, Acta Metall. Mater. Vol. 43, No. 10, 3861-3872, 1995.
41. H.O.Asbeck, Doctoral thesis, R.W.T.H., Aachen (1973).
42. P.J.Goodhew, 'Specimen Presentation in Materials Science', p.71 (1973).
43. R.J.Roe, J.appl.Phys. 36, 2024 (1965).

44. J.Jura and J.Pospiech, Textures 3, 1 (1978).
45. W.Truszkowski, J.Pospiech, J.Jura and B.Major, Proc.3^e me Coll.Europ^e en Sur Text. Pont-^a-Mousson, France (1973).
46. K.H.Virnich, J.pospiech, A.Flemmer and K.L^ücke, Proc. Fifth Int. Conf. Text. 1, 129 (1978).
47. J.Hirsch and K.L^ücke, Acta metall.33, 1927 (1985).
48. J.Hirsch and K.L^ücke, in Theoretical Methods of Texture Analysis (edited by H.J.Bunge), p.53. D.G.M., Oberursel (1987).
49. J.Hirsch and K.L^ücke, Acta metall. 36, 2863 (1988).
50. K.L^ücke, J.Pospiech, K.H.Virnich and J.Jura, Acta metall. 229, 167 (1981).